Synthesis of carbon nano-onions and their application in photovoltaic cells

By

Thomas Hlamalani Mongwe

Student Number: 1585603

BSc (Hons)

A dissertation submitted to the Faculty of Science, University of the Witwatersrand, Johannesburg, in fulfillment for the degree of Master of Science in Chemistry.

Promoters: Dr. Manoko S. Maubane and Prof. Neil J. Coville

University of the Witwatersrand, Johannesburg. April 2018

DECLARATION

I declare that this dissertation, which is hereby submitted for a degree of Master of Science in the Faculty of Science, School of Chemistry, University of the Witwatersrand, Johannesburg is my own unaided work and has not been submitted for examination at any institution.

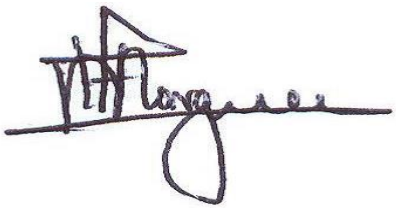

Thomas Hlamalani Mongwe

On this 12th day of April 2018

DEDICATION

This work is a special dedication to my family:

My father Mr Y.S Mongwe, My mother Ms J.S Skhosana

and

My younger brother Mr E.N Mongwe

ACKNOWLEDGEMENTS

First of all, I would to express my deepest gratitude to the all mighty God, for all that he has provided to me. After all, I would like to express my sincere gratitude to my supervisors Dr Manoko S. Maubane and Professor Neil J. Coville for their wonderful insights and for giving me a chance to learn under their mentorship. To both Dr Manoko S. Maubane and Dr Mahlaba A. Debeila, I would like to extend my appreciation for all your efforts you have put to educate and motivate me.

A warm thank you goes to Dr Boitumelo J. Matsoso, Dr Bridget K. Mutuma and Dr Mildred A. Airo for the kindness and mentorship they provided to me, as well as their great inputs through their motivational guidance they offered through my journey. Special acknowledgement also goes to the School of Chemistry and CATOMMAT members at the University of the Witwatersrand for being such great colleagues and friendly fellows throughout my study period.

I am grateful to the microscopy and microanalysis unit (MMU) and the powder X-ray diffraction spectroscopy unit (PXRDU) headed by Prof. Alexander Ziegler and Prof. Dave Billing respectively for allowing me to make use of the valuable facilities and or instrument(s) in their respective units. It is of great pleasure to also acknowledge Dr. Rudolph Erasmus for his kind assistance during Raman spectroscopy analysis and Dr James W. Smith for granting me a chance to do high resolution transmission electron microscopy (HRTEM) analysis through the *Council for Scientific and Industrial Research* (CSIR) characterization facility.

I would like to thank the National Research Foundation (NRF) for the funding assistance they provided as my stepping stone and to the DST-NRF Centre of Excellence in Strong Materials (COE-SM) for a bursary for their further financial assistance to complete this research project.

Special thanks are due to Mr Sunnyboy S. Sibanyoni and his family for their support throughout my difficulties, and lastly to all my family members and friends who kept on encouraging me to keep-up my head and never give up.

Proverbs 18:15: “The mind of the prudent acquires knowledge, and the ear of the wise seeks knowledge”.

PRESENTATIONS AND AWARDS

PRESENTATIONS

- MSSA 2016 conference: Poster presentation "*Synthesis of carbon nano-onions and their application to dye-sensitized solar cells*", Port Elizabeth (December 2016)
- CoE-SM/AMSEN annual student presentation: Poster presentation "*Synthesis of carbon nano-onions and their application in photovoltaic cells*", Johannesburg (June 2017)
- FEMMS 2017 conference: Poster presentation "*Synthesis of water soluble carbon nano-onions*" Johannesburg (September 2017)
- NYRS-SANI 2017 symposium: Pitch and poster presentation "*Facile synthesis of carbon nano-onions*", Pretoria (October 2017)
- Wits Cross Faculty 2017 Symposium: Poster presentation "*Synthesis of carbon nano-onions for catalytic purposes in dye-sensitized photovoltaic cells*", Johannesburg (October 2017)
- CATSA 2017 conference: Poster presentation "*Synthesis of carbon nano-onions for catalytic purposes in dye-sensitized photovoltaic cells"*, Pilanesburg (November 2017)
- MSSA 2017 conference: Poster presentation "*Simple synthesis of water soluble carbon nano-onions"*, Belabela (December 2017)

AWARD(S)

- Received a poster presentation certificate: CoE-SM/AMSEN annual student presentation, Johannesburg (June 2017)
- Won second prize for pitch and poster presentation, and received a poster presentation certificate :NYRS-SANI 2017 symposium, Pretoria (October 2017)
- Received a poster presentation certificate: Wits Cross Faculty 2017 Symposium, Johannesburg (October 2017)

ABSTRACT

In this study the synthesis and use of multi-layered and quasi-spherical carbon nano-onions (CNOs) for use as a catalyst in dye-sensitized solar cells (DSSCs) is reported. The synthesis of CNOs was achieved following procedures reported in the literature. Two synthesis methods are reported this study; the catalytic chemical vapour deposition (CCVD) and the flame pyrolysis method (FP).

To selectively synthesize CNOs using CCVD, a supported iron catalyst was prepared for the decomposition of acetylene (C_2H_2), used as carbon source. Sodium chloride was used as a support due to its water solubility advantage. During the CCVD synthesis at 450 °C, mixtures of carbonaceous nanomaterials were observed that included carbon nanofibres. To counter act this problem, the FP method was used and CNOs of high purity were obtained from this method. The FP method is a catalyst free method and in this study clarified butter (Ghee) was used as the carbon source as well as the fuel. The flame produced the soot material (CNOs) effectively. The carbon nanostructured materials produced from both methods were analyzed and characterized using various analytical techniques such as Branauer-Emmett-Teller (BET) analysis, Fourier Transform Infrared (FTIR) spectroscopy, Raman spectroscopy, Scanning electron microscopy (SEM), Transmission electron microscopy (TEM), Thermo-Gravimetric Analysis (TGA), Ultra-Violet visible (UV-vis) spectroscopy, and Powder X-ray diffraction (XRD). These techniques revealed that both methods produce CNOs. However, the ones produced from the CCVD method incorporated the metal catalyst and also included carbon nanofibers (CNFs). The CNOs produced were quasi-spherical nanostructured materials with diameters less than 100 nm. Materials produced through FP, were very pure and were synthesized in good yield in gram scaled.

The highly pure CNOs from the FP method were successfully doped with nitrogen (post-doped) using gaseous ammonia. Both the doped and undoped CNOs were tested in DSSCs. It was observed that both types of materials are capable of acting as a catalyst for this type of photovoltaic cells. However, the nitrogen doped material had better catalytic behavior compared to the undoped CNOs. This was attributed to the fact that doping CNOs with nitrogen promoted n-type behavior such that electron transportation in the cell was easily promoted.

TABLE OF CONTENTS

LIST OF FIGURES

Chapter 2

Chapter 3

Chapter 4

Chapter 5

Chapter 6

Appendix A

LIST OF SCHEMES

Chapter 2

Chapter 4

Chapter 5

Chapter 6

LIST OF TABLES

Chapter 4

Chapter 5

Chapter 6

LIST OF ABBREVIATIONS AND NOMENCLATURE

Abbreviation	Description
ASSC	Amorphous silicon solar cell
BET	Branauer-Emmett-Teller
CCVD	Catalytic chemical vapor deposition
CE	Counter electrode
CNFs	Carbon nanofibers
CNMs	Carbon nanostructured materials
CNOs	Caron nano-onions
CNTs	Carbon nanotubes
CVD	Chemical vapor deposition
CH_3COOH	Acetic acid
CH_3COCH_3	Acetone
$CH_3COCH_2COCH_3$	Acetyl acetone
CH_3CH_2OH	Ethanol
$C_{10}H_{19}IN_2$	1-hexyl-3-methylimidazolium iodide
$CH_3OCH_2CH_2CN$	3-methoxypropionitrile
$C_9H_{13}N$	4-tert butylpyridine
d-H_2O	Deionized water
DSSC	Dye-sensitized solar cell
Fe	Iron
FF	Fill factor
FP	Flame pyrolysis
FT	Fischer-Tropsch
FTIR	Fourier Transform Infrared spectroscopy
FTO	Fluorine doped tin oxide
GC	Gräetzel cell
GFP	Ghee flame pyrolysis
HOMO	Highest occupied molecular orbital.
HRTEM	High resolution transmission electron microscopy

I^-/I_3^-	Iodine redox electrolyte
I_2	Iodine
ITO	Indium doped tin oxide
J_{mp}	Maximum point photocurrent
J_{ph}	Light generated current density
J_{sc}	Short-circuit current density
J–V	Photocurrent density-voltage
LiI	Lithium iodide
LUMO	Lowest unoccupied molecular orbital
NCNOs	Nitrogen-doped carbon nano-onions
OSC	Organic solar cell
P_{light}	Incident light power
PCE;η	Power conversion efficiency
PtCE	Platinum coated counter electrode
Pt	Platinum
PV	Photovoltaic
R_{sh}	Shunt resistance
R_s	Series connection resistance
SEM	Scanning electron microscopy
STC	Standard test condition
TCO	Transparent conducting oxide
TEM	Transmission electron microscopy
TGA	Thermo-Gravimetric Analysis
TiO_2	Titanium dioxide
UV-vis	Ultra-Violet visible
V_{mp}	Maximum point voltage
V_{oc}	Open circuit voltage
wt%	Weight percentage
XRD	Powder X-ray diffraction

Chapter 1: Introduction to the study

1.1. Introduction

This is the first chapter of the dissertation which introduces the aims and objectives together with the background and motivation toward the study.

1.1.1. Study background and motivation

Studies have been done on alternative renewable energy technologies with an aim of optimizing resources for our modern society. Solar energy is one of the possible solutions to the energy challenges [1]. Possible solutions to the electrical energy crisis could be provided by use of independent power (energy) producers (IPPs) which use wind, solar and hydro as renewable resources. The correlation between an increased energy demand and the development of nanomaterials has created many studies in the field of nanoscience.

Grätzel and O'Regan reported on energy transformation using a dye sensitized solar cells (DSSCs). The energy transformation was the conversion of radiant energy to electrical energy by DSSCs devices. The cells were found to be of relatively low cost, but efficient, exhibiting commercially realistic energy-conversion efficiency [2]. The devices have both transparency and flexibility [3]. The DSSCs have advantages compared to the amorphous silicon solar cells such as their low fabrication costs. However, the use of flat electrodes and liquid electrolyte for dye sensitization of semiconductors face intrinsic problems for photo-electrochemical studies and these problems need to be addressed [4]. The problems can be addressed by making use of the novel carbon materials.

Studies to use different carbon based materials have been undertaken over the past decades. For example, Iijima discovered the shaped carbon nanomaterials usually called carbon nano-onions (CNOs) or onion-like carbon (OLC). They have a polyhedral nanostructure with particles sizes that are less than 100 nm and were observed as a byproduct in carbon black synthesis [5]. The carbon nano-onions are in a family of carbon nano-materials (carbon nano-fibers, horns, spheres, tubes etc.). Different synthetic methods have been reported for the synthesis of CNOs and include the chemical vapour deposition method (CVD) [6]. These materials have potential

applications which include their use in fuel cells and solar cells [7]. These carbon nano-materials can be functionalized to obtain long term operation stability when used as counter electrodes compared to the commercially available platinum-based electrodes used in photoelectrochemical cells [8]. The use of these materials for solar cells can provide a possible solution to problems faced in the fabrication of DSSCs.

This study focuses on the synthesis of CNOs for use in solar cells. The CNOs can provide a link between carbon nano-materials and energy converting devices (solar cells). These carbon materials exhibit good electrical properties and long term stability.

1.2. Purpose of the study

1.2.1. Aim of the study

The proposition for this study was the functionalization of CNOs will give a CNOs counter electrode with improved efficiency when compared to pristine CNOs in solar cells. However, solar cells containing CNOs as a counter electrode will not be highly effective when contrasted to DSSCs fabricated using platinum catalyst. DSSCs fabricated using CNOs will only prove that the counter electrode made from carbon nanostructured materials conceptually work but do not exhibit higher efficiency than DSSCs with PCE. This hypothesis leads to the aim of the study as follows:-

- To synthesize CNOs with quasi-spherical structural morphologies less than 100 nm.
- To characterize the functionalized CNOs for application in DSSCs as catalytic nanomaterials.

1.2.2. Objectives

- To use the catalytic chemical vapour deposition (CCVD) method and flame pyrolysis (FP) method to synthesize the CNOs.
- To functionalize CNOs through doping with nitrogen to increase the material's catalytic activity.

- To analyse the CNOs using various analytical techniques such as: BET, FTIR, Raman spectroscopy, SEM, TEM, TGA, UV-Vis spectroscopy and XRD to analyse and characterize the synthesized CNOs.
- To study both the physical and chemical properties of functionalized and pristine CNOs.
- To fabricate dye-sensitized solar cells (DSSCs) using a counter electrode (CE) coated with CNOs (both functionalized and pristine materials).
- To compare the performance of CNOs based DSSCs results with Pt based DSSC.

1.3. Outline of dissertation

Chapter 1: Gives a brief motivation, the research aims, hypothesis, and objectives of this study.

Chapter 2: A detailed review of the literature base on carbon nano-onions and dye-sensitized solar cells is presented in this chapter.

Chapter 3: Gives detailed descriptions and/ or explanations of the characterization techniques that were used in this study.

Chapter 4: The results obtained from the CCVD synthesis of CNOs, together with their discussion and interpretation are presented in this chapter.

Chapter 5: Describes the synthesis, results and discussion on work done on the GFP synthesis and N-doping of CNOs.

Chapter 6: Presents the DSCs fabrication method, results obtained from the device tests along with discussions based on results.

Chapter 7: Gives the general conclusions and future recommendations based on the results obtained with respect to the aims and objectives of the study.

References

1. Qiu X, Burda C. *Chemical Physics*,339 (2007); p 1
2. O'Regan B, Grätzel M. *Nature* 353 (1991); p 737
3. Grätzel M. *Journal of Photochemistry and Photobiology C: Photochemistry Reviews* 4 (2003); p 145
4. Wei D. *Int. J. Mol. Sci. 11* (2010); p 1103
5. McDonough JK, Gogotsi Y. *Electrochem. Soc. Interface Fall.* 22 (2013); p 61
6. Bartolome JP. *Tesis Doctoral en Xarxa.* 1 (2015); p 7
7. Kuznetsov O. *UMT Dissertation Publishing.* 1 (2010); p 7
8. Yu D, Nagelli E, Du F, et al. *J. Phys. Chem. Lett.* 1 (2010); p 2170

Chapter 2: Literature review

2.1. Catalytic and non-catalytic growth of carbon nano-onion

This is the second chapter of the dissertation that presents the detailed literature review based on carbon nano-onions (CNOs). In this chapter, the catalytic and non-catalytic methods used to synthesize CNOs are discussed.

2.1.1. Background on the synthesis of carbon nanostructured materials using transition metals

Transition metals can be defined as elements whose atoms have a partially filled *d* sub-shell [1]. It is archaeologically evident that different transition metals have been used for more than 40 decades. These elements are found in the d-block of the periodic table and include the most common elements used to prepare catalysts for the preparations of various carbon nanostructured materials (CNMs) which include CNOs as illustrated in **Scheme 2.1**. Elements such as cobalt, copper, iron and zinc have been used as catalysts to prepare CNOs.

In this study, we focus on iron (Fe) a group 8 with the electron configuration, [Ar] $3d^6$ $4s^2$ as a catalyst to make CNOs. Fe has a wide range of oxidation states, -2 to +6, with +2 and +3 being the most common [2]. It occurs in various forms ranging from chamosites to vivianites allowing its various applications in different industries and research fields. In various research fields the oxides of iron have also received special attention due to their many applications and versatility in catalysis [2]. Its oxides occur in many forms, with the common ones being: magnetite (Fe_3O_4), maghemite (γ-Fe_2O_3), and hematite (α- Fe_2O_3) [3, 4].

Different CNMs can be synthesized using a catalytic chemical vapour deposition method (CCVD) in which various shapes and sizes of carbon can be obtained [5]. However, ions and oxide nanoparticles of Fe can have a significant influence on the structural morphology of the CNMs formed [6]. Generally, a catalyst is prepared on a support and the role of the support is to disperse nanoparticles (e.g. of iron) homogeneously, leading to better yields of desired CNMs.

2.2. Application of transition metals as catalyst precursors for synthesizing carbon nano-onions

2.2.1. Capabilities of iron to act as a catalyst for carbon deposition in the CCVD

Among the metals used to make carbon materials such as cobalt and nickel, iron is traditionally used to control the type of carbon material grown in the CCVD. Typically, the elemental Fe and its alloys are ferromagnetic materials. The Fe nanoparticles can be used as catalytic particles when growing CNMs. It was suggested that the vapour liquid-solid mechanism (VLS) is followed during carbon deposition onto the Fe nanoparticles (see **Scheme 1**). This mechanism involves dissolution of a carbon source into the bulk of the particles [7, 8]. Moreover, the mechanism allows studies on the viability of a metal catalyst to deposit carbon atoms [9, 10].

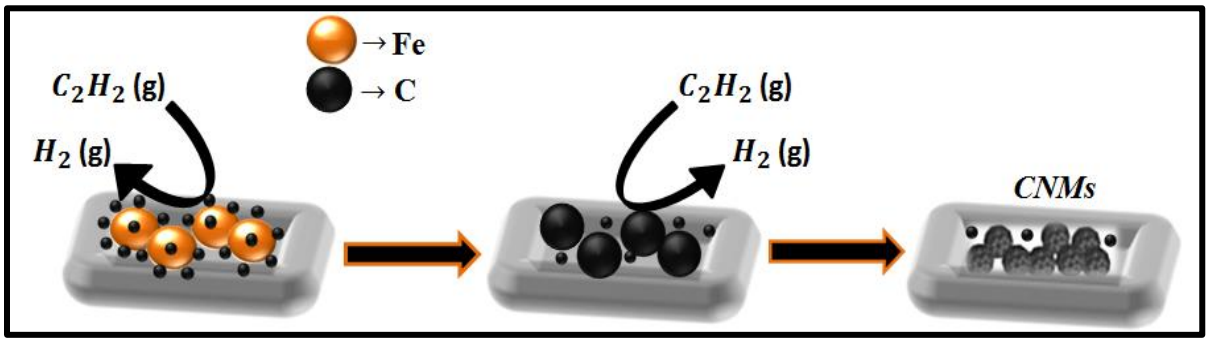

Scheme 2.1: Diagram shows the suggested VLS mechanism for carbon growth on iron nanoparticles [11].

The vapour liquid-solid mechanism allows iron nanoparticles to decompose hydrocarbons during CNMs formation. Decomposition of hydrocarbons happens under thermal conditions (high temperatures) in which the cracked fractions are dissociated into carbon atoms. The carbon atoms are later deposited and adsorbed onto the catalyst surface and then react to form bonds (carbon-carbon bonds) hence producing graphitic layers of CNMs as proposed in the reaction below (as shown in **Eq. 2.1**) [12].

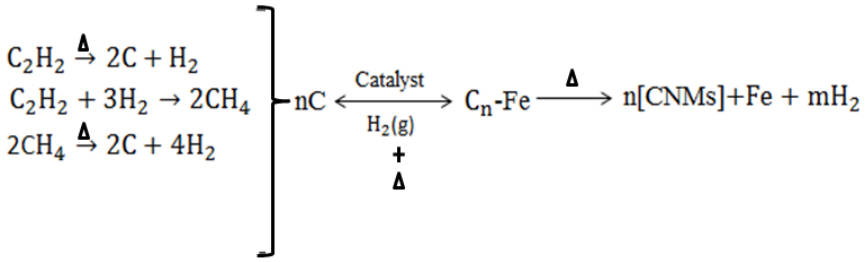

……..... 2.1

The catalyst can be prepared using different preparation techniques such as co-precipitation; sol-gel and impregnation to investigate its activity and selectivity behaviour [13]. The iron nanoparticles can sinter depending on temperature used when the sol-gel method is chosen for catalyst preparation [14].

Generally, nano-sized transition metal particles have been successfully used in CCVD including nickel, cobalt, molybdenum and copper either in oxide or metallic forms or as mixtures [15, 16]; Compounds such as Fe_2Co and Fe_2Ni were found to be efficient catalysts in the CCVD. The catalyst particles can also agglomerate depending on the drying process used during its preparation. The catalyst drying process significantly influences the catalyst particle size as well as the agglomeration of the catalyst particles. Agglomeration along with other negative factors can be avoided through a freeze drying process [17].

2.2.2. Synthesis of carbon nano-onions using an iron catalyst

Different carbon nanomaterials, from fibres to tubes include spherical carbon nanomaterials (spheres, dots etc.) have been prepared using various synthetic methods. Among the group of spherical CNMs, carbon nano-onions (CNOs) which are quasi-spherical nanomaterials have recently attracted researchers' attention because of their unique properties. However, to date, little attention has been paid to this type of nanomaterial. The preparation methods to make this multi-layered nanomaterials can be classified into two broad categories; chemical and physical methods [18]. Chemical methods include the catalytic pyrolysis reactions of hydrocarbons, catalytic disproportionation of carbon source as well as explosions. In contrast to chemical methods, physical methods used to synthesize CNOs include methods such as electric arc discharge and laser ablation methods [18]. Compared with other methods, CCVD has been considered as facile and inexpensive. This method can be easily implemented, and has been

widely used because of its ability to yield CNOs of high purity in gram scale [19, 20]. Different carbon sources and catalysts can be used in CCVD for CNOs synthesis.

Iron catalysts can be used to synthesize CNOs in an inert gas (e.g. nitrogen environment) to enhance the growth process. A supported catalyst is commonly prepared by incipient wetness impregnation method and used in CCVD processes when synthesizing CNOs [20]. It is well known that the growth of carbon nano-tubes by CCVD using a transition metal catalyst is greatly enhanced in a nitrogen environment [21]. Generally, CNMs can be synthesized using supported catalysts (e.g. iron catalyst) which display an enhanced dispersion of the active phase withstanding the mechanical degradation that threatens bulk of the catalyst [22, 23]. A catalytic decomposition of acetylene to produce CNOs can also be carried out through CCVD in the presence of an iron catalyst supported on sodium chloride [24, 25].

2.2.3. The use of sodium chloride as iron catalyst support

The preparation of the metal catalyst often requires the use of a supported or unsupported metal catalyst [26]. The catalyst formation can involve techniques such as incipient wetness impregnation for supported catalysts, while unsupported catalysts can be prepared by reduction among other techniques. Supports such as alumina (Al_2O_3), magnesium oxide (MgO), sodium chloride (NaCl), calcium carbonate ($CaCO_{3)}$, and zeolite have been used to synthesize carbon nanostructured materials (CNMs). However, the separation of these supports from the final products is a challenge. Thus water soluble supports have been used since they allow easy removal of the support from the product. In CCVD, CNOs have been synthesized using an iron catalyst supported on sodium chloride (NaCl). This support can be readily separated from the product since it dissolves in water [27]. The amount of iron supported on a given amount of NaCl is an important factor in the CNOs reaction since agglomerations of metal nanoparticles needs to be avoided.

2.3. Catalyst free synthesis of carbon nano-onions

Recent studies have reported on new developments in terms of CNOs synthesis methods. Among these, facile flame pyrolysis of various types of oils have been reported to produce CNOs with

particle sizes <100 nm [28, 29]. Apart from being simple, a flame pyrolysis method has advantages such as: (1) it is a catalyst free method, (2) it does not require a large amount of energy, (3) it is inexpensive (cost effective) and (4) it can yield large amounts (gram scale) of CNOs [30]. Moreover, reports also reveal that sources such as camphor and polystyrene foam plastic wastes, carrots, tomatoes, and tree leaves can also be used to synthesize CNOs [31-33].

2.4. Hetero atom doping of carbon nano-onions

In most studies, different carbon nano forms have been doped with different heteroatoms including nitrogen (N). The nitrogen doped carbon nanostructured materials (NCNMs) have been used in various applications. This is possible since nitrogen atoms are capable of adding electrons to the CNMs and they provide electron carriers for the conduction band. NCNMs also to exhibit various advantages such as narrower band gap energies created when nitrogen atoms are introduced into CNMs structural matrix. Possibilities for good catalytic and electrical conductivity properties usually emerge as a result of effective structural modulation due to the extra π-electrons in the graphitic plane of the NCNMs. Moreover, when considering the electronegativity difference between nitrogen and carbon (~0.5) [34], this gives rise to different structural properties including a high surface energy and also increases n-type carrier concentration of graphitic carbons. These properties also benefit catalysts, energy conversion/storage devices, and other flexible electronics [35].

Direct doping is possible during CNMs synthesis and the process is known as “in situ” doping. Moreover, post-treatment of pre-synthesized CNMs with a heteroatom containing precursor can also be achieved by “ex-situ” or post doping [36]. The extrinsic and intrinsic doping are processes called “in situ” and “ex-situ” doping respectively. The heteroatom dopant is introduced into the undoped carbon matrix for extrinsic modification whereas for intrinsic doping process, both the heteroatom precursor and carbon composition materials are used simultaneously [36, 37].

The most commonly used dopants include boron (B), nitrogen (N), sulphur (S), fluorine (F) and phosphorus (P). However, doping CNMs with nitrogen can be a facile process and precursors used for nitrogen doping include acetonitrile and ammonia. These precursors can be used for “in situ” and “ex-situ” doping respectively.

NCNMs have been explored as supports for noble metal such as palladium (Pd), platinum (Pt), and others. Metals such as Pd and Pt are used as catalysts in chemical synthesis as well as in energy conversion applications because of their excellent electronic properties. In catalysis, NCNMs are commonly used to stabilize and enhance the utilization of catalysts. Moreover, it is well documented that the strong metal-support interaction between some metal atoms (e.g. Pt) and NCNMs significantly improved the metal nanoparticles dispersion, thereby enhancing the metal utilization, stability and catalytic activity [38]. It can be proposed that doping CNOs with N atoms will introduce effective structural modulation in the CNOs structure.

2.5. Growth mechanism of carbon nano-onions

Among the carbon allotropes, CNOs are nanomaterials composed of spherical concentric fullerene-like shells forming multi-layered structures as shown in **Fig. 2.1a and b**. These nanostructured materials are graphitic with particle sizes having diameters less than 100 nm (see **Fig. 2.1a**). Depending on the synthesis method used, CNOs can be classified into two types, which include: (1) hollow CNOs and (2) core–shell structured CNOs (see **Fig. 2.2b**). Hollow CNOs are spherical or polyhedral in shape. The innermost layer of the spherical hollow CNO can be a C_{60} cage while the polyhedral CNOs usually have a larger volume than the C_{60} cage.

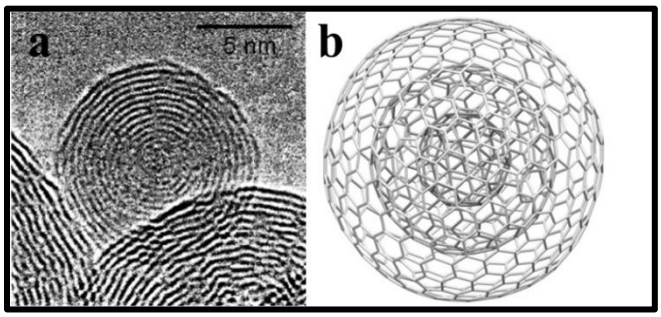

Figure 2.1: Shows; (a) HREM Micrograph of a quasi-spherical graphitic (size: < 100 nm) [39], (b) schematic diagram of multi-layered CNOs [40].

These carbon nano forms are sometimes called onion-like carbon or onion-like fullerenes. These carbon nanomaterials exhibit outstanding chemical and physical properties [41]. Depending on the method of synthesis their diameters might vary. Their growth mechanism requires any type of carbon source (e.g. acetylene gas C_2H_2, ghee oil and chitosan etc.). The synthesis procedures

are generally simple and cost effective. The procedures can either follow a bottom-up or top-down approach as shown in **Scheme 2.2**.

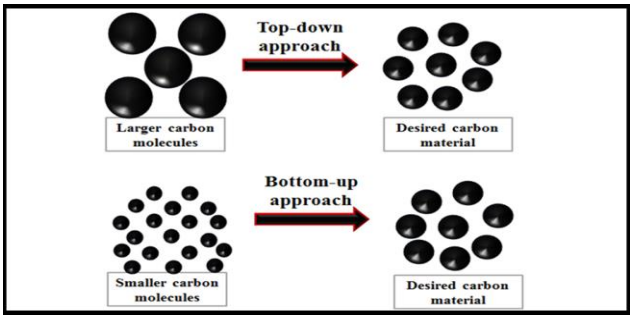

Scheme 2.2: Illustrates the bottom-up and top-down procedures for synthesis of CNOs [42].

Scheme 2.2 shows a possible reaction mechanism for the synthesis of CNOs through a CCVD method. The scheme illustrates the bottom-up method when C_2H_2 is decomposed in the presence of a metal catalyst. The formation of CNOs consists of different steps which include: (1) cracking, (2) nucleation and (3) growth. Initially, Argon (Ar) is used as the purging gas at desired temperatures. Cracking involves dissociation of a hydrocarbon, which breaks down to hydrogen atoms, carbon atoms and other carbon species. Upon the dissociation of hydrocarbon (C_2H_2), the concentration of carbon atoms and carbon species increases due to the influence of high temperature and pressure. High temperature and pressure alter the carbon atoms, molecules and and/ or ions concentration which can lead aggregation [43]. The carbon species grow up as the reaction proceeds, and this is called nucleation. The nucleated carbon species in the last step polymerize in an inert atmosphere, in the growth stage. Moreover, nucleated carbon species adsorb other carbon atoms or species on the surface and realize polymerization during cooling and this leads to the formation of CNOs [43].

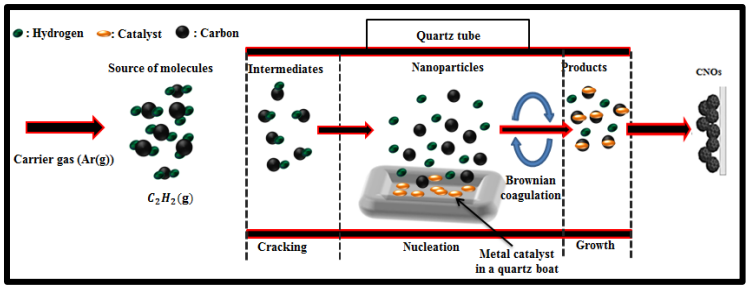

Scheme 2.3: Shows the synthesis mechanism (stages) of the CNOs growth through a bottom-up approach [43].

When this reaction mechanism is adhered to, quasi-spherical CNOs are formed. The microstructural features of the as-prepared CNOs with average particle size less than 100 nm can be observed in which the quasi-spherical CNOs particles are agglomerated in an interconnected network structure as seen in **Fig. 2.2a**. However, more than one core may be present in the CNO structure which indicates that the growth mechanism can involve multiple nucleation centers [44].

The micrographs in **Fig. 2.1b** show that purified and unpurified CNOs have different nanostructural features. The unpurified CNOs (as-synthesized) exhibit core-shelled nanostructural features. It was reported by Su et al [45], that when catalysts, such as those made of Fe, nickel (Ni), and chromium (Cr) are used to prepare CNOs, the metal nanoparticles can be at the core of CNOs. The hollow nanostructures appear after purification (e.g. through concentrated acid treatment) [45].

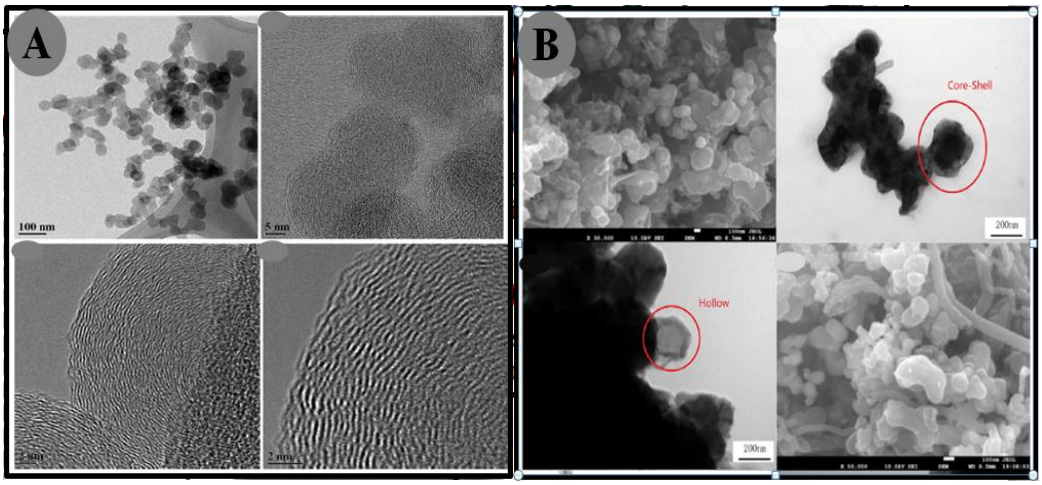

Figure 2.2: The reported micrographs of CNOs (a) HRTEM images [35], (b) SEM and TEM images [46].

2.6. Overview of photovoltaic (solar) cells fabrication using carbon nanostructured materials

2.6.1. History of photovoltaic cells

Alexandre Edmond Becquere observed the photovoltaic (PV) effect in 1839 [47]. His observations were through an electrode in a conductive solution exposed to light and that is when the theory of PV started. The PV history is mainly divided into three time periods. The first

period was during the discovery years from 1839 to 1904 whereby in 1877, William Adams and Richard Day observed the PV effect in solidified selenium and in 1904, Wilhelm Ludwig Franz Hallwachs made a semiconductor-junction photovoltaic cell with copper & copper oxide[48]. However, the real understanding of the science behind the operation of these first PV devices was still missing at this point.

The second period was the theoretical foundation for PV device operation formulation from 1905 to 1950 [49]. The key events in the second period were Einstein's photon theory, the adaptation of the Czochralski crystal growth method for single crystal silicon and germanium growth and the development of band theory for high purity single crystal semiconductors. The importance of high purity single crystal semiconductors for high efficiency photovoltaic cells was then emphasized by the developed photovoltaic cells (PVCs) theory. These developments laid the foundations for the 3rd phase of PV device development between 1950 and 1959 which lead to the practical silicon single-crystal PV device. The Bell labs announcement of the PVC in 1954 with the Pearson, Chapin, and Fuller patent in 1957 for the 8% efficient silicon photovoltaic cell was the key event in the history of PVCs [49].

2.6.2. The chemistry of solar cells

A photovoltaic cell also known as solar cell is an electrical device that converts the energy of light directly into electricity by the photovoltaic effect, which is a physical and chemical phenomenon. It is a form of photoelectric cell, defined as a device whose electrical characteristics, such as current, voltage, or resistance, vary when exposed to light [49]. The basic operation of photovoltaic cells (PVCs) requires three basic attributes: (1) The absorption of light, generating electron-hole pairs or exactions, (2) The separation of charge carriers of opposite types, (3) The separate extraction of those carriers to an external circuit [50].

There are different PVCs based on their structural architecture [51]. In this study we focus on dye sensitized solar cells (DSSCs), also referred to as dye sensitised cells. They were firstly invented by Professor Michael Gräetzel and Dr Brian O'Regan hence is often referred to as the Gräetzel cell (GCs) [52]. These types of cells fall in the third generation of PVCs. They are advanced cells which can be linked to the artificial photosynthesis by the way they replicate the

effects of nature's absorption of light energy. GCs technology is forming part of modern technologies used to produce electrical energy in a wide range of light conditions, indoors and outdoors. Moreover, they are low-costing PVCs belonging to the group of thin film photovoltaic cells.

The GCs working principle is based on a semiconductor formed between a photo-sensitized anode and an electrolyte. They have a number of attractive features; it is simple to make using conventional roll-printing techniques, is semi-flexible and semi-transparent which offers a variety of uses not applicable to glass-based systems, and most of the materials used are low cost. Each cell fabrication can be done with a pair of carbon-based electrodes using transparent, conductive carbon nanostructured materials (CNMs) as the working electrode with a bilayer of conductive CNMs and carbon black as the counter electrode. However, the improved efficiency can be attributed to the inhibition of the mass recombination at the working electrode/electrolyte interface and the acceleration of the electron transfer kinetics at the counter electrode by carbon black [53].

Normally platinum (Pt) catalytic layer is extremely important in GCs for the regeneration of the dyes after excitation of electrons [54]. The use precious platinum (Pt) metal as the catalyst for in GCs also assists in completing the circulation of electrons in the entire device. However, Pt is very expensive and corroded gradually by electrolytes [55]. This challenge can be addressed by applying popular nanostructured materials such as multi-walled or single-walled carbon nanotubes (CNTs), carbon black, polyaniline and grapheme in solid-state DSC [56].

The GCs are currently the leading photovoltaic device with regards to third generation PVCs because both first and second generation devices suffer the same performance restrictions, such as ‘‘red losses’’ in which photons with energies below the band gap of the device cannot be absorbed and also ‘‘blue losses’’ whereby photons with energies above the band gap lose their excess energy as heat. For optimized GCs, the counter electrode (CE) material must have the lowest possible sheet resistance, excellent catalytic activity for the reduction of the redox electrolyte, high chemical stability and a low cost. The reactions at the CE are dependent on the type of redox mediator used to transfer charge between the photo electrode and the CE. In most cases, the iodide–tri-iodide couple has been employed as the redox mediator and the overall redox reaction in GCs can be described as:

$I_3^- + 2e^- \rightarrow 3I^-$ 2.2

The tri-iodides are produced near the dye-sensitized TiO_2 electrode and reduced at the counter electrode (given by **Eq. 2.2**). The counter electrode can be coated with CNMs for better catalytic purposes as illustrated in **Scheme 2.4**.

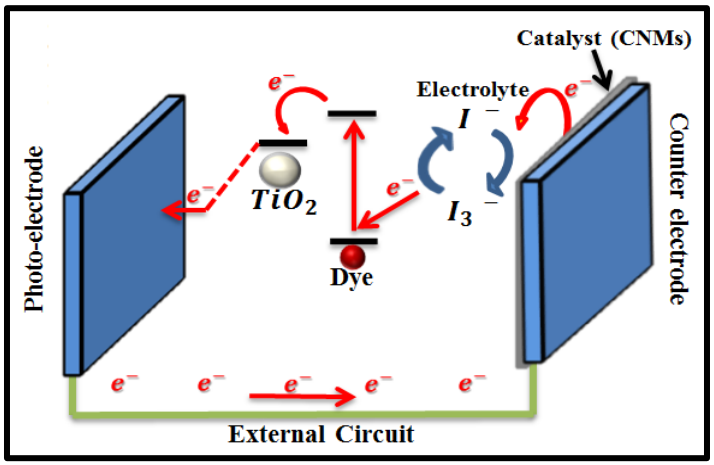

Scheme 2.4: Illustrates the electrons circulation and transfers in the GC [57].

The GCs uses dye complexes and different dyes behaviours have been studied, such as alkoxysilyl anchor dye and a carboxy-anchor organic dye [58]. A combination of light harvesting donor–p–acceptor dyes in conjunction with cobalt-based redox mediators with strong molar absorptivity of the dyes enabled the use of thin titanium dioxide (TiO_2) films. This potentially reduces fabrication costs while minimizing the unfavourable recombination between the electrolyte and the TiO_2 surface [59]. Attention has also been drawn to metal-free organic dyes because of abundant raw materials [60]. Nevertheless, up to now the performance of the GCs with carbon CEs has not been satisfactory and is usually inferior to that of GCs. This remains a challenge of developing GCs made of carbon-based CE with excellent rather better performance. However, the encapsulated metal and nitrogen doped nanomaterials exert a synergistically favourable influence on the CE performance of the GCs [61]. For the purpose of this study, GCs' counter electrode is explored in which carbon nano-onions (CNOs) are candidates chosen for replacing Pt since these nanomaterials have good catalytic properties among others.

2.6.3. Fabrication of solar cells

Since one of the proposed applications for carbon nanomaterials are in the GCs. Typically, the GCs are constructed with fluorine doped tin oxide (FTO) conductive glass/TiO_2 nanoparticle/Ru-based dye/iodine based electrolyte/Pt counter electrode/FTO (see **Scheme 2.5**) [62].

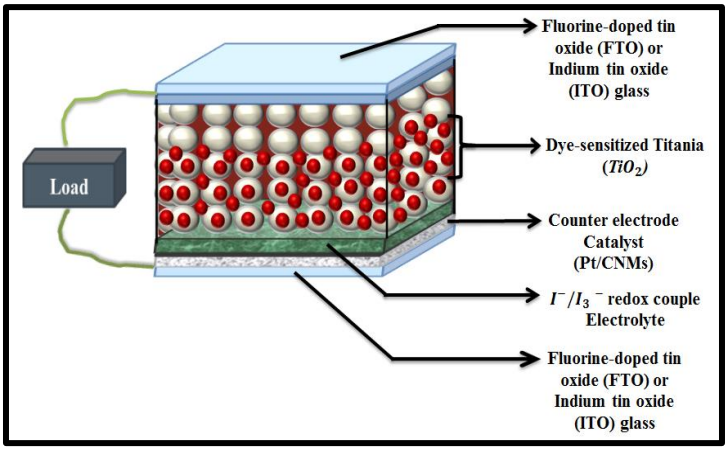

Scheme 2.5: Shows the structural architecture of GC and its basic components [63].

A glass with a fluorinated tin oxide surface layer (SnO2: FTO) is used .The TiO_2 active layer is prepared by doctor-blade method [64]. The electrolyte solution can be used with the preparation of the counter electrode (anode) by sputtering the FTO conductive glass with CNMs (CNOs). [65]. However, the doped carbon network with heteroatoms (e.g., N, B, and P) can introduce electrocatalytic active sites with a minimized change of the conjugation length [66]. Furthermore, heteroatom doping has also been demonstrated to enhance the electrical conductivity and surface hydrophilicity to facilitate charge-transfer and electrolyte– electrode interactions, respectively, and even impart electrocatalytic activities [67].

In GCs, the electrolyte is responsible for charge transport between the photo anode and the counter electrode. Most highly efficient GCs have been constructed with liquid electrolytes with iodide–tri-iodide (I^-/I_3^-) redox couple and volatile organic solvents. The unique performance liquid electrolytes are mainly attributed to, firstly, the favourable penetration into the porous film and, secondly, the fast dye regeneration combined with exceedingly slow recombination. However, the evaporation of toxic solvents and the leakage of liquid electrolytes as well as the sealing problem will significantly limit their practical application. Thus, attempts have been

made to solve the above problems by replacing liquid electrolytes with (quasi) solid-state electrolytes, such as a hole-transport material, ionic liquids, or solid-state composite electrolytes [68].

The CE has the function to transfer electrons arriving from the external circuit to the electrolyte including the redox couple. An effective CE should have the following properties: (1) good catalytic activity (2) chemical/electrochemical stability; and (3) mechanical stability and robustness. These CE properties are required for the cell to work such that measurements can be taken [69].

2.7. Conclusions

Carbon nano-onions (CNOs) can be are grown using various metallic catalysts which are known to have good catalytic activity. It is evident from the previous studies that different CNOs can be formed on a various metal catalysts such as iron metal catalyst and other metal composites. However, not only the catalyst can lead to the desired product since the synthesis temperature has important role and determines the type of carbon material produced.

Different CNMs have selective growth mechanism that varies with the interaction of carbon sources with the metal catalysts. This also allow CNOs to grow following certain proposed reaction schemes. In the absence of a catalyst, decomposition temperature and synthesis period plays an important role in altering the material's properties such as removing the undesired functional groups on the surfaces of the materials (e.g. removal of the carboxyl/hydroxyl groups).

Carbon nano-onions stand a chance to be potential candidates for their use in GCs. Their application and behaviour in the GCs strongly depends on their structural composition and or formation.

References

1. Zener C. *Phys. Rev.* 81 (1951); p 440
2. Su B, Cao Z, Shi Z. *Acc Chem Res*. 48 (2015); p. 887
3. Teja AS, Koh, PY. *j.pcrysgrow*. 55 (2008); p. 22
4. Wu W, He Q, Jiang C. *Nanoscale Research Letters*. 3 (2008); p 397-398
5. Yang Y, Liu X, Yanxing Han Y, et al. *Journal of Nanomaterials.* 2011 (2010); p 1
6. Cui X, Antonietti M, Yu S. *Small.* 2 (2006); p 756
7. Saito Y. *Carbon*. 33 (1995); p 985.
8. Tessonnier JP, Su DS. *ChemSusChem*. 4 (2011); p 830
9. Deck CP, Vecchio K. *Carbon.* 44 (2006); p 267-268
10. Ding F, Larsson P, Larsson JA, et al. *Nano Lett*. 8 (2007); p 464-466
11. Phaahlamohlaka TN. *WIReDspace*. 1 (2013); p 35
12. Iyuke SE, Simate GS. *Nanotechnology and Nanomaterials*. 1 (2011); p 2-3
13. Sarkaria M, Fazlollahib F, H. Atashic H, et al. *Chem. Biochem. Eng. Q.* 27 (2013); p 259-260
14. Singh G, Jalandhara D, Kamlesh Yadav K. *AIP Conference Proceedings.* 1728 (2016); p 2
15. Moisala A, Nasibulin AG, Kauppinen EI. *Journal of Physics: Condensed Matter*. 15 (2003); p 3012-3014
16. Dupuis, A.C. *Progress in Materials Science*. 50 (2005); p 937-938
17. Magrez A, Seo JW, Smajda R, et al. *Materials.* 3 (2010); p 4875-4876
18. Li H, Li Y, Zhang Y, et al. *Nanoscale Res Lett.* 11 (2016); p 1.
19. He C, Zhao N, Shi C, et al. *Scripta Materialia.* 54 (2006); p 1739
20. Zhang C, Li J, Shi C. *Carbon*. 49 (2010); p 1151
21. Gong K, Du F, Xia Z. *Science*. 323 (2009); p 760
22. Galvis HMT, Bitter JH, Khare CB. *Science*. 335 (2012); p 835
23. Zheng N, Stucky GD. *J. Am. Chem. Soc*. 128 (2006); p 14278
24. Shaikjee A, Coville NJ. *j Adv Res.* 125 (2011); p 899
25. Chen L, Wang C, Chen G. *Applied Mechanics and Materials.*184 (2012); p 1294
26. Yang Y, Liu X, Han Y, et al. *Journal of Nanomaterials.* 2011 (2011); p 2
27. Velasquez M, Batiot-Dupeyrat C, Gallego J. *Diamond and Related Materials.* 70 (2016); p 105-106
28. Yang Y, Liu X, Guo X. *Journal of Nanoparticle Research*. 13 (2010); p 1980

29. Mohapatra D, Badrayyana S, Parida S. *Materials Chemistry and Physics.* 174 (2016); p 113
30. Tripathi KM, Tran TS, Kim YJ. *ACS Sustainable Chem. Eng.* 5 (2017); p 3983
31. Dubey P, Tripathi KM, Sonkar SK. *RSC Adv.* 4 (2014); p 5840
32. Sawant SY, Somani RS, Panda AB, et al. *Mater. Lett.* 94 (2013); p 133
33. Ahmed GHG, Laíño RB, Calzón JAG, et al. *Beilstein J. Nanotechnol.* 7 (2016); p 759
34. Huheey JE. *Journal of Physical Chemistry*. 69 (1965); p 3286
35. Maubane MS, Mamo MA, Nxumalo EN, et al. *Synthetic Metals*. 162 (2012); p 2307
36. Ahmed GHG, Laíño RB, Calzón JAG. *Beilstein J. Nanotechnol.* 7 (2016); p 759
37. Zhou Y, Neyerlin K, Olson TS, et al. *Energy & Environmental Science*. 3 (2010); p 1438
38. Lee WJ, Maiti UN, Lee JM. *Chem.Commun.* 50 (2014); p 6819
39. Ugarte D. *Carbon*. 33 (1995); p 991
40. Camisasca A, Giordani S. *Inorganica Chimica Acta.* 468 (2017); p 68
41. Ning X, Li Y, Dong B, et al. *Journal of Catalysis*. 348 (2017); p 100
42. Hobbs RG, Petkov N, Holmes JD. *Chem. Mater*. 24 (2012); p 1975
43. Zhenga Y, Zhu P. RCS Adv. 6 (2016); p 92285
44. Yan L, Yang Y, Ma C, et al. *Carbon*. 109 (2016); p 600
45. Mohapatra D, Badrayyana S, Parida S. *Materials Chemistry and Physics*. 174 (2016); p 114-115
46. Su X, Zhang J, Jia Y, et al. *Journal of Alloys and Compounds.* 695 (2016); p 1422
47. Williums R. *The Journal of Chemical.* 32 (1959); p 1505
48. Jordan DC, Kurtz S.R. *Photovoltaic Degradation Rates — An Analytical Review*. 1 (2012); p.2.
49. L.M Fraas, *Springer International Publishing*. 1 (2014); p 1
50. Askari MB, Abadi VMM, Marhabibi M. *American Journal of Optics and Photonics*. 5 (2015); p 94-95
51. Askari MB, Abadi VMM, Marhabibi M. *American Journal of Optics and Photonics.* 5 (2015); p 94-113
52. Askari MB. *Engineering Physics.* 1 (2017); p 1
53. Askari MB, Abadi VMM, Marhabibi M. *American Journal of Optics and Photonics.* 5 (2015); p 99
54. Roy-Mayhew JD, Bozym DJ, Christian Punckt C, et al. *ACS Nano.* 4 (2010); p 6209

55. Kyaw AKK, Tantang H, Wu T,et al. *Journal of Physics D: Applied Physics.* 45 (2012); p 1-2
56. Wang H, Hu YH. *Energy Environ. Sci*. 5 (2012); p 8182
57. Obotowo IN, Obot IB, Ekpe UJ. *Journal of Molecular Structure*. 1122 (2016); p 82
58. Kakiage K, Aoyama Y, Yano T, et al. *Chem.Commun.* 51 (2015); p 15894
59. Mathew S, Yella A, Gao P, et al. *Nature Chemistry.* 6 (2014); p 242
60. Yao Z, Zhang M, Wu H, et al. *J. Am. Chem. Soc.*137 (2015); p 3799
61. Zheng X, Deng J, Wang N, et al. *Angew Chem Int Ed Engl.* 53 (2014); p 7026
62. Bu IYY. *Solar Energy.* 105 (2014); p 236
63. Costa RD, Lodermeyer F, Casillas R, et al. *Energy Environ. Sci.* 7 (2014); p 1283
64. Velten J, Mozer AJ, Li D, et al. *Nanotechnology*. 23 (2012); p 2-3
65. Susantia D, Nafi' M, Purwaningsiha H, et al. *Procedia Chemistry*. 9 (2013); p 5
66. Xue Y, Liu J, Chen H, et al. *Angew. Chem. Int. Ed.* 51 (2012); p 12124
67. Luo Y, Li D, Meng Q. *Adv. Mater*. 21 (2009); p 4648-4650
68. Wand P, Zakeeruddin SM, Moser JE, et al. *Nature Materials.* 2 (2003); p 402
69. Ge C, Rahman M, Nath NCD, et al. *Bull. Korean Chem*. Soc. 36 (2015); p 8

Chapter 3: Characterisation techniques

3.1. Introduction

This third chapter of the dissertation presents characterisation techniques used in this research project.

Different instruments are usually used to analyse most materials synthesized in various research fields. In the field of material sciences, carbon nanostructured materials (CNMs) are explored by many researchers. With the existence of various spherical nanostructured materials, carbon nano-onions (CNOs) were herein studied using various analytical instruments.

In this study, the prepared CNOs samples were analysed and characterised with an aid of different technical instruments. The instrumental techniques used offered sets of data and this opened channels towards interpretation of the results obtained. Moreover, the data sets obtained offered opportunities to characterize the prepared nanomaterials apart from giving information about their intrinsic properties.

The prepared CNOs were analysed using transmission electron microscopy (TEM) and scanning electron microscopy (SEM) to study their intrinsic and extrinsic structural morphology respectively. The samples were further analysed looking at the elemental composition using the electron probe mapping the distribution of elements in the sample by energy dispersive X-ray spectroscopy (EDS) coupled to TEM.

Powder X-ray diffraction (PXRD/XRD) was used to determine the crystallographic phases and structural nature of CNOs comparing the results obtained with those from EDS. In addition to the XRD results, Fourier transform infrared spectroscopy (FTIR) was used to analyse the chemical bonding such as presence of various functional groups in CNOs' structural surfaces. Moreover, the laser Raman spectroscopy (LRS/RS) was used to study the graphitic nature of the prepared nanomaterials.

The thermal stability of CNOs samples were investigated following the thermogravimetric analysis (TGA) and or differential thermogravimetric analysis (DTGA). The surface area studies were done using Brunauer-Emmett-Teller analysis (BET). The absorption characteristics of the prepared CNOs were investigated using Ultraviolet-visible **(**UV-vis) spectrophotometer.

3.2. Analysis techniques used for prepared CNOs

3.2.1. Powder X-ray diffraction (PXRD) analysis

Powder X-ray diffraction (PXRD) analysis helps mostly in terms of the phase identification of components in the prepared sample. The powder X-ray diffraction analysis technique is usually used to analyse all solid materials both the inorganic and organic solids. The analysis describes the crystalline structure of the sample since every crystalline material is capable of interacting with the X-rays to produce specific diffraction pattern even if is in a mixture [1]. For every given phase of a sample analysed, the area under the peak gives a measure of the quantity of that phase present in the sample. The diffraction pattern of a pure substance is like a fingerprint of that substance, hence the PXRD can distinctively identify and characterise polycrystalline phases. The fingerprint of a substance is derived from the diffraction of X-rays due to the arrangement of atoms which might be arranged in a certain sequence that make up the crystalline form of the solid material. The solid materials can be described as amorphous which can be as the result of disordered and random arrangement of atoms in a solid material. However, atoms can be arranged in a regular manner which might bring a sequential repetition in a three dimensional order describing a solid crystal and eventually the crystallinity of the solid material. The every crystalline structure, the unit cell of the smallest volume of a crystal consists of three axes (a, b, c) with corresponding angles alpha, beta and gamma [1].

In this study, all samples were analysed using a Bruker D2 Phaser PXRD shown in **Fig. 3.1** which uses Co-Kα irradiation and make use of a 30 kV X-ray tube at the current of 30 mA over a $10° \leq 2\theta \leq 90°$ range. The D2 diffractometer uses the Bragg – Brentano geometry with an incident angle defined between the X-ray source and the sample while the diffraction angle 2θ, is defined between the detector and the incident beam [2]. The diffraction vector of the instrument is always normal to the surface of the sample. However, careful sample preparation was required before analysing the sample. In this study, packing preparation method was used. All samples

were packed into a sample holder to gain a flat plane surface which was further pressed with a flat glass plate to attain a smoothened surface with a uniform height.

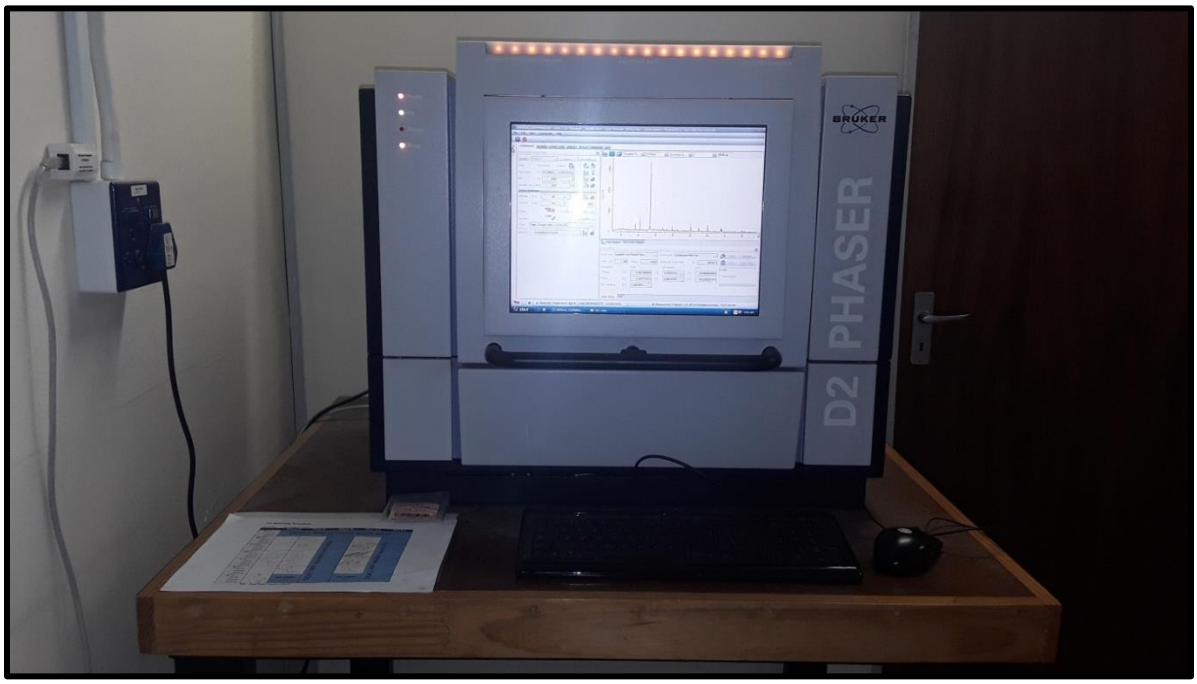

Figure 3.1: The Bruker D2 Phaser PXRD fitted with a LynxEye detector.

Scans were measured over a period of 20 min whereby the sample rotated during scanning. All scans gave out data sets which included: lattice parameters, Miller indices and peak patterns. The obtained peak patterns per scan were identified by searching through an inorganic crystal structure database (ICSD) that matched phases which occurred at their respective 2θ values using a computer evaluation program known as EVA software.

3.2.2. Scanning electron microscopy (SEM) analysis

The extrinsic structural morphology of the CNOs produced was studied using SEM. This is a technique that is used for obtaining images of high resolution which reveals the information about the materials' surfaces. The technique involves scanning a fine beam of electrons over a specimen and detection of the signals which are emitted by the sample. Scanning electron microscope allows the beam of electrons to excite the sample and this generates signals detectable on the two cathode ray tube-types of detectors. The detected signals are then visualised and recorded as the sample's image. The sample's image is as the result of generated

signals displaying the; back-scattered electrons, secondary electrons, sample current and or transmitted electrons [3]. However, there is a secondary electron image is formed by both the secondary electrons and the back-scattered electrons that reach the detector. This is due to the secondary electrons which are generated from within a few nanometres from the surface of the sample. The modern SEM instruments have resolutions of the order of 2 nm and this makes them provide the topological information while being sensitive to the structural surfaces. Moreover, the back-scattered electrons generated within the sample turn to interact much more strongly with the sample allowing the instrument to provide the required compositional and topological information.

A FEI Nova Nanolab 600 FEG-SEM, operated at 30 kV with a spot size of 0.63 nA, as shown in **Fig 3.2**, was used for the purpose of this study. All CNOs samples were analysed to study their detailed morphological structure. The as-synthesised CNOs samples were prepared onto a carbon tape which was mounted on a sample stab. The preparation only involved placing almost a tip of spatula of each sample onto the carbon tape and coating the prepared sample with gold-palladium. The prepared samples are usually charging hence coating with gold-palladium helps to limit the level of charges generated allowing flexible analysis.

Figure 3.2: The FEI Nova Nanolab 600 FEG-SEM/FIB.

3.2.3. Transmission electron microscopy (TEM) analysis

While the extrinsic structural morphology of the CNOs produced were studied using SEM. The intrinsic structural properties of the CNOs produced were studied using TEM is able to generate high resolution images of samples. The resolutions can be as high as 0.5 nm from a high powered beam of electrons accelerated at 120 kV [4]. In this instrument, the electrons are basically generated from the field emission or thermionic sources after which a series of lenses facilitate their collection and focus into the optical path. However, the optical quality of the lenses controls the resolution of the electron microscope even though these lenses can affected by factors such as stigmation as well as spherical and chromatic aberration [5]. The operational mechanism of TEM instrument includes imaging which involves the manipulation of the electrons beam by making use of condenser lenses that focuses the electron beam onto the sample's surface. The strength of the diffraction or projector lens can introduce differences in during imaging [6].

Different types of scattering are produced by the beam-surface interactions and parts of it are transmitted during the analysis. The transmitted electrons are then focused by the objective lens to the image on the charge-coupled device (CCD) camera [7]. The obtained image can be enhanced in its contrast with an aid of objective apertures and be enlarged by down propagation to the column through the intermediate and projector lenses.

Parameters such as crystallinity, diameter measurements, grain arrangement, particle size phase transitions, and structural morphology of the materials can be determined by TEM analysis [5].Using transmission electron microscopy (TEM) also enables the revelation of the finest details of internal structure and the data extrapolations from a series of reaction products can be used to determine a step-by-step mechanism of the reaction process [5].

In this study, a FEI Tecnai T12 transmission electron microscope (Shown in **Fig. 3.3**) was used to characterise the intrinsic morphological properties and characteristics of CNOs produced. The preparation of the sample included a number of steps. About 1 mg of a sample was analysed using TEM by placing the sample in a glass vial containing 5 mL of ethanol. The mixture was then sonicated for 20 min in order to disperse the sample and also to attain a homogeneous suspension of CNOs in the solvent. A drop of the suspension was then spread on a copper grid

(Structure Probe, Inc. (SPI) carbon copper grid (200 mesh), and then it was allowed to dry at room temperature. The grid was then mounted onto an exchange rod of the instrument's sample holder and placed into the instrument's chamber and then analysed.

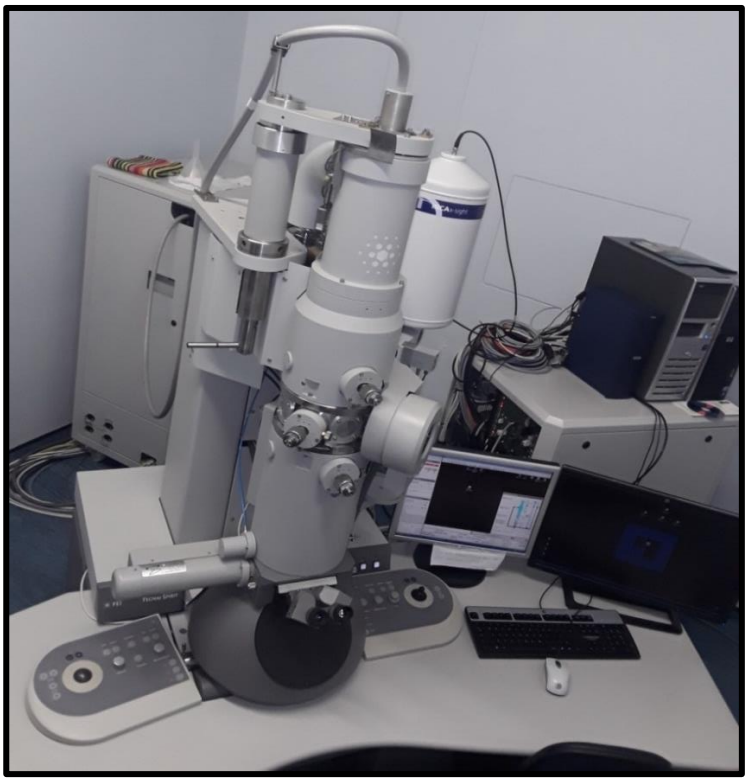

Figure 3.3: The FEI TECNAI T12 transmission electron microscope (TEM).

3.2.4. Energy dispersive X-ray spectroscopy (EDS)

Coupled with TEM analysis, energy dispersive X-ray spectroscopy (EDS) analysis was done for the prepared samples. The energy dispersive X-ray spectroscopy (EDS) analysis is a technique that involves scanning the X-rays generated from the interaction of an electron beam with a sample. However, some of the X-rays produced have wavelengths and energies that are characteristic of the elements. This allows their distribution and the sample's elemental composition to be determined [8]. The analysis also involves X-rays transmitting energy as they strike a semiconductor crystal. The electrons in this crystal absorb a specific amount of energy, putting them into an excited state. This energy is then converted to an electrical signal which in turn is emitted and amplified. Thereafter the data from the EDS analysis can be presented as: a spectrum, histogram, peak patterns and map images. This technique is useful when acquiring

rapid qualitative analysis of an unknown sample and it can also be used to complement broader analyses such as those from TEM and SEM. In this study, EDS analysis was performed to determine the elemental composition of the CNOs produced. The analysis was done through the TEM instrument hence the samples preparation was similar to those of TEM analysis.

3.2.5. Branauer-Emmett-Teller (BET) surface area analysis

The total surface area of various materials is important for different applications. The specific surface area is a parameter measured on solid materials as the total surface area of a material per unit of mass. The specific surface area (SSA) is usually measured in $m^2\ kg^{-1}$ or $m^2\ g^{-1}$ and serves to determine the characteristic properties of a material in terms of the area covered by the material per given mass. This basic information can be sourced from Branauer-Emmett-Teller **(**BET) analysis, and it has important implications for reaction surfaces of the material. However, the SSA may be determined using different measurement methods such as: (i) adsorption measurements by BET isotherms, (ii) gas permeability, and (iii) calculation from the particle size distribution [9]. Unfortunately, all these methods except for BET, fail to measure much the deep texture of the particles' surface and fine structure of the material's surface. Moreover, measurements may greatly differ due to the substance used in the adsorption process. Branauer-Emmett-Teller surface area analyses make use of nitrogen gas being adsorbed on the surfaces of powdered solids, where the volumes adsorbed are measured at a constant temperature i.e. -195 ºC and the lowest relative pressure [10].

Figure 3.4: The micromeritics RS232 Brunauer -Emmett-Teller (BET) surface area analyser.

In this research work, a Micromeritics Tristar 3000 (RS232) surface area and porosity analyser (**Fig. 3.4)** was used to determine the specific surface area of CNOs in an attempt to gather further information about the dispersity of the materials. CNOs samples were degassed and then analysed. Degassing per sample was done under nitrogen between 150-200 °C for 3 hours followed by analysis measurements are done at -195°C.

3.2.6. Fourier transform infra-red spectroscopy (FTIR) analysis

Different materials absorb light in various regions of the spectrum in distinct ways. However, most materials turn to absorb in the infrared (IR) region. Various absorptions result in changes in the rotational and vibrational modes of the molecules depending on the materials composition, which can be due to their dipole moments changing. Consequently, the absorption frequencies of a material are determined by the vibrational frequencies of the molecules, which turn to influence the efficiency of the infrared photon energy transfer [11]. The measure of the magnitude of the infrared photon energy transfer gives the absorption intensity.

Figure 3.5: Bruker Tensor 27 FTIR analyser.

For the purpose of this study, the Fourier transform infra-red spectroscopy (FTIR) was useful for quantification of several components absorbing in the infrared region. The operation mechanism of the instrument allows quantification of the components present in the sample. This mechanism is characterised by the splitting of a beam into two different paths. Once the beams are allowed

to recombine after interference, the intensity of the output beam is monitored as a function of path difference by using a detector [12].

In this study, a Bruker Tensor 27 FT-IR analyser (**Fig. 3.5**) was used to monitor the presence of different functional groups in every sample analysed. These analyses generated spectra that served as unique molecular fingerprints that were easily distinguished from the absorption patterns of other molecules. Samples were each placed on the instrument's analyser and the transmittance scans was performed producing the IR spectra per sample.

3.2.7. Laser Raman spectroscopy (LRS) analysis

Laser Raman spectral analysis (LRS) is a technique that characterises materials with unique vibrational and crystallographic information that is derived from electronic states and phonon energy dispersion in an electrochemical system of a material [13-15]. This information enables detailed studies of the physical properties that are relevant to electrons and phonons. LRS is commonly used to characterise sp^2 carbons such as: 3D graphite, 2D graphene, 1D carbon nanotubes and 0D fullerenes [16].

Figure 3.6: Bruker Senterra laser Raman spectrometer.

Structural characterisation of graphitic materials provides particularly valuable information about defects, stacking of the graphene layers and the finite sizes of the crystallites parallel and perpendicular to the hexagonal axis. LRS is a comparatively easy, non-destructive, non-contacting and rapid measurement method to examine the inelastic scattering of light from a sample surface at room temperature and ambient pressure. The Raman spectra of graphitic materials are commonly characterised by two dominant spectral features, the G and G′ bands appearing at 1582 cm^{-1} and 2700 cm^{-1}, as well as the D and D′ bands occurring at 1350 cm^{-1} and 1620 cm^{-1} respectively [17].

The laser Raman spectrometer used in this research was a Bruker Senterra (**Fig. 3.6)** fitted with a 50x objective lens for imaging. Here the laser excitation wavelength was set to 532 nm and spectral data were evaluated using OPUS 7.1 software. Detailed studies were carried out on the CVD products synthesised over the various supported catalysts (Au, La, Ni and $LaNi/TiO_2$), under different sets of parametric conditions. These studies were conducted to determine the effect of varying the parametric conditions of synthesis in terms of graphicity and crystallinity of the products.

3.2.8. Thermogravimetric analysis (TGA)

The thermal stability of the CNOs was monitored using a Perkin Elmer Thermogravimetric analyser (TGA)/Differential Thermogravimetric analysis (DTGA) 6000. In a standard run, about 10 mg of CNOs were placed into a high-temperature alumina sample cup that was supported on an analytical balance located in the furnace chamber of the analyser and the sample was heated in air (10 °C/min) from 35°C to 900 °C. Initially the instrument uses nitrogen gas for purging (20 mL/min) while holding at 35°C for 5 minutes.

The basis of TGA is the monitoring of the mass of a material as a function of temperature or time under a controlled temperature and gaseous atmosphere (air and nitrogen). Thermogravimetric analysis fundamentally involves heating a material (sample) and measuring its weight as it is heated or cooled in a furnace. The sample is usually loaded in a specialised alumina crucible supported by an instruments' precision balance that measures its mass loss/gain against temperature or time. The entire measurements give information about the extent of: catalytic

metal residue, decarboxylation, decomposition, oxidation, pyrolysis, solvent water as well as weight percentage ash [18].

In this study TGA was applied in the characterisation of the CNOs synthesised using CCVD and flame pyrolysis method (FP). Herein, TGA is reported as used to determine the mass of any residue that remained from the synthesized CNOs. The composition of the supported catalysts was also analysed as part of CNOs thermal stabilities synthesized from CCVD in which the metal nanoparticle catalysts deposited on a sodium chloride support, whereas those obtained from FP were analysed and considered as samples without catalyst materials. To complement the data from PXRD and Raman analysis, the information from the material's decomposition temperature was useful. The degree of crystallinity was used to distinguish different carbonaceous materials present as compared to the PXRD and Raman data obtained. In this study, a Perkin Elmer TGA Simultaneous analyser STA 6000 Pyris Series (**Fig. 3.7**) was used for all TGA analyses.

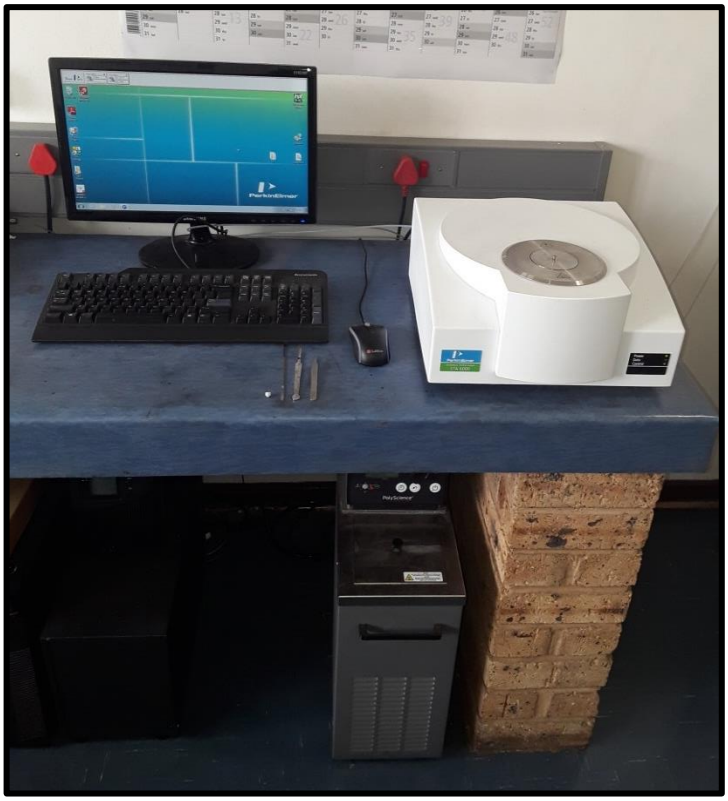

Figure 3.7: TGA thermal analyser used to determine the thermal stability of CNOs.

3.2.9. Ultraviolet – Visible spectroscopy (UV-vis) analysis

In the field of nanoscience, nanomaterials produced gained interest of many researchers for a wide range of applications. However, spectroscopic methods are needed for identification of their molecular structures. UV-vis spectroscopy is the spectroscopic technique usually used to determine concentrations of solution, molecular structures, and purity of compounds and also sizes of nanoparticles [19]. This kind of spectroscopic technique involved a spectrophotometer that comprises of five main components [20].

The first is a light source such as a deuterium lamp hollow cathode lamp, or a tungsten lamp which is used to generate light in the UV, visible or infrared spectral ranges. The second component is a monochromator used or light frequency selection with uniform wavelength from the lamp. Following the monochromator is a specialised sample holding compartment. The compartment fits the cuvettes containing the sample and allow light to pass through them. The photomultiplier is the last component in which the intensity of the light of each monochromatic beam after passing through the sample is detected and or measured in the UV-vis spectral range. The adsorption spectra and the spectral scans are then displayed on a computer.

Figure 3.8: Varian UV-vis spectrophotometer used to determine optical properties of CNOs.

The Varian UV-vis 50 conc. spectrophotometer (**Fig. 3.8**) was used for the purpose of this study, to monitor the absorption wavelength of the CNOs produced. Here absorption of CNOs was monitored by placing samples on glass substrates and exposing the samples to the UV-vis light source. CNOs samples were drop-casted onto the glass substrates and allowed to dry using ethanol as a dispersing medium. Following analysis done by the instrument, the adsorption spectra of CNOs at time (t) were then represented on a computer display [21-22].

References

1. Chatterjee N. *MIT Electron Microprobe Facility*. 1 (2012); p 1-10.
2. Zhao X, Ando Y. *J.Appl.Phys*. 37 (1998); p 4846
3. Reed, S. J. B. *Journal of Research of the National Institute of Standards and Technology*. 107 (2002); p 497–502
4. Masuda, H. *InTech world journal*. (2015); p 3–34
5. D. H. Anjum DH. *Materials Science and Engineering.* 146 (2016); p 4
6. Jackson KW, Chen C. Anal. Chem. 68 (1996), p 231–256
7. Pennycook SJ, Lupini AR, Borisevich A. et al. *Phys. Rev. Lett.* 1 (2014); p 1-5
8. Franklyn, P. J. *Univ. Cambridge*. 27 (2011); p 1-2.
9. A. Trunschke. Modern Methods in Heterogeneous Catalysis Research. 1 2013 p 4
10. Zielinski, J. M. & Kettle, L. *Intertek Chem.Pharm.* 1 (2013); p 1–7
11. Andrievsky GV, Klochkov VK, Bordvuh AB, et al. *Chemical Physics Letters*. 364 (2002); p 8-17
12. Ibrahim, M., Nada, A. & Kamal, DE. *Indian journal of Pure and Applied Physics*. 43 (2005); p 911–917
13. White SN. *Chem. Geol*. 259 (2009); p 240–252
14. Dresselhaus MS, Jorio A, Saito R. *Matter Phys.* 46 (2010); p 89–108.
15. Pimenta MA, Dresselhaus G, Dresselhaus MS, et al. *Physical Chemistry Chemical Physics.* 409 (2007); p 1276–1291
16. M.S. Dresselhaus MS, Jorio A, Saito R. *Rev. Condens. Matter Phys*. 1 (2010); p 90
17. M. A. Pimenta,a G. Dresselhaus,b M. S. Dresselhaus, et al. *Phys. Chem. Chem. Phys*. 9 (2007); p 1276
18. Perkinelmer. *Thermogravimetric Analysis (TGA) A Beginner's Guide*. 1 (1960); p 1-18
19. Haiss W, Thanh NTK, Aveyard J. *Anal.Chem.* 79 (2007); p 4215
20. Haiss W, Thanh NTK, Aveyard J, et al. *Anal. Chem*. 79 (2007); p 788–800
21. Andrievsky, G. V. Comparative analysis 364 (2002); p 8–17
22. Petrasch J, Coray P, Meier A, et al. *J. Sol. Energy Eng*. 129 (2006); p 405-411

Chapter 4: Synthesis of CNOs using catalytic chemical vapour deposition (CCVD) method

4.1. Introduction

This chapter of the dissertation presents results and discussions based on the synthesis of CNOs using a CCVD method.

Since the discovery of fullerenes [1-2], interest in carbon based nanomaterials continues to broaden. Apart from numerous carbon allotropes, other forms of carbon nanomaterials include the nanofibres, nanospheres and nanotubes. These carbon nanostructured materials can be synthesized using different methods such as arc discharge [3], flame pyrolysis [4] and chemical vapour deposition methods [5]. Among the spherical nanostructured materials (such as carbon dots and carbon spheres), carbon nano-onions (CNOs) have also been studied due to their electronic and structural properties. The structural morphologies of CNOs range from polyhedral to spherical [6]. These nanomaterials are commonly known to resemble concentric multi-layered spheres. CNOs can be prepared by various methods including the most promising catalytic chemical vapour deposition method (CCVD). The CCVD method has been considered as inexpensive yielding highly pure CNOs in gram scale [7, 8].

In the CCVD method, different carbon sources can be used to prepare various forms of carbon nanomaterials (CNMs) including CNOs [9-11]. Transition metal nanoparticles are typically used as catalysts for growing CNOs. The first row transitional metals are often used to prepare the different metal catalysts used in CCVD. The metal catalyst preparation requires different catalyst systems such as unsupported and/ or supported metal catalysts. Moreover, various techniques (e.g. incipient wetness impregnation) are involved when preparing supported catalysts, while unsupported catalysts can be prepared by reduction methods among other techniques [12]. Supports such as alumina (Al_2O_3) and calcium carbonate ($CaCO_3$) have been used to prepare supported catalysts when growing CNMs. However, separation of these supports and catalysts from the final products is a challenge. To circumvent this problem, water soluble catalyst supports such as sodium chloride (NaCl) have been used [12]. Sodium chloride is soluble in

water and can be readily separated from the product. It has a low pore volume [13], although it can support iron particles and thus provide for the dispersion of metal particles [14-16]. Acetylene gas (C_2H_2) is often used as a source of carbon in CCVD reactor studies [17].

The metal catalyst composition can vary depending on the precursor source (e.g. $Fe(NO_3)_3 \cdot 9H_2O$) used to prepare the catalyst [18]. The oxides of the metal used are formed during the catalyst preparation. These oxides need to be reduced to obtain the metal in elemental form. In this study, the metal catalyst was reduced by hydrogen gas (H_2). The reduction process gave a desired metal catalyst allowing the decomposition of the C_2H_2.

4.2. Experimental procedure

In this study, CNOs synthesis was carried-out following the experimental procedure reported by Yang et al. [19]. The procedure involved both the catalyst preparation and decomposition of acetylene gas in a catalytic chemical vapour deposition (CCVD) method discussed in **Section 4.2.1 and 4.2.2**.

4.2.1. Starting materials

The iron catalyst was prepared from ferric nitrate (($Fe(NO_3)_3 \cdot 9H_2O$), 97%) and sodium chloride ((NaCl), 99%) purchased from Sigma-Aldrich and were used as received. Argon (Ar, 99.9%), acetylene (C_2H_2, 99.98%) and hydrogen (H_2, 99.98%) were obtained from Afrox and used for CNOs synthesis. Hydrochloric acid (HCl, 36%) was purchased from Sigma-Aldrich while distilled water was used during purification.

4.2.2. Preparation of the supported metal catalyst

The iron catalyst was prepared by dissolving grams (respective wt%) of iron nitrate ($Fe(NO_3)_3 \cdot 9H_2O$) in 50 mL of distilled water. The mass of $Fe(NO_3)_3 \cdot 9H_2O$ was varied from 0.3 g to 1.2 g at 0.3 g intervals. NaCl (14.85 g) was then added slowly to the iron nitrate solution. The homogeneous mixture was stirred for 12 hours while reducing the water content by heating the mixture at 80 °C. The resulting solid catalyst was collected and dried in an oven at 120 °C for an hour. The supported metal catalyst obtained was ground into fine particles and was used to synthesize CNOs. The catalyst was labelled as Fe/NaCl.

The weight percentages of $Fe(NO_3)_3 \cdot 9H_2O$ was varied by keeping the mass of the support constant while changing the mass of $Fe(NO_3)_3 \cdot 9H_2O$. The variation was done to investigate the effect of using different amounts of iron source when preparing the metal catalyst.

4.2.3. Synthesis of CNOs using a supported metal catalyst

The as-prepared supported metal catalyst was employed in the horizontal CCVD reactor to synthesize CNOs (see **Scheme. 4.1)**. In a standard run, about 4.00 g of Fe/NaCl catalyst was placed and spread in a 75 mm long quartz boat, and the boat was then placed in the furnace isothermal zone. In order to maintain the desired heating rate and reaction temperature under specific gas flow rates, the temperature was electronically controlled. The furnace containing the tube was first heated up to 450 °C in 100 mL/min of Ar flow at a heating rate of 10 °C/min for 45 minutes. The catalyst was then reduced in a hydrogen (at 100 mL/min) atmosphere at 450 °C for an hour. After reducing the catalyst, C_2H_2 was passed over the catalyst. The reaction was carried out for an hour by introducing a mixture of C_2H_2 and Ar into the reactor's quartz tube at a flow rate of 30 and 100 mL/min, respectively. However, the C_2H_2 flow rate was varied at 30 mL/min until 120 mL/min. After the growth process, the product was washed with distilled water and treated with concentrated HCl such that the NaCl and residual metal catalyst were removed respectively from the product. The purified product was further annealed, whereby the furnace temperature was raised to 900 °C under an Ar atmosphere at 100 mL/min in order to graphitize the product. The furnace was finally cooled to room temperature in an Ar flow at 100 mL/min and the black-grey CNOs powder was collected after removing the quartz boat from the reactor. The black-grey powder was labelled as pristine CNOs (pCNOs).

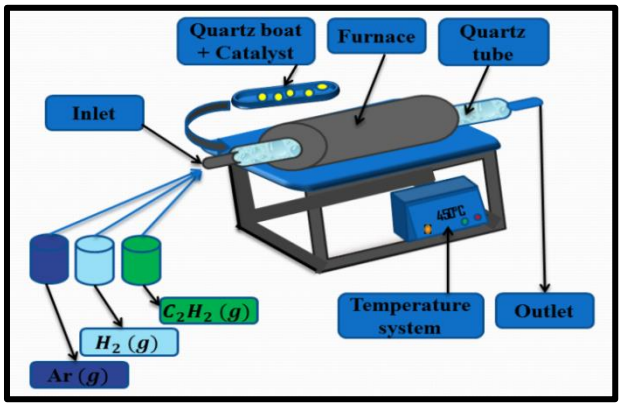

Scheme 4.1: The CCVD reactor set-up used for synthesizing CNOs.

4.2.4. Purification and graphitization of synthesized CNOs

The CCVD process produced CNOs that contained catalyst and impurities (i.e. residual catalyst metal particles and in some cases unwanted carbonaceous by-products). Based on the synthesis temperature used (450 °C), the carbonaceous by-products obtained are carbon nanofibres (CNFs). The NaCl was removed by washing the sample in an appropriate amount of distilled water (100 mL) followed by filtration. CNOs grown using metallic catalysts usually incorporate the metal particles which are necessary for the growth of the onions. The pCNOs incorporating the metal were then purified using concentrated acid. The purification involved placing 1.0 g of pCNOs in 50 mL of 36% hydrochloric acid and sonication of the mixture for 25 minutes in order to disperse the pCNOs. The mixture was allowed to settle for 72 hours at room temperature. The mixture was then diluted with distilled water and the CNOs were collected by filtration (filter paper (MN 615, 150 mm)), followed by subsequent washing with distilled water until the pH was neutral (pH estimations were done using litmus indicator paper). The product was then dried in an oven at 120 °C and collected for further heat treatment. After the growth and purification/washing process, the furnace temperature was raised to 900 °C under Ar atmosphere at 100 mL/min in order to anneal the pCNOs, aiming to further graphitize the nanomaterials. After the graphitization process, the furnace was cooled to room temperature in an Ar flow at 100 mL/min and the black-grey CNOs powder was collected following the removal of the quartz boat from the reactor. The black-grey powder obtained after annealing was labelled as annealed CNOs (aCNOs) and taken for analysis and characterization together with the pCNOs samples.

4.3. Characterization of the CNOs

The morphology of the CNOs was ascertained by transmission electron microscopy (TEM) using a Tecnai Spirit T12 instrument at 120 kV and high-resolution transmission electron microscopy (HRTEM) using a Tecnai G2 30ST at 200 kV. The instrument was coupled with an energy-dispersive X-ray spectroscopy (EDS) detector. About 1 mg of sample was analysed by placing the sample in a glass vial containing 5 mL of ethanol. The mixture was then sonicated for 20 min in order to disperse the sample and also to attain a homogeneous suspension of CNOs in the solvent. A drop of the suspension was then spread on a copper grid (Structure Probe, Inc. (SPI) copper grid (200 mesh), and then it was allowed to dry at room temperature. The grid was then

mounted onto an exchange rod of the instrument's sample holder and placed into the instrument's chamber and analysed.

The external structural composition, morphology and surface topology of CNOs were studied by scanning electron microscopy (SEM) using a FEI Nova 600 instrument at 30 kV. The CNOs sample was analysed with the aid of carbon tape which was stuck onto the aluminium stub. The sample then placed onto the tape and coated with gold/palladium. The stub was then mounted on the instrument's stage, which was moved into the chamber and analysed.

X-ray diffraction (XRD) patterns were collected on a Bruker D2 phaser diffractometer in Bragg-Brentano geometry with a Lynxeye detector using Cu-Kα radiation at 30 kV and 10 mA. The scan range was $10° \leq 2\theta \leq 90°$ in 0.026° steps, using a standard speed with an equivalent counting time of 1 s per step. The diffraction peaks were then compared with those of standard compounds reported in the diffraction plus evaluation package using the EVA (V11.0, rev.0, 2005) software package.

Fourier transform infrared spectroscopy (Bruker Vector 22 FT-IR spectrometer) was used to determine the surface functional groups on the CNOs. A sample was placed on the instrument's analyser and the transmittance scans were performed producing the IR spectra.

The graphitic nature of the CNOs was investigated using Raman spectroscopy (micro-Raman of a Jobin-Yvon T64000 Raman spectrometer). The spot size on the sample was approximately 1.5 μm in diameter. A wavelength of 514.5 nm from an argon ion laser source coupled to a charge coupled detector (CCD) was used to collect the data.

The thermal stability and the differential thermogravimetric analysis of the CNOs were monitored using a Perkin Elmer Thermogravimetric analyser (6000). In a standard run, about 10 mg of CNOs were placed into a high-temperature alumina sample cup that was supported on an analytical balance located in the furnace chamber of the analyser and the sample was heated from 35 °C to 900 °C at 10 °C/min for 90 minutes per analysis.

The Brunauer-Emmett-Teller (BET) analyser was used to determine the surface area and pore volume of CNOs using a Micromeritics Tristar 3000 surface area and porosity analyser. CNOs were degassed at 150-200 ºC and analysed at -195 ºC.

The Ultraviolet-visible **(**UV–vis) absorption spectrum of the resultant sample (CNOs) was monitored using a Varian Cary 500 UV-vis NIR spectrophotometer. The solid sample was sonicated in ethanol to disperse the sample before being drop casted onto the glass substrates for analysis in the spectrophotometer.

4.4. Results and discussion

The results and discussions of the CNOs synthesized by the catalytic chemical vapour deposition (CCVD) method are hereby presented in this section.

4.4.1. Effect of catalyst composition and gas flow rates

Essentially CNOs were made from acetylene decomposed by a metal supported catalyst. This was achieved over Fe catalyst supported on NaCl with specific weight percentage. Different catalyst weight percentages were used to synthesize CNOs. The catalysts used were composed of 0.3, 0.6, 0.9, 1.2 wt% $Fe(NO_3)_3 \cdot 9H_2O$ (see **Table 4.1**).

Table 4.1: Yield of CNOs using different catalyst weight percentages and gas flow rates

C_2H_2 flow rate (mL/min)	**Catalyst wt%**	**Mass of Fe catalyst used (g)**	**Mass of CNOs obtained (g)**	**CNOs % Yield**
60	0.3	4	5.63	40.75
	0.6	4	5.21	30.25
	0.9	4	4.69	17.25
	1.2	4	4.13	3.25
90	0.3	4	5.12	28.00
	0.6	4	4.89	22.25
	0.9	4	4.28	7.00
	1.2	4	4.21	4.75

	0.3	4	4.34	8.50
120	0.6	4	4.29	7.25
	0.9	4	4.19	4.75
	1.2	4	4.11	2.75

The percentage yield of CNOs grown by the CCVD method was determined assuming that all the nitrate $Fe(NO_3)_3$ was converted to iron oxide (FeO) after hydrogen reduction process. The percentage yield resulting from the synthesis of CNOs using different weight percentage of Fe catalyst was calculated for all experiments performed using **Formula 4.1** [20, 21].

$$\text{CNOs yield } (\%) = \frac{m_f - m_i}{m_i} \times 100 \quad \text{..... 4.1}$$

Where m_i is the initial amount of the catalyst and m_f is the total weight of the CNOs sample collected (residual catalyst + deposited carbon).

All reactions were performed under the same temperature conditions (i.e. at 450 ºC) in a horizontal CVD reactor. Due to the better yield of carbon nanomaterials with 0.3 wt% metal loading, the mass of the iron nitrate used had to be < 0.5 g (for ~5 wt%), since metal loadings >0.5 wt% leads to agglomeration of Fe nanoparticles as shown by highlighted areas in **Figs. S2a, b and c**. Better yield was due to the availability of more Fe nanoparticles onto the support. The use of lower metal precursor loading on the support to yield better carbon results is in agreement with the data reported by Yang et al. [19].

The data obtained indicates good reproducibility of CNOs using a CCVD for lower metal loading (for wt% less than 0.5). The results indicate that higher yields of CNOs were obtained with lower flow rates of carbon source (60 mL/min). This was due to more contact time given on the metal surface of the Fe catalyst. During every synthesis, both the carrier (Ar) and reducing (H_2) gas were kept constant at 100 mL/min. H_2 was used as the reducing gas only to avoid the etching effects of hydrogen radicals on carbon atoms which usually suppresses the carbon growth rate [22].

The carbon percentage yields of the obtained nano-onions were based on the mass of the black-grey powder/soot collected as shown in **Table 4.1**. Low carbon yield (8.5 – 2.75%) was obtained at a higher flow rate of the carbon source.

4.4.2. Morphology analysis of the CNOs

The black-grey powder produced in the CVD reactor was characterized using HRTEM in order to investigate the morphological features of the synthesized nano material. The energy-dispersive X-ray spectroscopy (EDS) spectra of the as-prepared nanomaterials (pCNOs) contained different elements with different ratios. The iron particles incorporated in the CNOs structure was identified. Moreover, the results show the presence of a carbon peak confirming the presence of carbon nanomaterials in the sample, as shown in **Fig. 4.1**. The Fe peaks resulted from the Fe/NaCl catalyst used in the formation of CNOs whereas the chlorine and copper peaks are as a result of sodium chloride (NaCl) used as the catalyst support and the copper grid used in the analysis respectively. It is suggested that the onion-like rings form around the catalyst nanoparticles which yields CNOs incorporating the metal nanoparticles [23, 24].

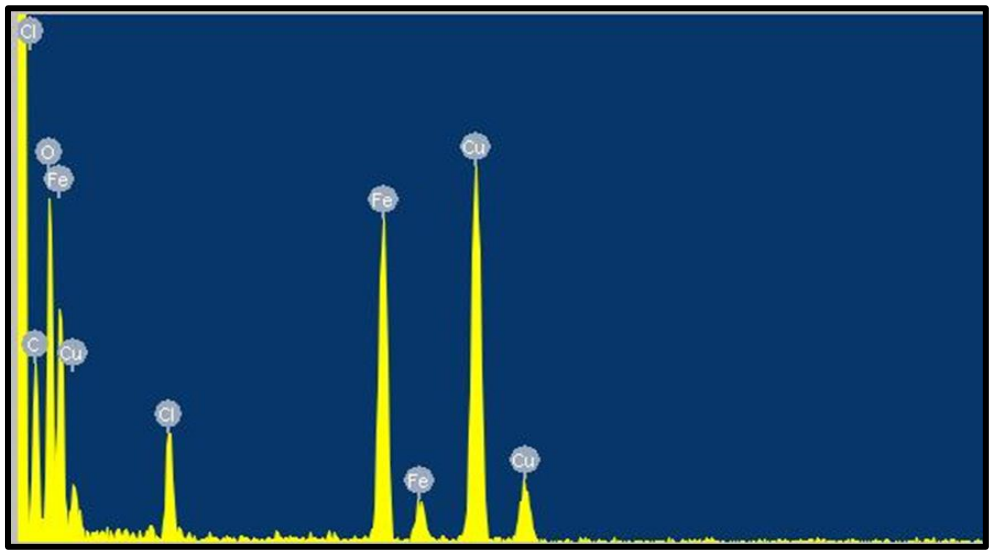

Figure 4.1: EDS spectrum of the pCNOs incorporating the Fe nanoparticles.

The TEM micrographs of the pCNOs revealed that during the synthesis of these nanomaterials, the metal catalyst's nanoparticles form bigger particle sizes due to sintering (**Fig. 4.2a**). The bigger particles give larger CNOs, although less than 100 nm in diameter. The size of the catalyst

particles formed affects the size of the CNOs formed. At 450 °C, CNOs were formed but with long-range ordering due to longer graphitic planes as shown in **Fig. 4.2b**.

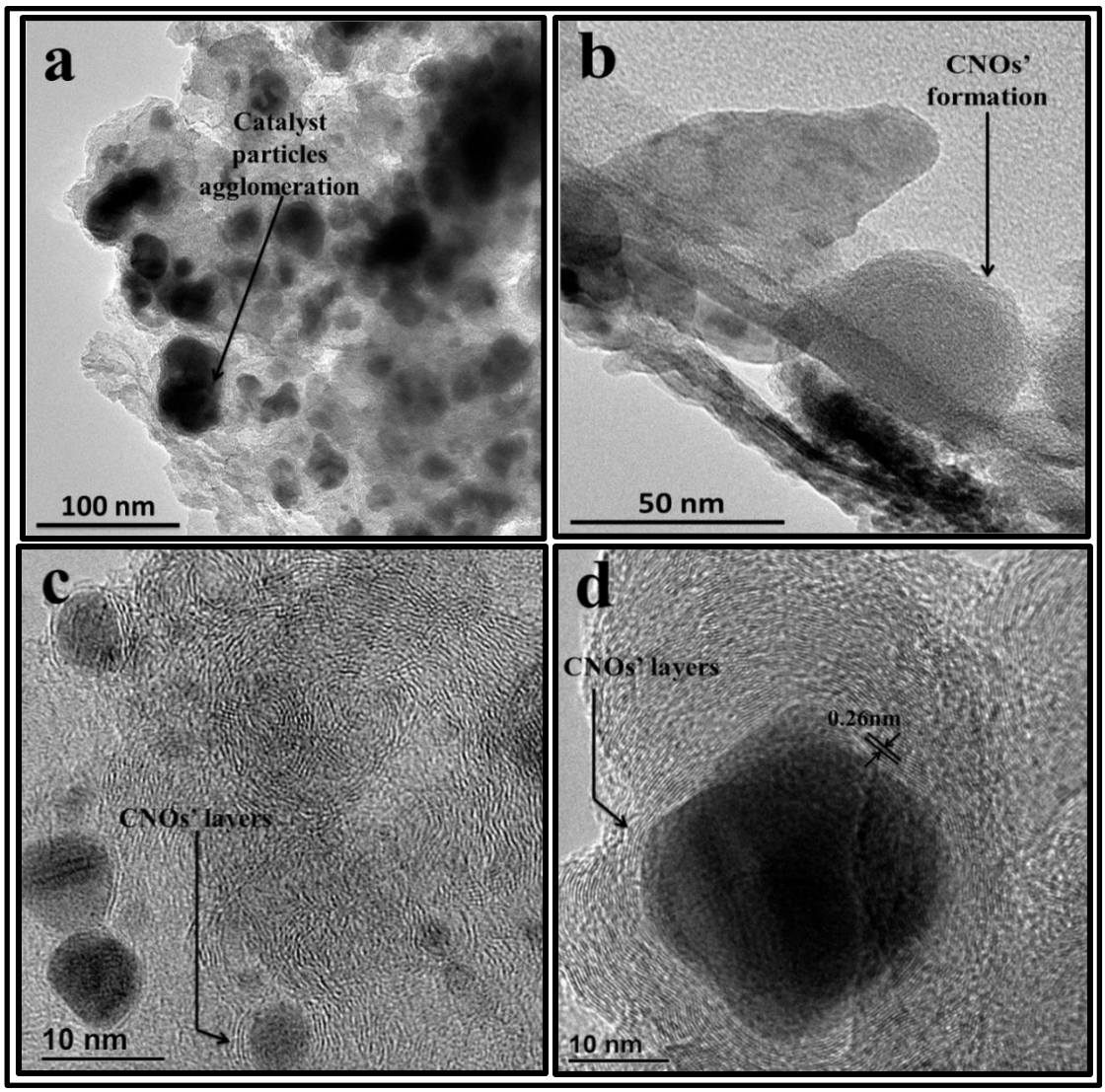

Figure 4.2: TEM micrographs of CNOs; (a, b) pCNOs and (c, d) aCNOs, respectively.

Upon annealing the pCNOs after acid treatment, it was observed that the aCNOs comprised of concentric layers which are quasi-spherical and have a lattice fringe spacing of 0.26 nm as shown by HRTEM micrographs in **Figs. 4.2c** and **d**. These micrographs reveal similar results to those obtained by Zheng and Ahmed [25, 26]. These results show that the carbon nanomaterials formed have an onion-like structure with long-range ordering showing an improved graphitic structure. Moreover, it is evident that the aCNOs formed incorporate metal nanoparticles of different sizes [27]. Carbon nano-onions formed are completely filled with the metal particles in

their core-shells suggested by the Fe peak in the EDS spectrum and shown by dark black portion in the HRTEM micrograph (see **Fig. 4.2d**) [28].

The HRTEM micrographs also reveal that the structural shape of CNOs formed are quasi-spherical. The particle size distribution showed that the most probable particle diameter was less than 100 nm ranging from 12-27 nm (average size ~18 ± 3.6 nm) whereas the number of shells ranged from 4 to 25.

The aCNOs were characterized further using SEM to support the information from HRTEM. As shown in **Figs. 4.3a** and **b**, the SEM micrographs of the aCNOs show that these nanomaterials consist of cores with metal iron nanoparticles (white spots at the core, see arrow in **Fig. 4.3a**) and confirm that they are quasi-spherical [29]. Consistently, undesired nanomaterials formed and are observed as CNFs as seen in **Fig. 4.3b**. The formation of the undesired nanomaterial emerges from the various reaction conditions (such as synthesis temperature, gas flow rates, etc.) used. According to the SEM micrographs, the ratio of CNOs to CNFs is estimated to be 3:1. The presence of CNFs is due to the role of the metal catalyst as shown in **Scheme. 2**.

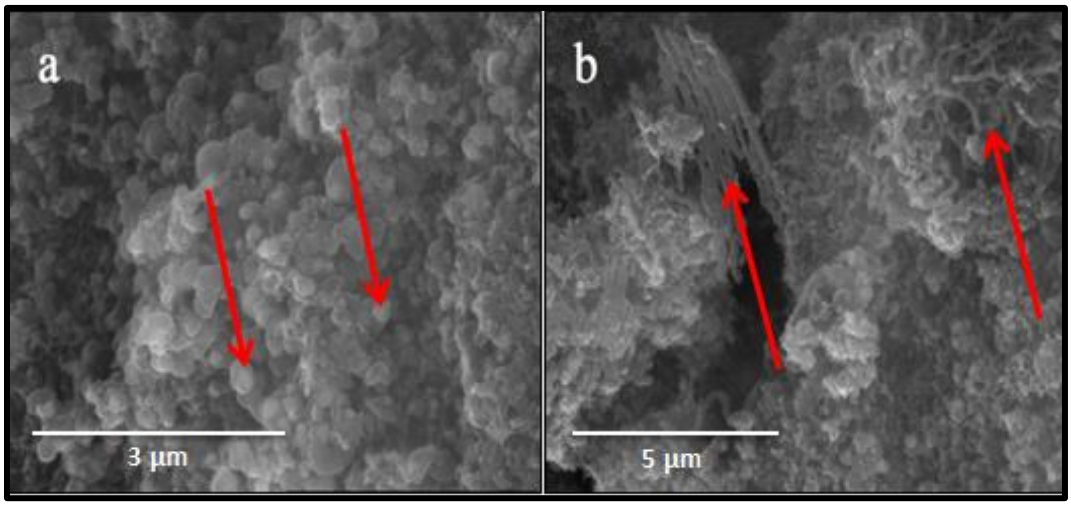

Figure 4.3: SEM Micrographs of CNOs incorporating the metal nanoparticles synthesized using CCVD.

The CCVD growth mechanism of the CNOs and CNFs can be suggested to follow the same routes as reported by Zhang [30]. Based on the HRTEM and SEM results, the proposed growth mechanism for the formation of core-filled CNOs and CNTs is depicted in **Scheme. 4.2**.

In the CCVD growth stage, core-filled CNOs form from the iron particles due to the release of carbon atoms from the C_2H_2 and decomposing effect of Fe catalyst [31]. The Fe catalyst expedited deactivation creates core-filled CNOs from each catalyst particle. The catalyst also decomposes when the reactor is cooled down; this is due to the instability of carbon atoms (as carbide) within the particle at low temperature. During the annealing process, the high temperature (900 °C for 1 hour) causes the expansion and melting on the iron particles. The excess carbon atoms will dissolve in the expanded particles and eventually form the core-filled CNOs.

The nucleation, growth and separation of the CNOs graphitic layers depend on the composition and size of the iron catalyst particles. The iron catalyst particles determine the sizes of the CNOs formed until the carbon proportion is too low to create the formation of more graphitic layers. The growth termination can emerge due to coalescence and/ or Ostwald ripening [30, 32]. The iron particles are also involved in CNFs growth at low temperature. The smaller iron catalyst particles are responsible for nucleation of CNOs whereas they can also promote growth of the CNFs depending of synthesis temperatures [33].

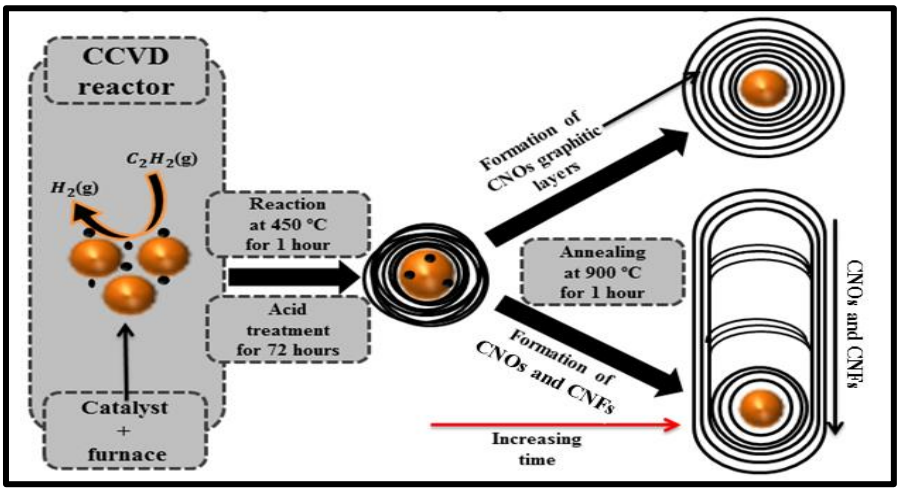

Scheme 4.2: Shows the reaction process for the formation of CNOs and CNFs.

4.4.3. XRD spectroscopy of CNOs

XRD measurements were conducted on the prepared CNOs. The patterns observed, as shown in **Fig. 4.4**, revealed that the as-grown aCNOs were composed of iron oxides which are due to the incorporation or residual metal iron catalyst particles used in the formation of pCNOs. The

ferrous-ferric oxide (magnetite: Fe_3O_4) characteristic peaks were centred at approximately 51.8, 55.7 and 60.4º 2Θ, corresponding to (422), (511) and (440) planes for pCNOs as seen in **Fig. 4.4**. The pCNOs pattern showed carbon peaks centred at approximately 30.4 and 51.8º 2Θ corresponding to (002) and (004) planes of carbon respectively. The sharpness of the pCNOs peak observed around 30.4º 2Θ is due to the presence of large carbon domains [34]. These carbon peaks were also seen in the spectra of the aCNOs. The aCNOs pattern showed and confirmed that carbon materials were formed [35].

The broader carbon peak indicates the long-range structural disorder of the aCNOs [36]. These results show that the aCNOs contains large graphitic carbon domains. However, these materials seem to have traces of the metal catalyst before and after being treated with concentrated acid.

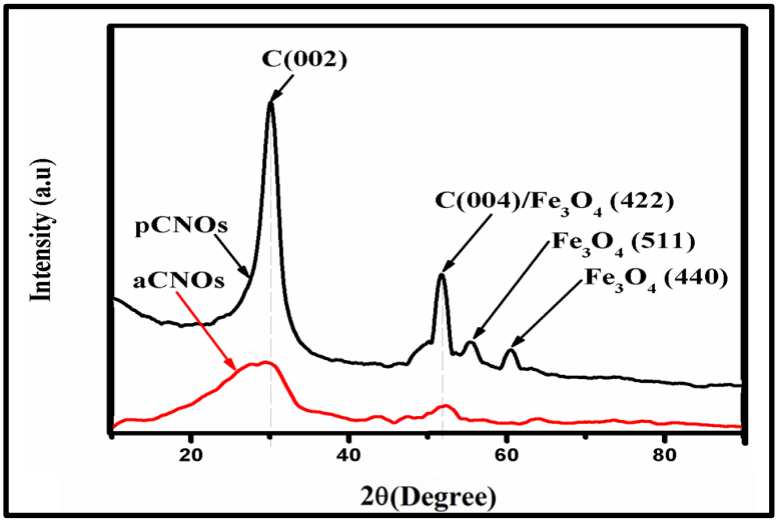

Figure 4.4: Shows the XRD pattern of the synthesized aCNOs and pCNOs.

4.4.4. FTIR spectroscopy of CNOs

The surface functional groups of the CNOs produced were characterized by FTIR spectroscopy. The pCNOs showed a vibration due to the $–CH_2$ bending mode at 1392 cm^{-1} (**Fig. 4.5a)**. In addition, intense C-C stretching bands at 1550, 1236 and 900 cm^{-1}can be found, suggesting more other terminal groups for pCNOs formed. The peak observed around 1789 cm^{-1} suggest the presence of C=O bending mode from the aromatic groups in the structure of CNOs. A strong peaks appearing between 2250 and 2500 cm^{-1} can be attributed to strong CO_2 stretching frequencies.

The aCNOs spectrum show relatively intense vibration of $–CH_2$ at 1478 and 1393 cm^{-1}as shown by the spectrum in **Fig. 4.5b**. The scissoring deformation of $–CH_2$ is also observed around 900 cm^{-1}.

It was also observed that these materials showed an intense C-C stretching bands at 1550, 1243 and 900 cm^{-1} including the broad band around 1857 cm^{-1} may be suggesting the aromatic groups in the structure of aCNOs, which is in good agreement with the HRTEM and Raman results [37]. The peaks appearing between 2350 and 2000 cm^{-1} can be attributed to weak CO_2 stretching frequencies with that of medium C-H stretching frequency observed around 2700 cm^{-1} (circled in **Fig. 4.5**)

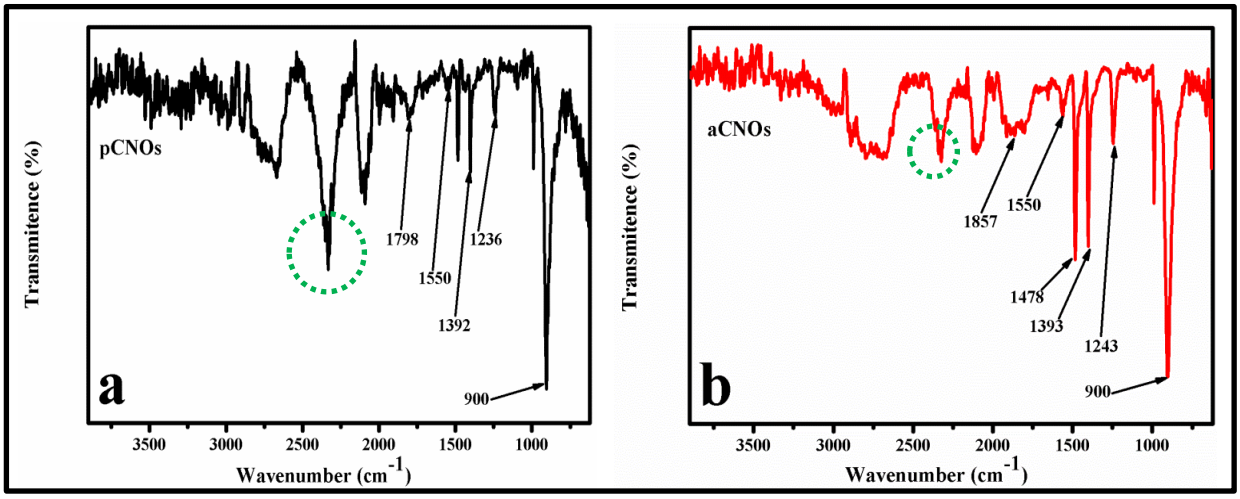

Figure 4.5: FTIR spectrum of; (a) pCNOs and (b) aCNOs synthesized over Fe/NaCl catalyst.

The observed CO_2 peaks in both pCNOs and aCNOs sample analysis can be attributed to the oxygen surface groups of CNOs which decompose to CO and CO_2 during the synthesis and/ or annealing [38]. Moreover, the presence of CO_2 can also be explained by the decomposition of the catalyst precursor into ferric oxide at temperatures < 300 ºC which the oxides are gradually reduced into metallic iron along with the formation of CO_2 (see **Eq. 4.2 and 4.3**) [39].

$4\ Fe(NO_3)_3 \cdot 9H_2O = 2Fe_2O_3 + 12NO_2 + 3O_2 + 36H_2O$ ……...…..4.1

$2Fe_2O_3 + 3C = 4Fe + 3CO_2$ ……..….4.2

$O_2 + C = CO_2$ ……..…...4.3

4.4.5. Raman spectroscopic analysis of CNOs

The Raman spectra of pCNOs and aCNOs showed two prominent peaks, corresponding to D-band and the G-band (**Fig. 4.6**). The position of two broad peaks and the intensity ratios (I_D/I_G) for both samples are summarized in **Table 4.2**.The peaks are ascribed to the D peak for disordered induced by C–C vibration band and the G peak for C=C graphite carbon vibration frequency of the carbon material with sp^2 orbital structure [40].

The I_D/I_G intensity ratios were used to quantify the degree of disorder of the CNOs [41]. The I_D/I_G value of 1.10 implied a low graphitization degree that resulted from the long-range disorder structure of the pCNOs. However, the aCNOs' intensity ratio was 0.93 meaning that the graphitization degree improved correlating with the HRTEM results.

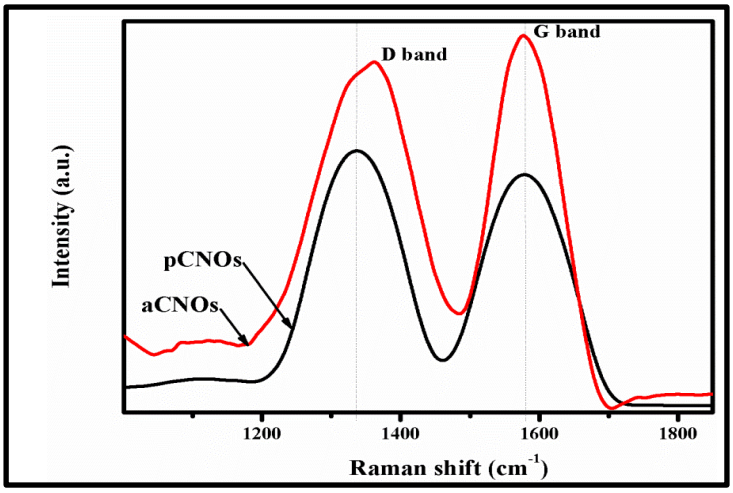

Figure 4.6: Shows Raman spectra of pCNOs and aCNOs synthesized at 450 °C and 900 °C respectively.

Table 4.2: Summarizes Raman data of pCNOs and aCNOs

	D band		**G band**		
Sample	Raman shift cm^{-1}	Intensity	Raman shift cm^{-1}	Intensity	**I_D/I_G**
PCNOs	1333.3	27.3	1580.1	24.8	1.10
ACNOs	1361.9	36.7	1577.5	39.4	0.93

When comparing the D-band of aCNOs to that of pCNOs, an up-shift of the band was observed. This can be attributed to structural deformations and the disorderliness of the carbon lattice induced by the incorporated metal catalyst nanoparticles in the core of the nano-onions [42]. These defects are caused disruptions in sp^2 bonding, due to dangling bonds, sp^3 bonding, vacancies, and carbon rings [43]. A down-shift of the G-band was also observed which is due to structural disorder (distortion of the multi-layers).

4.4.6. TGA of the CNOs

The thermal stability of the nanomaterials was studied. It was noted that the onset decomposition temperature of pCNOs was at 510 °C and that of aCNOs was at 443 °C with the derivative peak centred at 588 °C and 608 °C respectively as shown in **Figs. 4.7a** and **b**. The pCNOs were observed to be less stable than the aCNOs. This might be due to the presence of additional amorphous carbon in the pCNOs materials. The higher thermal stability of the aCNOs indicated the presence of less structural defects, which is consistent with the Raman results. The broader first order derivative peak for the pCNOs is due to structural disorder or distortions since the materials were prepared at lower temperature but annealed after acid treatment to attain better graphitic layered CNOs [44].

Upon acid treatment and annealing, the aCNOs had 8.8% of the residual metal catalyst from 10.8% of the pCNOs residual metal catalyst which showed that aCNOs contained less metal catalyst residue (see **Fig. 4.7a**).

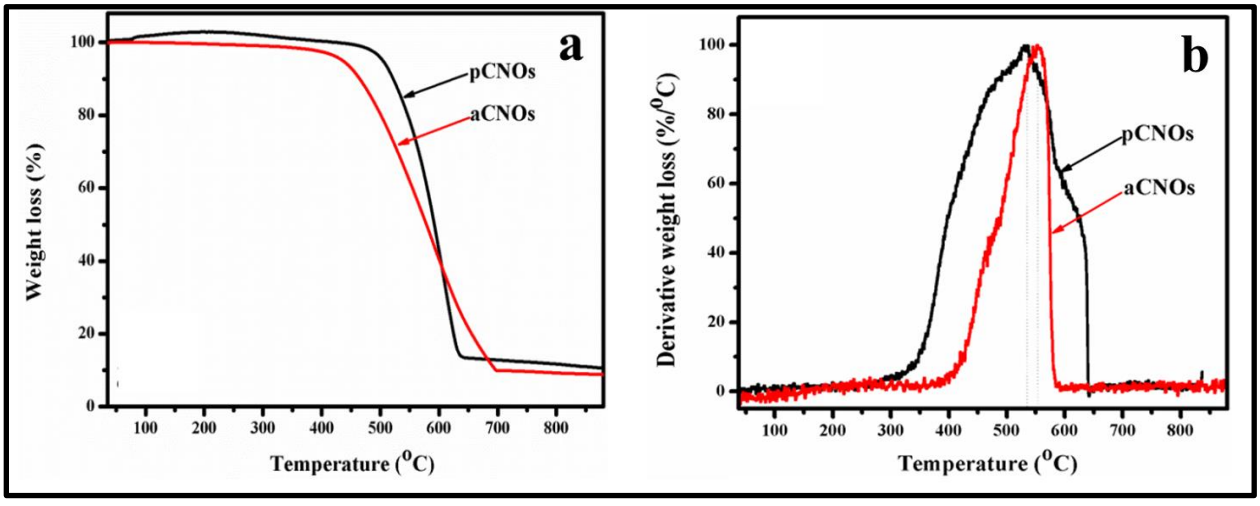

Figure 4.7: Shows the percentage weight loss as a function of temperature, (a) TGA of pCNOs and aCNOs and (b) DTGA of pCNOs and aCNOs.

The CNOs surface area was found to be ~63.00 m^2/g and ~69.50 m^2/g for pCNOs and aCNOs respectively. These results show that CNOs have higher surface area compared to that of carbon spheres prepared by chemical vapour deposition method and the values are comparable to those reported in the literature by Lian et al [45, 46].

4.4.7. UV-vis absorption spectrum of CNOs

The UV-vis spectra of CNOs are shown in **Fig. 4.8**. The spectra show that pCNOs absorb in the ultraviolet region tailing up to ~800 nm. A broad absorption peak at ~309 nm also indicates that the materials synthesized absorb ultraviolet light since this peak is below the visible region (<400 nm). Similarly, aCNOs seem to absorb light in the ultraviolet region. However, the peak at ~309 nm is less broad than that of the pCNOs at ~302 nm. This might be due to different structural orderliness of the CNOs introduced by different surface functional groups. The presence of the small peak at ~232 nm is due to the optical properties of iron oxide nanoparticles incorporated in the aCNOs cores [47].

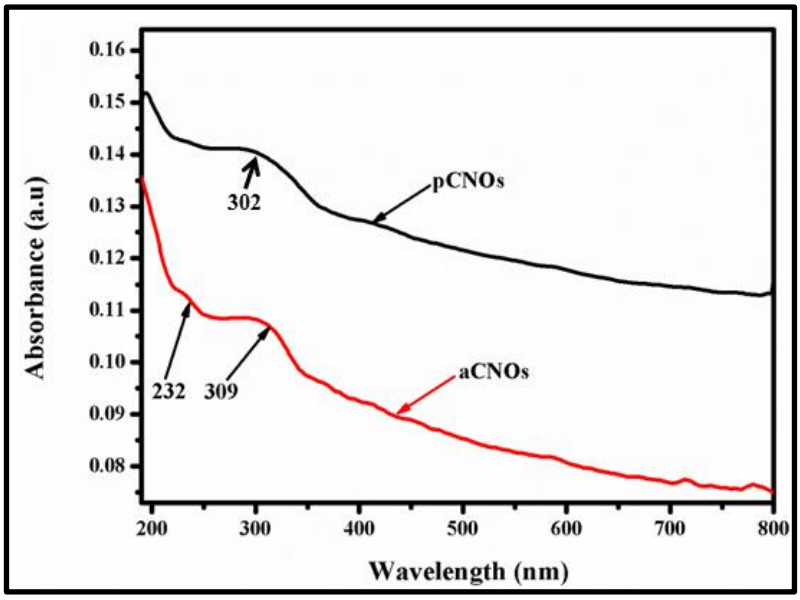

Figure 4.8: UV-vis absorption spectrum of annealed CNOs (aCNOs) and pristine CNOs (pCNOs).

4.4.8. Conclusions

The synthesized CNOs incorporate metal nanoparticle(s) and also exhibit concentric layers ranging from 4 to 25 shells with the shape similar to those reported by Lian et al [48]. The materials formed showed better graphitization after high temperature treatment. There is no evidence of CNOs at lower temperatures (i.e. < 450 ºC). This can be due to poor catalytic activity of Fe catalyst limiting C_2H_2 decomposition. Larger catalyst particles form bigger CNOs whereas smaller particles produce CNOs with smaller diameters. The use of higher amount metal precursor can also lead to metal nanoparticles agglomeration which might retard CNOs formation and or form bigger CNOs.

CNOs have potential to absorb in the UV-vis region which the character is granting them an advantage to be used for various electronics application [49].

References

1. Flavin K, Chaur MN, Echegoyen L. *Org. Lett*. 12 (2009); p 840
2. Harris PJF, Hernández E, Yakobson BI. *Am. J. Phys*. 1 (2004); p 415
3. Bu IYY. *Solar energy.* 105 (2014); p 236
4. Tripathi KM, Bhati A, Singh A, et al. *RSC Adv.* 6 (2016); p 37322
5. Zhang C, Li J, Liu E, et al. *Carbon* 50 (2012); p 3513
6. Gubarevich AV, Kitamura J, Usuba S, et al. *Carbon.* 41 (2003); p 2603
7. He C, Zhao N, Shi C, et al. *Scripta Materialia*. 54 (2006); p 1739
8. Zhang C, Li J, Shi C, et al. *Carbon*. 49 (2010); p 1151
9. Hafner JH, Bronikowski MJ, Azamian BR, et al. *Chemical Physics Letters*. 296 (1998); p 195
10. Bok-Badura J, Jakóbik-Kolon A, Turek M, et al. *Nanomaterials: Applications & Properties (NAP-2015): Proceedings of the International Conference*. 4 (2015); p 1
11. Wang B, Tian C, Wang L, et al. *Nanotechnology*. 21 (2009); p 2
12. Velasquez M, Batiot-Dupeyrat C, Gallego J. *Diamond and Related Materials*. 70 (2016); p 105-106
13. Yang Y, Liu X, Guo X. *Journal of Nanoparticle Research*. 13 (2011); p 1980
14. Chen L, Wang C, Chen G. *Applied Mechanics and Materials.* 184-185 (2012); p 1294
15. Yang Y, Liu X, Han Y, et al. *Journal of Nanomaterials.* 2011 (2011); p 2
16. Velasquez M, Catherine Batiot-Dupeyrat C, Gallego J. *Diamond and Related Materials.* 70 (2016); p 105-106
17. Yang Y, Liu X, Han Y, et al. *Journal of Nanomaterials*. 2011 (2011); p 2
18. Chen B, Parker II G, Han J, et al. *Chem. Mater.* 14 (2002); p 1893-1894
19. Yang Y, Liu X, Guo X et al. *Journal of Nanoparticle Research.* 13 (2011); p 1981
20. Bhoware S, Maubane MS, Phaahlamohlaka T, *Chemical Physics Letters*. 577 (2013); p 72
21. Kathyayini H, Nagaraju N, Fonseca A, et al. *J. Mol. Cat. Chemical A.* 223 (2004); p 129
22. Young LT, Han JH, Hong CS, et al. *Diamond and Related Materials.* 12 (2003); p 851-855
23. Yang Y, Liu X, Yanxing Han Y, et al. *Journal of Nanomaterials*. 2011 (2011); p 2
24. Liu XG, Wang C, Yang Y, Et al. *Chinese Science Bulletin*. 54 (2009); p 139
25. Zheng Y, Zhu P. *RSC Adv*. 6 (2016); p 92289
26. Ahmed GHG, Laíño RB, Calzón JAG. *Beilstein J. Nanotechnol.* 7 (2016); p 760
27. Wang X, Xu B, Liu X. *Diamond & Related Materials*. 15 (2006); p 148

28. Somani SP, Somani PR, Noda M, et al. *Diamond & Related Materials*. 17 (2008); p 579
29. Su X, Zhang J, Jia Y, et al. *Journal of Alloys and Compounds.* 695 (2016); p 1422
30. Zhang C, Li J, Liu E, et al. *Carbon.* 50 (2012); p 3518
31. Zhang C, Li J, Liu E, et al. *Carbon*. 50 (2012); p 3515
32. Tharani K, Nehru LC. *International Journal of Advanced Research in Physical Science.* 2 (2015); p 48
33. Velasquez M, Batiot-Dupeyrat C, Gallego J, et al. *Diamond and Related Materials. 70 (2016); p 105*
34. Chiou J, Lai B, Hsu K, Dong-Hwang Chen. *Journal of Hazardous Materials*. 248-249 (2013); p 395
35. Pol VG, Thackeray MM. *Energy & Environmental Science*. 4 (2010); p 1906
36. Han FD, Yao B, Bai Y. *J. Phys. Chem. C.* 115 (2011), p 8924
37. Pasha MA, Fakhroueian Z, Shafiekhani A, et al. *Materials Science-Poland.* 229 (2011); p 155
38. Prado-burguete C, Linares~olano A, Rodriguez-reinoso F, et al. *Journal of catalysis.* 115 (1989); p 100
39. Wentao Lian, Huaihe Song*, Xiaohong Chen. *Carbon*. 46 (2008); p 527
40. Saleh TA. *Carbon.* 1 (2013); p 482
41. Yan L, Yang Y, Chang QM. *Carbon*. 109 (2016); p 601
42. Matsoso BJ, Kamalakannan Ranganathan K, Mutuma BK, et al. *RSC Adv*. 6 (2016); p 106917
43. Tripathi KM, Bhati A, Singh A, et al. *RSC Adv*. 6 (2016); p 37321
44. Maubane MS. *WIReDspace*. 1 (2010); p 76-77
45. Xiong H, Moyo M, Motchelaho MA, et al. *Journal of Catalysis*. 311 (2014); p 82
46. Wentao Lian, Huaihe Song*, Xiaohong Chen. *Carbon*. 46 (2008); p 528
47. Tharani K, Nehru LC. *International Journal of Advanced Research in Physical Science*. 2 (2015); p 49
48. Wentao Lian, Huaihe Song*, Xiaohong Chen. *Carbon*. 46 (2008); p 529
49. Vasilios Georgakilas V, Guldi DM, Signorini R. *J. Am. Chem. Soc*. 125 (2003); p 14269

Chapter 5: Synthesis of CNOs using Ghee flame pyrolysis (GFP) method

5.1. Introduction

This chapter of the dissertation presents results and discussions based on the synthesis of CNOs using a GFP method.

Spherical carbon nanostructured materials (SCNMs) have continued to receive attention in the research field. The most common SCNMs include carbon dots, carbon nano-onions (CNOs), and carbon spheres. Researchers have shown that over the past decade, different methods have been employed to synthesize CNOs which include catalytic chemical vapour deposition method (CCVD) [1]. However, CCVD use different transition metal catalysts for growing CNOs which is one of the challenges apart from using expensive manufacturing equipment/materials. The use of metal catalysts involves treating the as-synthesized nanomaterials with concentrated acids (e.g. nitric acid) when removing residual metal catalyst nanoparticles which is one of the drawbacks. The CCVD has been explored for its ability to control the diameter and the type of the carbon nanostructured materials (CNMs) [2].

Apart from using CCVD to synthesize CNOs, other methods such as arch discharge, laser ablation and electron beam irradiation have been reported as methods that can be used to synthesize various carbon nanomaterials [3-5]. Recently, various carbon precursors have been used for the synthesis of CNOs. For instance, Ahmed, et al. [6], reported on use of carrots and tomatoes as a carbon source for generation of CNOs. Moreover, catalyst free traditional flame synthesis method is among the promising processes due to its simplicity and continuous production of CNOs in air without complexity. This method is inexpensive and less intricate to yield larger quantities of CNOs [7]. The CNOs synthesized by this method possess structural morphologies which exhibit concentric multi-layers in spherical shapes [8]. Thus, the catalyst free method has an advantage over the others due to lessened contamination and production costs of CNOs.

Flame pyrolysis methods (FP) of liquid fuels (e.g. ghee oil, flaxseed oil and paraffin oil) have been used in the traditional flame pyrolysis processes and have shown a good yield of CNOs [9-11]. The CNOs obtained from this method are free of any catalyst, with less or without contaminant (s). The FP can be compared with CCVD, whereby it is considerably facile and inexpensive with an ability to produce CNOs of high purity.

Taking advantage of the highly pure CNOs which can be synthesized through FP, the as-synthesized materials can be functionalized to tailor their structural properties. In comparison with other carbon nanomaterials such as carbon nanotubes (CNTs), the electronic properties of CNOs can be altered by doping the materials with various heteroatoms such as boron (B) or nitrogen (N) atoms which substitute the carbon atoms of the nanomaterials. In case of nitrogen doping (N-doping), the N-configurations within the carbon matrix can be different (i.e. pyridinic or pyrrolic). In pyridinic-N, pyrrolic-N, oxidized pyridinic-N the N atoms attach either on a five or six membered ring. It is also possible for the N atoms to attach on the edges of the rings while attaching to oxygen or hydroxyl group for the substitution of C with N (graphitic-N) [12]. The substitution by the heteroatoms will generate either p-type or n-type material, respectively [13]. Doped CNOs can be applied in rechargeable lithium ion batteries and also in dye sensitized solar cells (DSCs) as a catalyst in the counter electrode of the cell [14, 15]. However, there are other functional groups or heteroatoms which can be introduced into the structural matrix of the CNOs other than B and or N [16].

For the purpose of this study, we aimed at synthesizing and doping CNOs with nitrogen. The ex-situ doping process was preferred over an in-situ process. This preference was because the materials were firstly synthesized by pyrolysing flame generated from the ghee oil in contrast to the CCVD. The objective for doping CNOs with N atoms was to modify the overall catalytic activity as well as selectivity of a catalyst for DSCs [17].

During the synthesis, ghee acted as the fuel source for the flame generation and the method was deemed as ghee flame pyrolysis (GFP). Apart from the fact that ghee has been used for centuries as a food product, it was hereby used as the flame's fuel because of its composition. It is mainly composed of fatty acids, unsaturated and saturated fats together with Vitamin (Retinol:$C_{20}H_{30}O$),

E (Tocopherol:$C_{29}H_{50}O_2$) and K (Phytomenadione:$C_{31}H_{46}O_2$) which can be suggested as carbon sources due to their long carbon chained molecular structures with the presence of some aromatic rings [18,19] as illustrated in **Scheme. 5.1**.

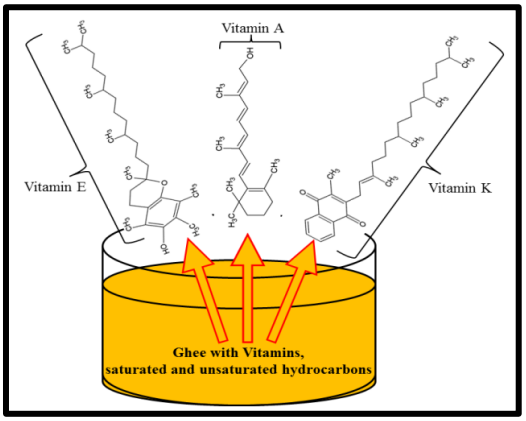

Scheme 5.1: Illustrates different vitamin components in Ghee [20-23].

5.2. Experimental procedure

5.2.1. Starting materials

The CNOs were prepared from ghee butter and fiber wick purchased from local market (Checkers). A flat polished glass plate (260×260×5 mm) and a flat brass plate (260×260×1.5 mm) were used to collect the soot containing the CNOs. Steel tubes stand was designed to hold each plate with a tray. The synthesis of CNOs was carried out using the GFP with the set-up as shown in **Scheme. 5.2**. Liquid ammonia ((NH_3), 98%) was purchased from Sigma-Aldrich. Argon (Ar, 99%), was obtained from Afrox and used for CNOs doping process (discussed in **Section 2.4**).

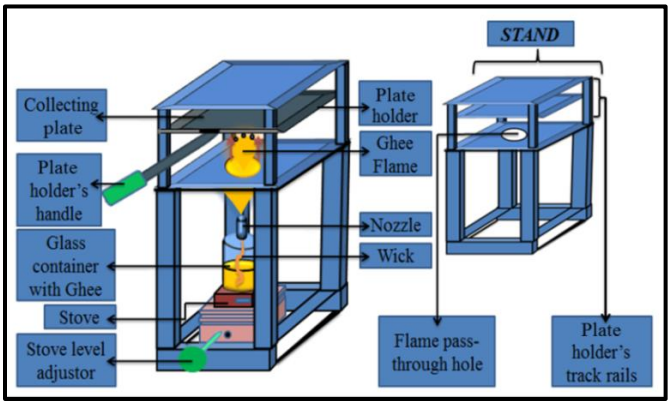

Scheme 5.2: Diagram showing the GFP set-up.

5.2.2. Preparation and placement of the ghee oil

The ghee oil was prepared from the stock product as purchased. The ghee butter was firstly melted at 40 °C in a 250 ml glass beaker to obtain a liquid form of the butter. The oil was poured into a glass container through a nozzle using a funnel. Fibre glass wick was then immersed in the oil such that it extracts the oil by capillary actions and/or surface tension. The glass container was then placed under the collection plate. The distance between the nozzle and the collecting plate was 4 cm.

5.3. Synthesis of CNOs using GFP

The wick wetted with ghee oil was ignited to produce flame in air. However, the wick sizes effects have been investigated using different wick thicknesses. The produced flame had distinct zones recognised by different colours. The zone with the orange-yellow colour is the zone from which the black soot originates. The pitch black soot is believed to be produced by the flame due to incomplete or partial combustion of the fuel (ghee) in the middle zone of the luminous flame with moderate temperature (~1000 °C) of the flame.

A 5 mm thick recycled (fused silica) glass plate was used to collect the soot onto it while cooling at 10 minutes intervals for an hour to avoid cracking the glass due to heat transfers. Moreover, the heat resistance of the collecting plates was investigated and a 1.5 mm thick brass plate was also used to collect the soot for an hour. The soot coated onto the collecting plate and the plate was let to cool down for about 15 minutes to room temperature. A microscope glass slide was used to scrap-off the soot-product from the collecting plate. The yield of the materials was also monitored based on the amount of ghee butter used, synthesis period and the wick sizes and the results are summarized in **Table 5.1**, for both type of collecting plates (brass and glass).

After the collection of soot, it was subjected to high temperature treatment. The materials produced regarded as pristine carbon nano-onions (pCNOs) were annealed at 900 °C under Ar atmosphere. The annealing process was done by varying the exposure periods in order to investigate the heat treatment effect with respect to time. About 0.2 g of pCNOs was put in a 75 mm long quartz boat and the boat was placed into the quartz tube which was then placed at the

furnace's isothermal zone in a horizontal chemical vapour deposition (CVD) reactor. The furnace with the tube was firstly heated up to 900 °C in 100 mL min^{-1} of Ar flow for 1 hour 30 minutes. The carrier gas (Ar) was firstly passed at the same rate during the annealing process. Annealing was done for hours ranging from 1 to 3 hours and the samples were labelled as a_1CNOs, a_2CNOs and a_3CNOs for pCNOs annealed for 1,2 and 3 hours, respectively.

5.4. Doping the as-synthesized materials with nitrogen

The collected soot was functionalized further by doping with nitrogen. About 0.2 g of CNOs was put in a 75-mm long quartz boat and the boat was placed into the quartz tube which was then placed at the furnace's isothermal zone in a horizontal chemical vapour deposition (CVD) reactor as illustrated in **Scheme. 5.3**. A glass bubbler also was filled with about 50 mL of NH_3 prepared for the doping process. In order to maintain the desired furnace heating rate and reaction temperature under specific gas flow rates, the furnace was electronically controlled by a temperature programed device connected to the reactor's furnace. The furnace with the tube was firstly heated up to 900 °C in 100 mL min^{-1} of Ar flow for 1 hour 30 minutes.

The pCNOs were then doped with N at 900 °C using the ex-situ doping process. The source of the dopant (N) was NH_3. Ar was passed through the quartz tube along with NH_3 such that it carries along the ammonia gas to the pCNOs put in the furnace. The doping was carried out for an hour under the same Ar flow and furnace heating rates and the sample was labelled as ndCNOs. Moreover, the effect of the gas flow rate (NH_3) was investigated by increasing the NH_3 flow rates. The Ar flow rates were then varied at 50 mL/min intervals from 50-150 mL/min. The furnace was cooled down to room temperature under Ar atmosphere after every doping process and the samples were labelled as nd_1CNOs, nd_2CNOs and nd_3CNOs for pCNOs annealed at 50,100 and 150 mL/min respectively.

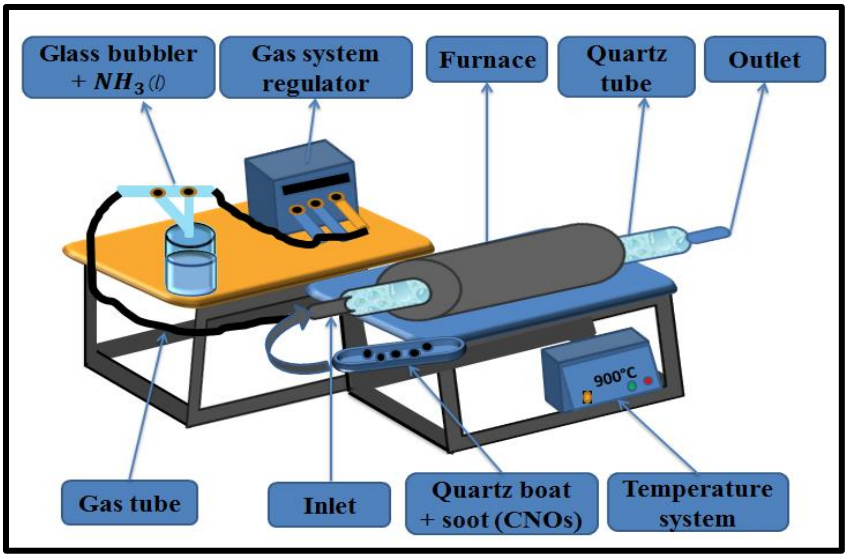

Scheme 5.3: Diagram showing a CVD reactor set-up used for doping the CNOs with nitrogen.

5.5. Characterization of the CNOs

The morphology of the CNOs was ascertained by transmission electron microscopy (TEM) using a Tecnai Spirit T12 instrument at 120 kV and high-resolution transmission electron microscopy (HRTEM) using a Tecnai G2 30ST at 200 kV. The instrument was coupled with an energy-dispersive X-ray spectroscopy (EDS) detector. About 1 mg of sample was analysed by placing the sample in a glass vial containing 5 mL of ethanol. The mixture was then sonicated for 20 min in order to disperse the sample and also to attain a homogeneous suspension of CNOs in the solvent. A drop of the suspension was then spread on a copper grid (Structure Probe, Inc. (SPI) copper grid (200 mesh), and then it was allowed to dry at room temperature. The grid was then mounted onto an exchange rod of the instrument's sample holder and placed into the instrument's chamber and analysed.

The external structural composition, morphology and surface topology of CNOs were studied by scanning electron microscopy (SEM) using a FEI Nova 600 instrument at 30 kV. The CNOs sample was analysed with the aid of carbon tape which was stuck onto the aluminium stub. The sample then placed onto the tape and coated with gold/palladium. The stub was then mounted on the instrument's stage, which was moved into the chamber and analysed.

X-ray diffraction (XRD) patterns were collected on a Bruker D2 phaser diffractometer in Bragg-Brentano geometry with a Lynxeye detector using Cu-Kα radiation at 30 kV and 10 mA. The scan range was $10° \leq 2\theta \leq 90°$ in 0.026° steps, using a standard speed with an equivalent counting time of 1 s per step. The diffraction peaks were then compared with those of standard compounds reported in the diffraction plus evaluation package using the EVA (V11.0, rev.0, 2005) software package.

Fourier transform infrared spectroscopy (Bruker Vector 22 FT-IR spectrometer) was used to determine the surface functional groups on the CNOs. A sample was placed on the instrument's analyser and the transmittance scans were performed producing the IR spectra.

The graphitic nature of the CNOs was investigated using Raman spectroscopy (micro-Raman of a Jobin-Yvon T64000 Raman spectrometer). The spot size on the sample was approximately 1.5 μm in diameter. A wavelength of 514.5 nm from an argon ion laser source coupled to a charge coupled detector (CCD) was used to collect the data.

The thermal stability and the differential thermogravimetric analysis of the CNOs were monitored using a Perkin Elmer Thermogravimetric analyser (6000). In a standard run, about 10 mg of CNOs were placed into a high-temperature alumina sample cup that was supported on an analytical balance located in the furnace chamber of the analyser and the sample was heated from 35 °C to 900 °C at 10 °C/min for 90 minutes per analysis.

The Brunauer-Emmett-Teller (BET) analyser was used to determine the surface area and pore volume of CNOs using a Micromeritics Tristar 3000 surface area and porosity analyser. CNOs were degassed at 150-200 ºC and analysed at -195 ºC.

The Ultraviolet-visible (UV–vis) absorption spectrum of the resultant sample (CNOs) was monitored using a Varian Cary 500 UV-vis NIR spectrophotometer. The solid sample was sonicated in ethanol to disperse the sample before being drop casted onto the glass substrates for analysis in the spectrophotometer.

5.6. Results and discussions

5.6.1. Morphology analysis of the CNOs

The CNOs' soot was characterized using a HRTEM in order to investigate the morphological features of the synthesized nanomaterial. As shown in **Figs. 5.1a** and **b**, the HRTEM micrographs revealed that the as-synthesized CNOs have quasi-spherical shapes with different particle sizes that are less than 100 nm [24, 25]. The average particle size was found to be ~55 ± 4.1 nm. Furthermore, results show that pCNOs exhibit concentric multi-layers resembling that of an onion-like structure owing their name as CNOs with the lattice fringe spacing of 0.27 nm as shown in **Fig. 5.1c**. Similar results were obtained by Habiba and Shen in their studies [26, 27].

These nanomaterials are mostly connected in an accreted form (see **Fig. 5.1b**). Upon heat treatment of the pCNOs it was observed that there was no improvement of the concentric multi-layering, instead, the opposite occurred. The connected nanomaterials coalesce to form bigger non-concentric multi-layered structures showed by arrows in **Figs. 5.1d, e** and **f**. The diameter sizes of the CNOs increased with annealing time due to coalescence of the nanomaterials. Heat treatment of pCNOs promoted coalescence to form bigger nano-onions depending on the period of annealing. After annealing pCNOs for 1, 2 and 3 hours, smaller nano-onions coalescence to form bigger onions as shown in **Figs. 5.1d, e** and **f** respectively.

It was evident that larger nano-onions formation depends on the annealing period. The prolonged annealing process does not only alter the size of the nanoparticles formed but also the layering of the nano-onions shells (see **Fig. 5.1f)**.

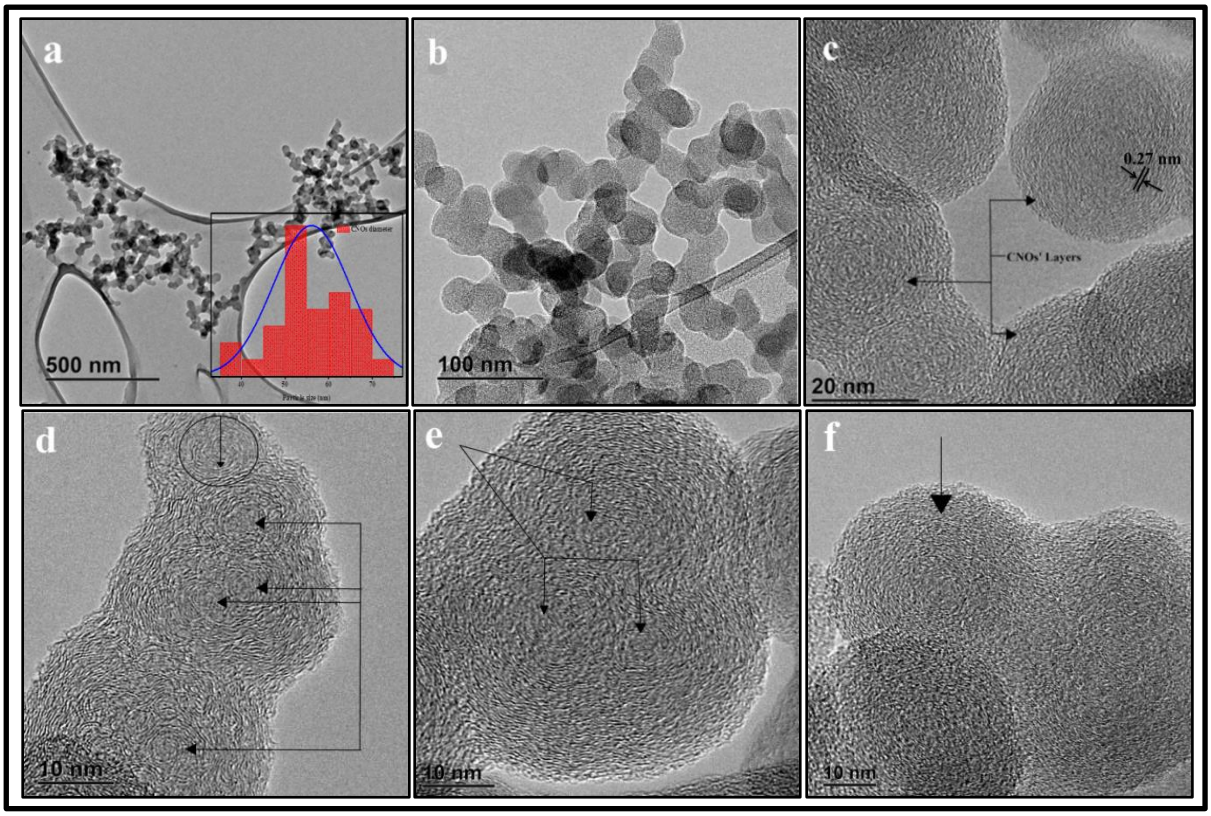

Figure 5.1: TEM micrographs of CNOs; (a, b and c) pristine CNOs (d) CNOs annealed for 1 hour (e) CNOs annealed for 2 hours (f) CNOs annealed for 3 hours.

The CNOs were characterized further using a SEM to support the information from the HRTEM. As shown in **Figs. 5.2a** and **b**, the SEM micrographs of the CNOs confirm that these nanomaterials are connected with quasi-spherical shapes. There were no foreign nanomaterials formed other than nano-onions. However, it is not clear from these micrographs to observe the effect of annealing. The nano-onions clustered to form bigger onions when the pCNOs were annealed (see **Fig. 5.2b**).

In contrast to the CNOs formed through a CCVD method, CNOs synthesized by GFP do not contain any impurity (such as the metal catalyst). With reference to the amount of Ghee butter used, synthesis period, type of collecting plate and the wick sizes, the yield of CNOs' soot was recorded according to **Table 1**.

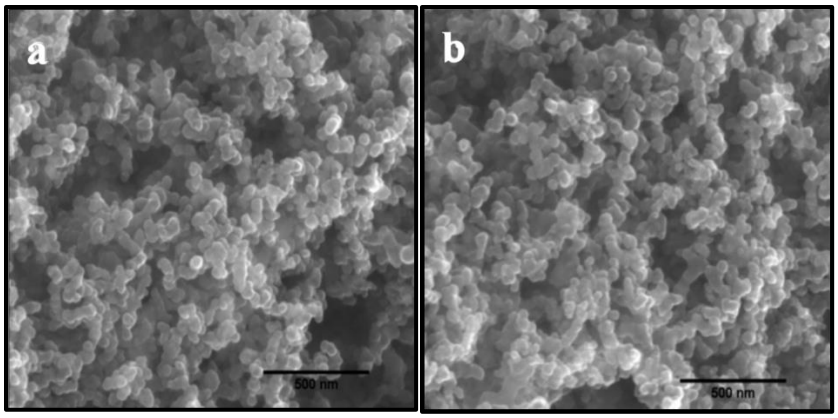

Figure 5.2: SEM micrographs of CNOs synthesized using Ghee oil; (a) pristine CNOs and (b) annealed CNOs, respectively.

Table 5.1: Summarizes yield results of CNOs

Glass plate					
Synthesis period (hour(s))	**Wick thickness (mm)**	**Initial ghee oil (G_i) (g)**	**Final ghee oil (G_f) (g)**	**$G_i - G_f$ (g)**	**Soot yield (CNOs) (g)**
1	10	100	78.21	21.83	0.52
1	20	100	61.73	38.34	0.58
1	30	100	46.33	53.71	0.73
1	40	100	36.24	63.84	1.19
Brass plate					
Synthesis period (hour(s))	**Wick thickness (mm)**	**Initial ghee oil (G_i) (g)**	**Final ghee oil (G_f) (g)**	**$G_i - G_f$ (g)**	**Soot yield (CNOs) (g)**
1	10	100	77.63	22.42	0.59
1	20	100	56.31	43.71	0.62
1	30	100	44.84	55.23	0.81
1	40	100	33.22	66.83	1.33

The results in **Table 5.1** show that the yield of CNOs' soot depends directly on the amount of ghee butter used, synthesis period, type of collecting plate and the wick sizes. The brass

collecting plate (a metal alloy of copper and zinc) showed better yield per hour (see results **Tables 5.1**). This can be due to the robustness of the metal against heat energy from the flame (at ~1000 °C). Glass (fused silica) had lower yields due to the cooling periods which served to avoid cracking/breaking. However, with the same amount of oil and period of soot collection, the wick size showed a positive effect on the flame produced yielding certain amount of soot, respectively (i.e. in both cases, the soot yield increased with wick diameters). This can be attributed to more absorption of the ghee oil by the thicker wick compared to the narrower ones.

It is suggested that the CNOs formed through the bottom-up approach as depicted in **Scheme. 5.4** [28]. As the flame decomposes, the ghee composition molecules break down by heat energy to form carbon multi-layered shells. In the flame's dark zone, pyrolysis (cracking) of the fuel (ghee) begins because of inadequate oxygen forming the carbon containing molecules and eventually minute carbon particles. The temperature is about 1,000 °C which can also extend to further carbon particles formation in the luminous zone (orange-yellow region of the flame) [29]. The carbon particles cluster and rearrange under heat conditions. The rearrangement might be promoted by heat energy present during clustering which leads to the concentric multi-layers formation. Other carbon containing molecules binds onto the carbon shells formed to produce functionalised CNOs.

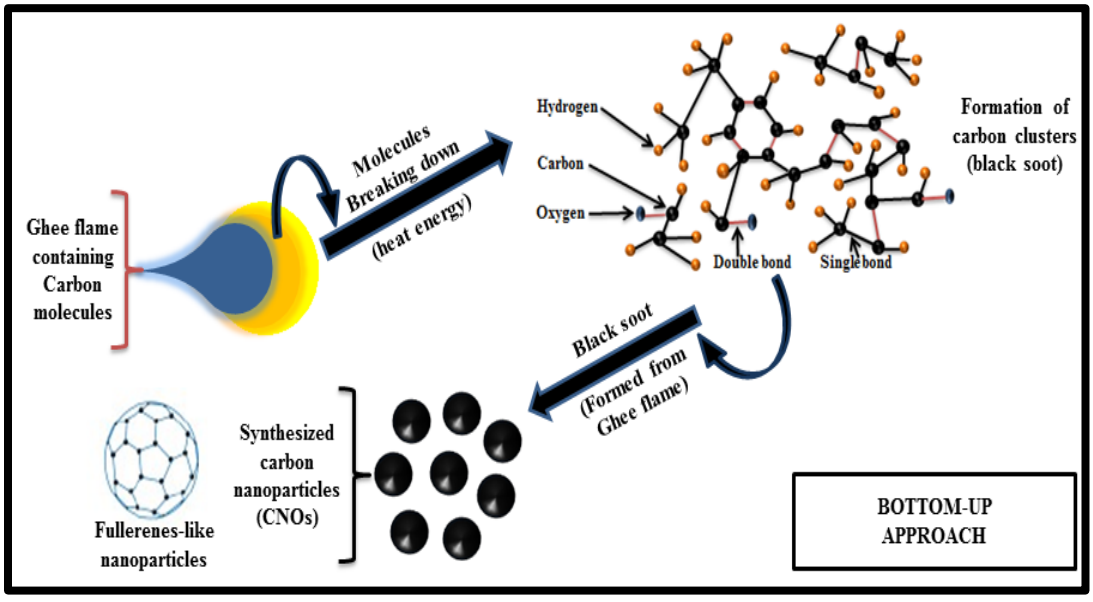

Scheme 5.4: Diagram showing suggested bottom-up approach for the formation of CNOs.

Analogously, the annealing process is described in **Scheme. 5.5**. It was evident from HRTEM micrographs that the nano-onions formed undergo clustering to form new/more nano-onions upon further heat treatment. This can be due to the unburned ghee oil particles surrounding the soot particles on the collection plate during the pyrolysis, which then burn to form new onion-like nanostructures during the annealing process. The oil particles can also be intercalated in the pristine CNOs (pCNOs) layers to introduce structural disorders upon annealing the pCNOs.

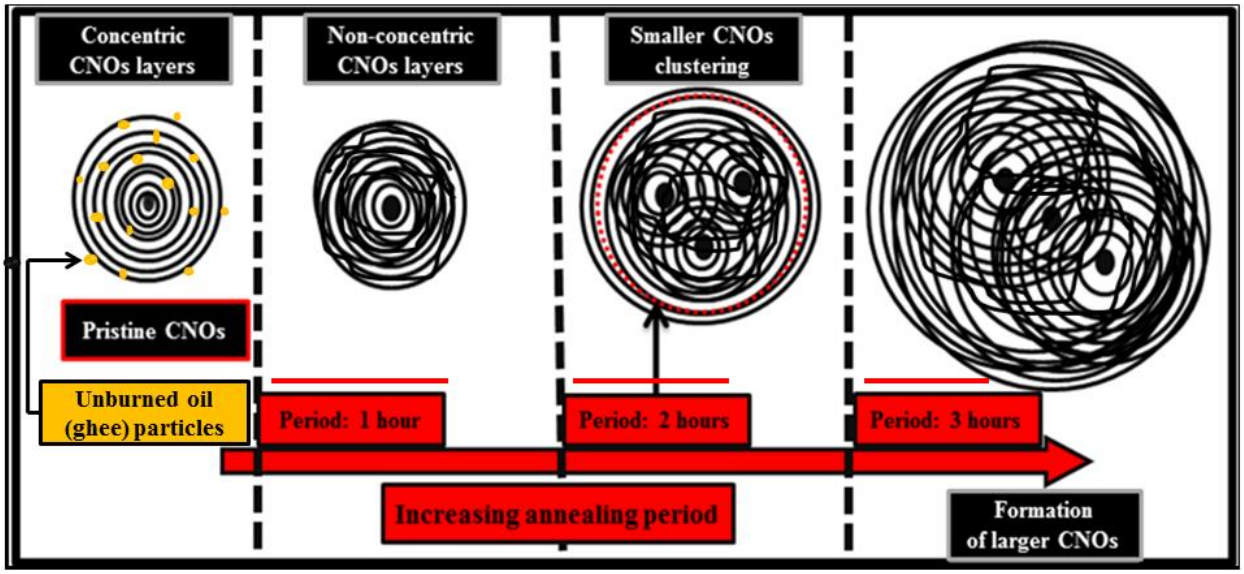

Scheme 5.5: Describes the coalescence effect on CNOs with increasing annealing time.

5.6.2. XRD spectroscopy of CNOs

XRD measurements were conducted to study the crystallinity of prepared CNOs. The patterns were observed as shown in **Fig. 5.3**, revealed that the CNOs prepared differently were fairly composed of carbon without any other impurity. All CNOs pattern showed carbon peaks centered at 2θ = 28.3 º and 51.1º corresponding to (002) and (004) planes of carbon, respectively. These patterns confirmed that carbon materials were formed. However, the appearance of peak centered at 2θ = 51.1º signifies that the CNOs produced contain graphitic carbon domains [30].

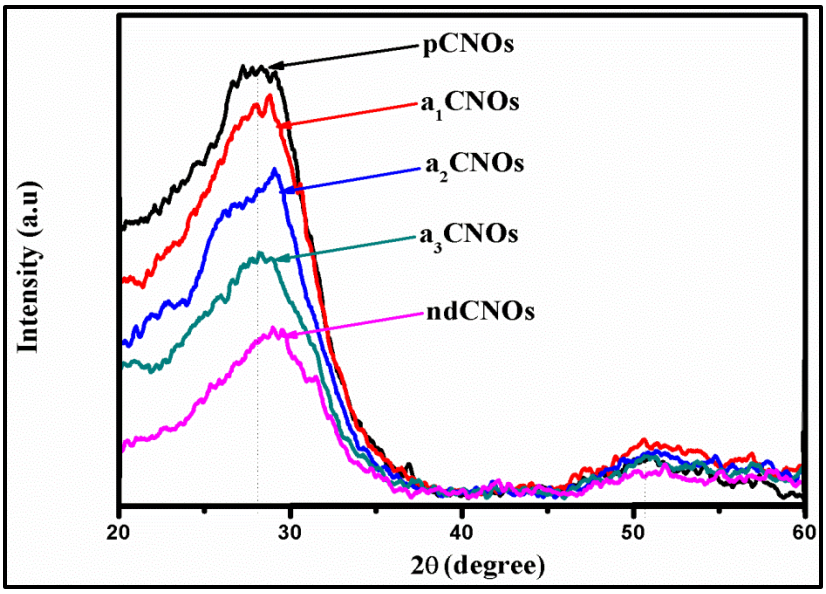

Figure 5.3: The XRD pattern of prepared pCNOs, aCNOs and ndCNOs using a glass collector.

5.6.3. FTIR spectroscopy of ghee butter and prepared CNOs

The surface functional groups of the ghee butter and CNOs were characterized by FTIR. The ghee spectrum showed peaks between 607 and 1170 cm^{-1} which can be attributed to the characteristics of trans-compounds of the butter as shown in **Fig. 5.4a** [31]. The vibration modes of $-CH_3$ were observed at 1375 and 1465 cm^{-1}. However, some additional peaks of high intensity at 2849 and 2919 $cm^{-1}$are also present, which probably arises from symmetric and asymmetric C-H stretch vibrations of alkyl groups from some ghee compounds.

It was observed that all CNOs prepared by GFP, either annealed or doped produced the same transmittance results for each spectrum (see **Fig. 5.4b**). It was seen that a band appeared at 1026 cm^{-1} which can be from a symmetric C-O vibration and phenol groups [32]. The peaks appearing at 2094 and 2322 cm^{-1} can be attributed to weak C=C stretching frequencies with that of medium C-H stretching frequency observed at 2666 cm^{-1}. The medium C-H band can be due to the presence of sp^3 stretching vibrations. These CNOs surface functionalization can be the ones promoting water solubility of CNOs prepared from ghee butter although it was not evident for the presence of the –OH groups around 3600 cm^{-1} [33].

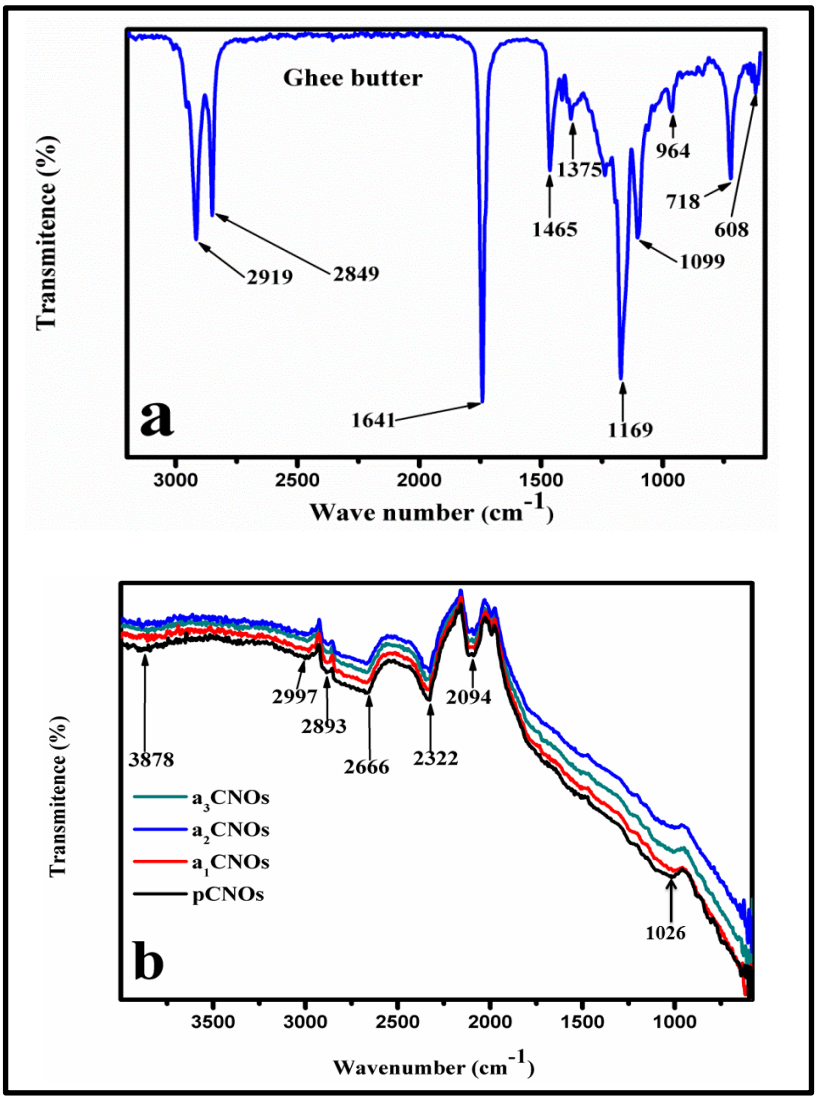

Figure 5.4: FTIR spectrum of the CNOs.

5.6.4. Raman spectroscopic analysis of the aCNOs

The Raman spectra in **Fig. 5.5** show two prominent peaks, corresponding to D-band and the G-band for CNOs polymorph. The peak positions with the intensity ratios (I_D/I_G) are summarized in **Table 5.2**. The peaks observed between 1338 cm^{-1} and 1355 cm^{-1} are ascribed to the D peak for disorder induced by C–C vibration band of carbon and which corresponds to disruptions in sp^2 bonding, such as dangling bonds, sp^3 bonding, vacancies, and carbon rings other than hexagon [34]. The G peak is ascribed to the C=C graphite carbon in-plane vibration modes of the carbon material with sp^2 orbital structure [34, 35]. The I_D/I_G intensity ratios were used to quantify the

degree of graphitization of the CNOs [36]. The I_D/I_G value of greater than 1 implied that low graphitization degree resulted from the long-range structural disorder of the CNOs.

The I_D/I_G intensity ratios were used to quantify the degree of disorder of the CNOs since it is directly related to the extent of defects in the form of sp^3 and the presence of shorter graphitic fragments [37]. It was observed that upon annealing the as-obtained CNOs, the I_D/I_G increased from 0.97 to ~1.05. This means that the annealing process introduces CNOs' structural defects and/ or disorders instead of improving graphitization degree which is in agreement with the HRTEM results.

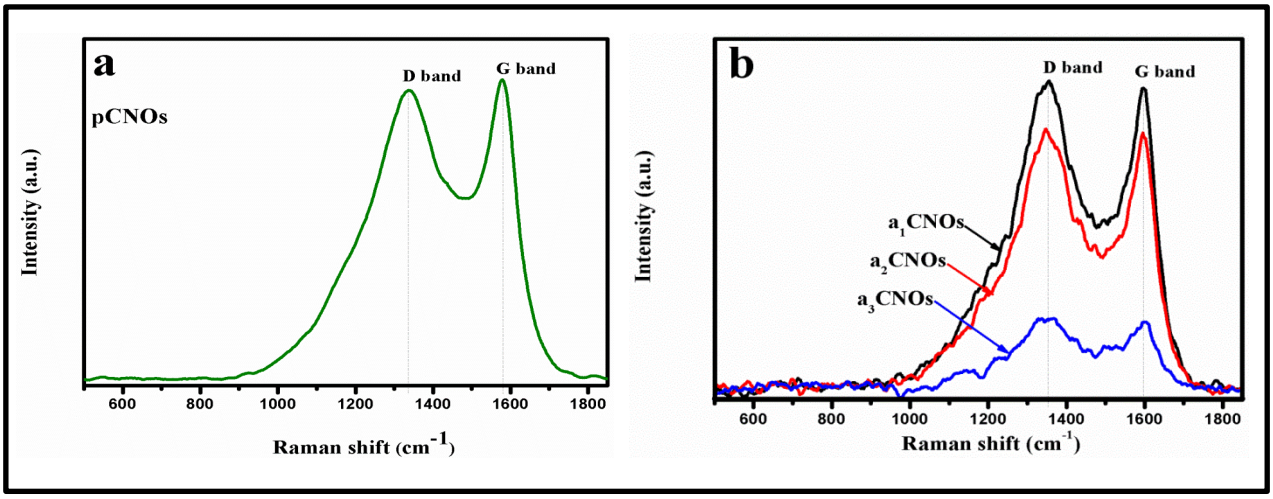

Figure 5.5: Raman spectra of CNOs; (a) pristine CNOs and (b) annealed CNOs, respectively.

Table 5.2: Summarizes Raman data of CNOs

	D band		**G band**		
Sample	Raman shift (cm^{-1})	Intensity	Raman shift (cm^{-1})	Intensity	**I_D/I_G**
pCNOs	1338.6	937.5	1579.5	970.7	0.97
a_1CNOs	1355.1	144.9	1596.0	141.9	1.02
a_2CNOs	1346.4	122.9	1596.0	120.9	1.02
a_3CNOs	1346.4	33.3	1601.8	32.3	1.03

The results in **Table 5.2** further reveal that upon annealing the nanomaterials, there are up-shifts of both the D- and G-bands. These shifts can be attributed to CNOs structural defects since the quasi-spherical CNOs are constructed of nano-domains with a number of defects, such as dangling bonds. The up-shifts of the D peaks can be due to structural disorders of the CNOs while that of the G peaks can be explained by the curvature of CNOs' graphitic shells. However, the peak position of these bands also depends on the quantity of CNOs' multi-layered shells [38].

5.6.5. TGA results of the CNOs

To the best of our knowledge, no TGA data has been reported for CNOs synthesized by FP. However, the CNOs' thermal stability analysis was conducted and it was observed that the onset decomposition temperature of annealed CNOs differs greatly from that of the pristine CNOs as summarized in **Table 5.3**. The pCNOs were observed to have three different decomposition temperatures. This can be due to the loss of surface functional groups at ~220 °C, the decomposition of amorphous carbon at ~366 °C and that of the remaining graphitic carbon at ~490 °C.

The annealed CNOs also had different decomposition temperatures. The a_1CNOs were observed to have lower decomposition temperature (~462 °C) compared to both a_2CNOs and a_3CNOs. It was also evident that this lower decomposition temperature is also less than that of the pCNOs. It is suggested that this temperature difference is due to the structural deformation induced by annealing. As seen from HRTEM micrographs, annealing the nanomaterials for an hour introduced coalescence of smaller nano-onions to form bigger nano-onions with deformed multi-layers. However, a_2CNOs and a_3CNOs were more stable than pCNOs and a_1CNOs (see **Fig. 5.6**). The later had higher decomposition temperature at ~527 °C which can be due to the number of layers and the size of CNOs formed during annealing and coalescence.

The a_1CNOs exhibited a narrower first order derivative peak than the pCNOs (see **Fig. 5.7a**). This could be attributed to defects induced functional groups on the surfaces of pCNOs resulting to a broader first order derivative peak for pCNOs. Moreover, the broadness of the first order derivative peak for all aCNOs did not show any prominent difference (see **Fig. 5.7a and b)**. For

all CNOs synthesized there was no residue after an overall decomposition process which implies that the prepared nanomaterials are highly pure as shown in **Fig. 5.6**.

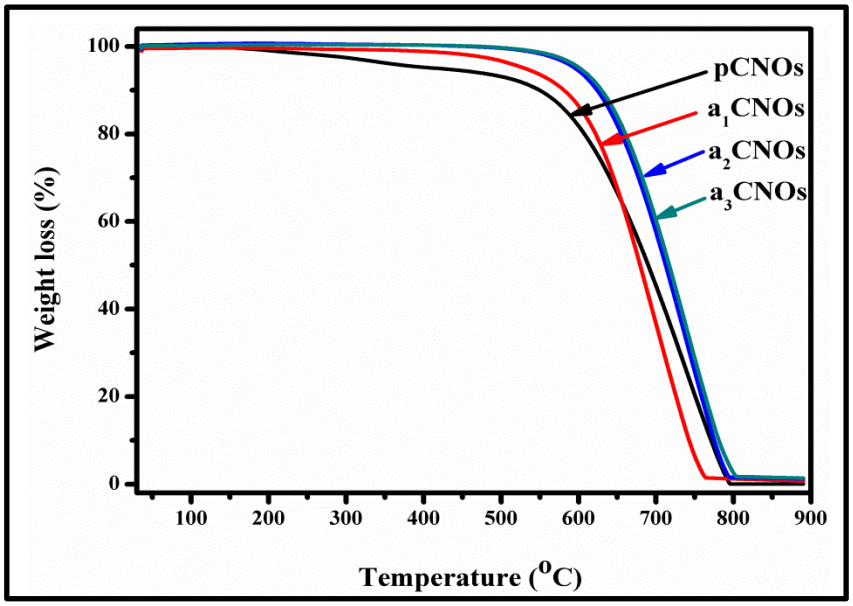

Figure 5.6: The percentage weight loss as a function of temperature for pCNOs and $a_{1,2,3}$CNOs.

Table 5.3: Summarizes TGA/DTGA data of CNOs

CNOs Sample	Onset decomposition temperature (ºC)	Derivative peak center (ºC)
pCNOs	220, 366 and 490	214, 338 and 735
a_1CNOs	462	699
a_2CNOs	527	741
a_3CNOs	527	741

The as-synthesized CNOs were further doped with N to tailor their catalytic properties. For N-doped CNOs, it was observed that the onset decomposition temperature of all N-doped CNOs ($nd_{1,2,3}$CNOs) was at 560 °C. These results were compared to that of a_1CNOs since doping was done while heating the materials for an hour.

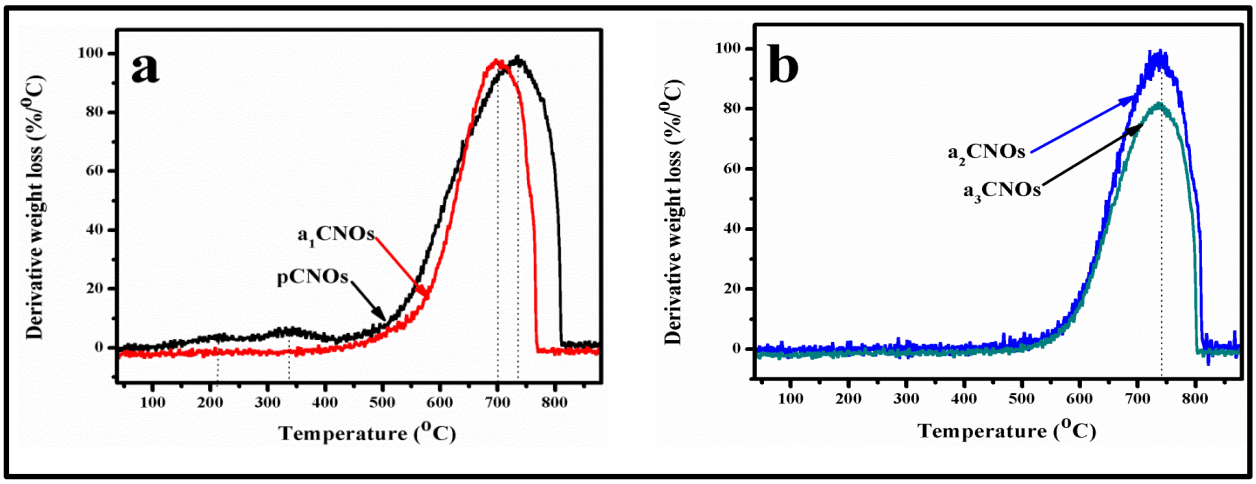

Figure 5.7: The derivative weight loss as a function of temperature, (a) for pCNOs and a_1CNOs, (b) for a_2CNOs and a_3CNOs.

Upon doping, it was expected that the thermal decomposition temperatures for $nd_{1,2,3}$CNOs decrease after functionalization due to increased structural defects. However, $nd_{1,2,3}$CNOs had a higher decomposition temperature than that of a_1CNOs and it can be due to the nitrogen atoms introduced into the carbonaceous matrix of the CNOs as suggested by the TGA results obtained (see **Fig. 5.8)**. This chemical functionalization therefore, plays an essential role in tailoring the properties and application versatility of CNOs. It is suggested that when doping CNOs, the N atoms form shorter carbon-nitrogen bonds on the internal layered-shells surfaces of the CNOs as illustrated in **Scheme. 5.6**. Pyridinic nitrogen, lactam nitrogen, pyrrolic nitrogen, graphitic nitrogen, and/or quaternary nitrogen are the possible suggested types of nitrogen atoms that can be found binding on the inner layered-shells of the CNOs [39].

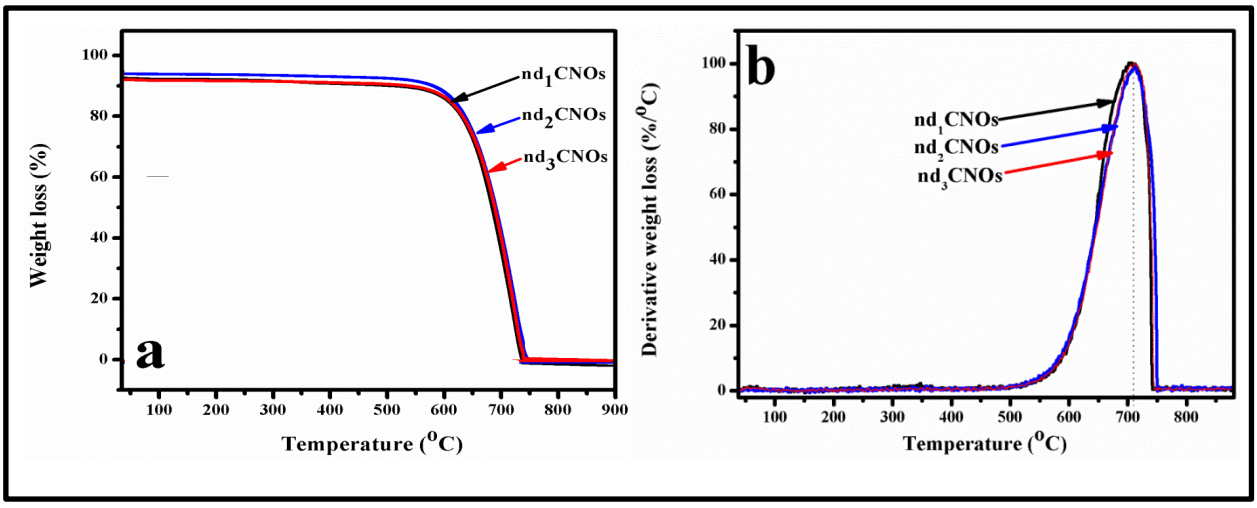

Figure 5.8: The percentage weight loss and derivative weight loss as a function of temperature for $nd_{1,2,3}$CNOs.

With an observed different thermal stability, the as-prepared and annealed CNOs surface areas were found to be 53 and 48 m^2/g, respectively. The pristine CNOs have higher surface area compared to the annealed CNOs. This suggests an increase in the particle sizes due to annealing effect. These results show that CNOs have lower surface area compared to the CNOs produced via CCVD method.

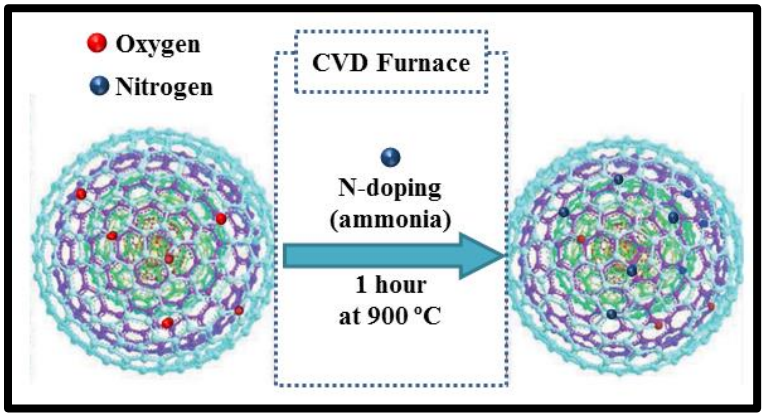

Scheme 5.6: Doping illustration of CNOs structural modification using nitrogen source [39].

Further characterization of the N-doped CNOs was done to obtain information based on the surface of the doped CNOs. **Fig. 5.9** shows the FTIR spectra of the N-doped CNOs using different nitrogen source gas flow rates. It is evident that there are different functional groups present. It was seen that a band appeared at 1080 cm^{-1} which can be from a symmetric C-O vibration and phenol groups [32]. Those appearing at 1578 and 1815 cm^{-1} suggests the presence of the C=O functional groups whereas peaks appearing at 2100, 2335 and 2711 cm^{-1} can be attributed to weak C=C stretching frequencies with that of medium C-H stretching frequency observed at 2711 cm^{-1}. However, small peaks were observed between 2711 and 3648 cm^{-1} shown by arrows (highlighted region) in **Fig. 5.9**. These small peaks suggest the presence of N-H groups [32].

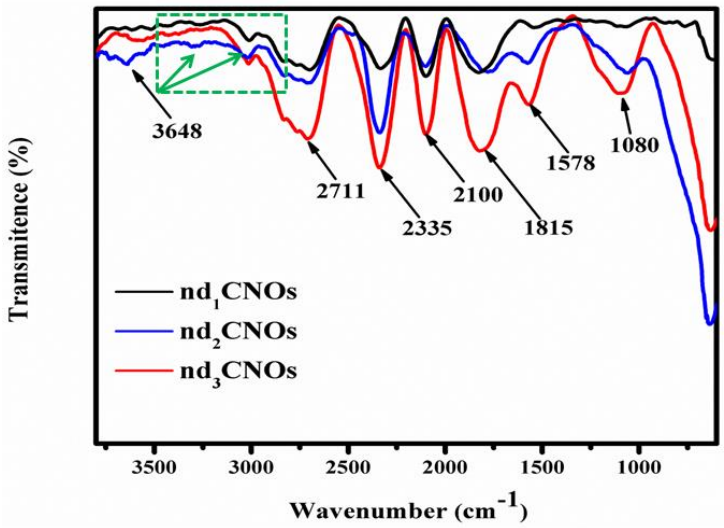

Figure 5.9: FTIR spectrum of nitrogen doped CNOs.

The Raman spectra of the N-doped CNOs show that the D-band intensities are slightly higher than the G-band intensities which can be attributed to structural defects introduced by the hetero atom (see **Fig. 5.10**). The intensity ratios are given in **Table 5.4** and reveal that higher the flow rate of ammonia gas introduces increased structural defects.

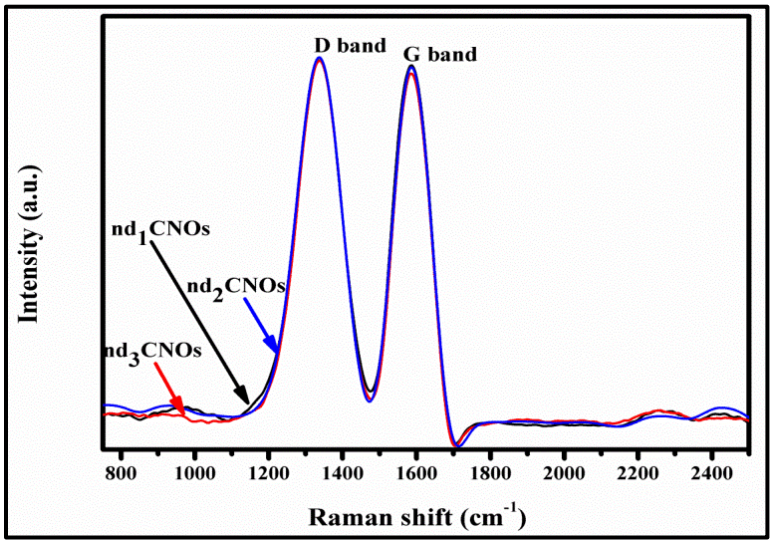

Figure 5.10: Raman spectra of nitrogen doped CNOs at different ammonia gas flow rates.

Table 5.4: Summarizes Raman data of nitrogen doped CNOs

	D band		G band		
Sample	Raman shift (cm^{-1})	Intensity	Raman shift (cm^{-1})	Intensity	I_D/I_G
nd_1CNOs	1340.2	53.57	1586.0	52.84	1.01
nd_2CNOs	1340.2	53.56	1586.0	52.11	1.03
nd_3CNOs	1340.2	53.52	1586.0	51.43	1.04

5.6.6. UV-vis absorption spectrum of as-synthesized CNOs and annealed CNOs

The UV-vis spectra of pCNOs and $a_{1,2,3}$CNOs are shown in **Fig. 5.11**. The spectra show that pCNOs optically absorb in the ultraviolet region. The absorption band evolves at ~200 nm which indicates that the materials synthesized absorb the ultraviolet light since this peak is below the visible region (<400 nm). Similarly, $a_{1,2,3}$CNOs seem to absorb light in the ultraviolet region. These observations can be attributed to the overlapping of aromatic polycyclic hydrocarbons of CNOs [40, 41].

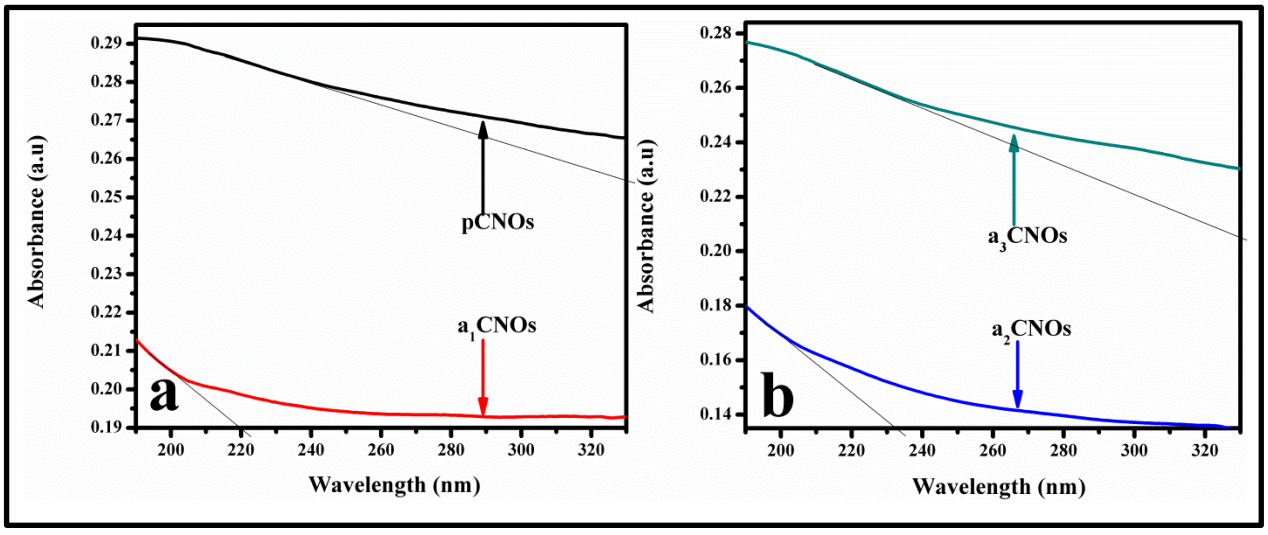

Figure 5.11: UV-vis absorption spectrum of the pCNOs and aCNOs.

The estimated band gap energy (Eg) of the pCNOs, a_1CNOs, a_2CNOs and a_3CNOs was 2.17, 4.43, 5.32, 2.27 eV, respectively. These results show that these materials have electrical

properties which might grant them an opportunity to be applied in various electronic devices such as solar cells (e.g. DSCs).

5.7. Conclusions

The synthesized CNOs are nanomaterials with particle sizes less than 100 nm and also exhibit concentric layers. The synthesized CNOs did not incorporate any metal nanoparticle(s) suggesting solid CNOs formed. The concentric layers exhibited by the solid CNOs formed ranged from 4 to 25 shells with the shape similar to those reported by Zheng et al [42].

The materials formed showed better graphitization before high temperature treatment. High temperature treatments promote the formation of larger CNOs. The CNO yield depends on the amount of ghee butter used, synthesis period, type of collecting plate and the wick sizes. As discussed in Section 5.6.1 (results in Table 5.1). The brass metal plate show better (increased with time taken for pyrolysis) yield when compared to the glass substrate.
The CNOs have potential to absorb in the UV-vis region which the character is granting them an advantage to be used for various electronics application.

References

1. Wang X, Xu B, Liu X, et al. *Diamond and Related Materials.* 15 (2006); p 148
2. Carrasco JA, Prima-Garcia H, Romero J, et al. *J. Mater. Chem. C*. 4 (2015); p 440
3. Borgohain R, Yang J, John P, et al. *Carbon*. 66 (2014); p 274
4. Zhang H. Liang C. Liu J, et al. *Carbon.* 55 (2013); p 108
5. Daniel Ugarte. *Nature.* 359 (1992); p 707
6. Ahmed GHG, Laíño RB, Calzón JAG, et al. *Beilstein J. Nanotechnol*. 7 (2016); p 759
7. Bu IYY. *Solar Energy.* 105 (2014); p 237
8. Tripathi KM, Bhati A, Singh A, et al. *RSC Adv.* 6 (2016); p 37323
9. Mohapatra D, Badrayyana S, Parida S. *Materials Chemistry and Physics.* 174 (2016); p 113
10. Tripathi KM, Tran TS, Kim YJ. *ACS Sustainable Chem. Eng.* 5 (2017); p 3983
11. Zhou M, Li Q, Zhong S, et al. *Materials Chemistry and Physics*. 198 (2017); p 188
12. Matsoso BJ, Kamalakannan Ranganathan K, Mutuma BK, et al. *RSC Adv*. 6 (2016); p 106915
13. Mohapatra D, Badrayyana S, Parida S. *Materials Chemistry and Physics.* 174 (2016); p 114
14. Ning X, Li Y, Dong B, et al. *Journal of Catalysis.* 348 (2017); p 100
15. Bu IYY. *Solar Energy.* 105 (2014); p 241
16. Han F, Yao B, Bai Y. *J. Phys. Chem. C.* 115 (2011); p 8926
17. Mabena LF. Ray SS. Mhlanga SD, et al. *Applied Nanoscience.* 1 (2011); p 70
18. Meena Mehta. *Food Scince research journal.* 4 (2013); p 116-120
19. Dhurvey YR, Kawtikwar PS, Sakarkar DM. *International Journal of ChemTech Research.* 4 (2012); p 185-188
20. Brigelius-Flohe R, Traber MG. *The FASEB Journal*. 13 (1999); p 1146
21. Vesely MVJ, Oesterhelt G. *Journal of Chromatography*. 83 (1973); p 447
22. Kaneki M, Hosoi TMD. *Nutrition.* 22 (2006); p 846
23. Zou Q, Li YG, Lv B, et al. *Inorganic Materials.* 26 (2010); p 127
24. Macutkevic J, Kuzhir P, Seliuta D, et al. *Diamond and Related Materials.* 19 (2010); p 92
25. Bartelmess J, Giordani S. *Beilstein J. Nanotechnol.* 5 (2014); p 1981-1989
26. Habiba K, Makarov VI, Weiner BR, et al. *Manufacturing Nanostructures.* 1 (2014); p 267
27. Shen J, Zhu Y, Yang X. *Chem. Commun.* 48 (2012); p 3690
28. Homann KH, Wagner HG. *Proceedings of the Royal Society of London. Series A, Mathematical and Physical Sciences.* 307 (1986); p 141-152

29. Qiao Z, Li J, Zhao N, et al. *Scripta Materialia.* 54 (2005); p 226
30. Dhurvey YR, Kawtikwar PS, Sakarkar DM. *International Journal of ChemTech Research.* 4 (2012); p 187
31. Plonska-Brzezinska ME, Dubis AT, Lapinski A. *Chemphyschem.* 12 (2011); p 2666
32. Tripathi KM, Tran TS, Kim YJ. *ACS Sustainable Chem. Eng.* 5 (2017); p 3985
33. Plonska-Brzezinska ME, Dubis AT, Lapinski A. *Chemphyschem.* 12 (2011); p 2663
34. Zhang C, Li J, Liu E, et al. *Carbon.* 50 (2012); p 3517
35. Obraztsova ED, Fujii M, Hayashi S, et al. *Carbon.* 36 (1998); p 822
36. Mutuma BK, Matsoso BJ, Ranganathan K, et al. *RSC Adv.* 7 (2017); p 21190
37. Gubarevich AV, Kitamura J, Usuba S, et al. *Carbon. 41 (2003), p 2604*
38. Lin Y, Pan X, Qi W. *J. Mater. Chem. A.* 2 (2014); p12475-12477
39. Yang S, Feng X, Zhi L, et al. *Adv. Mater.* 22 (2010); 839
40. Koudoumas E, Kokkinaki O, Konstantaki M, et al. *Chemical Physics Letters.* 357 (2002); p 338
41. Tripathi KM, Tran TS, Kim YJ. *ACS Sustainable Chem. Eng.* 5 (2017); p 3987
42. Yanbin Zheng, Pinwen Zhu. *RSC Adv*. 6(2016); 9228

Chapter 6: Fabrication of dye-sensitized solar cells using CNOs

6.1. Introduction

This chapter of the dissertation presents results and discussions based on the fabrication of dye-sensitized solar cells (DSSCs).

Fossil fuels are nonrenewable source of energy such as coal, gas and oil. They are often used to meet high energy demands. However, their uses have negative impacts such as producing air and environmental pollution. Studies on alternative renewable energy technologies have been conducted with an aim of harnessing renewable energy resources and sustaining resources for the modern society. Amongst available sources of renewable energy, solar energy has been seen as one of the possible solutions to the energy challenges [1].

After the observation of a photovoltaic (PV) effect was made by Becquerel in 1839 [2], there were many developments made of photovoltaic cell theory which laid the foundations for the third PV device phase. In this phase, DSSCs, also referred to as Gräetzel cells were discovered. These types of cells use solar energy sourced from the sun to generate electrical energy (conversion of sunlight (radiant) energy into electrical energy) hence they mimic the photosynthesis process in plants. They were firstly co-invented in 1988 by Brian O'Regan and Michael Gräetzel [3-4].

The cells are regarded as clean energy generators and form part of the independent power (energy) producers [5]. Normally the cells use platinum (Pt) as a catalytic layer, which is an extremely important component for the regeneration of the dye-sensitizer after electron ejection upon excitation through the photovoltaic effect [6]. Pt metal is the catalyst used in DSSCs and it also assists in completing the circulation of electrons in the entire device. However, Pt is very expensive and can be sensitive to different electrolytes [7]. This challenge can be addressed by applying nanostructured materials such as multi-walled or single-walled carbon nanotubes (CNTs), carbon black, polyaniline and graphene in solid-state DSSCs [8-9].

Recently, it was found that DSSC fabrication can be done with a pair of carbon-based electrodes using conductive carbon nanostructured materials (CNMs) as the working counter electrode with an aim of substituting Pt catalyst [10].

The DSSCs are of low cost and they have been reported to have high efficiencies which depend on materials used during fabrication [11]. Wei reported on DSSCs [12], and revealed that the devices have both transparency and flexibility. The cells have advantages compared to the amorphous silicon solar cells (ASSCs) and their advantages are: (1) the direct energy transfer can be realized in DSSCs, (2) having good cost effectiveness for the production and that the semiconducting-electrolyte interface can be easily formed, (3) less sensitivity to semiconductor defects compared to ASSCs.

In trying to improve the performance of the DSSC, many research studies have been conducted and the counter electrodes (CE) have been varied. The CE has been reported to be the critical component of a DSSC and it serves as a mediator for collecting electrons from an external circuit and reducing I_3^- ions to I^- ions for the redox couple to be generated. In the DSSC, a platinized counter electrode (PtCE) is normally used. The use of the PtCE in the DSSC is mainly due to its high conductivity and catalytic activity for reduction of I_3^- ions. However, the PtCE has been found to have some limitations such as the corrosion of platinum in the presence of the redox electrolyte (I^-/I_3^-) [13, 14].

This study focuses on using carbon nano-onions as catalytic material in DSSCs because of their good chemical and physical properties which includes catalytic and electrical properties [15, 16]. These properties offer them better opportunities for various applications including their application in solar cells.

6.2. Fabrication procedure

For the purpose of this study, DSSCs have been fabricated in order to test the use of CNOs as a counter electrode nanomaterial (catalytic purposes). We hereby report on the photocurrent to voltage characteristics of CNOs based DSSCs when compared to the platinum based DSSCs. In this study, we have applied CNOs in DSSCs to show their catalytic activity when they replace Pt.

6.2.1. Starting materials

Acetone (CH_3COCH_3, ≥ 99.5%), ethanol (CH_3CH_2OH, 96%) and deionized water (d-H_2O) were used for cleaning processes as obtained from Sigma-Aldrich and our laboratory respectively. Acetic acid (CH3COOH, ≥ 99.85%), acetyl acetone ($CH_3COCH_2COCH_3$, ≥ 99.3%), acetone, ethanol, fluorine-doped tin oxide (FTO) glasses, N719 dye-sensitizer, titania (TiO_2) (Degussa, P25) powder were used as purchased from Sigma-Aldrich. Sunlight dish washing soap and a copper foil were also used as purchased from a local super market (Pick n' Pay). Moreover, 1-hexyl-3-methylimidazolium iodide ($C_{10}H_{19}IN_2$, ≥ 98%), iodine (I_2, ≥ 98%), 4-tert butylpyridine ($C_9H_{13}N$, ≥ 96%), 3-methoxypropionitrile ($CH_3OCH_2CH_2CN$, ≥ 98%) and lithium iodide (LiI, ≥ 99%) were purchased from Sigma-Aldrich for the preparation of the redox electrolyte (I^-/I_3^-) solution.

6.2.2. Preparation of the photoanode and deposition of the dye-sensitizer

In DSSCs, each and every layer plays an important role. The transparent polycrystalline semiconducting titania (TiO_2) nanoparticles usually have a high surface area and mainly act as a photoanode. The porous TiO_2 thin film assists in transferring electrons from the dye-sensitizer and electrolyte to the transparent conducting oxide (TCO). Fundamentally, when a DSSC is illuminated, photons are absorbed by dye molecules, which inject electrons from their excited states into the conduction band of the TiO_2 nanoparticles to leave the dye molecule oxidized. Oxidized dye molecules are reduced by a redox electrolyte, which transports the positive charges by diffusion to the back/counter electrode of the cell [17].

In this study Degussa, P25 TiO_2 powder was used to prepare a slurry paste. 1.0 g of TiO_2 was put in a beaker and 0.3 mL acetyl acetone was added to the powder. This was followed by the addition of 12 mL d-H_2O and constant heating and stirring of the slurry at 60 °C for 24 hours to prevent re-aggregation of TiO_2 nanoparticles. Furthermore, the obtained granulated powder was ground to a fine powder. 0. 2 mL of acetic acid was then added to the powder along with 1 mL of sunlight soap and 3 mL of ethanol added drop wise. The mixture forming a slurry paste was continuously stirred for 3 hours.

FTO glasses were cleaned with d-H_2O, acetone and ethanol sequentially and the paste was deposited onto the conducting sides of the clean FTOs which served as TCOs for each cell. After the paste deposition, the TiO_2 coated FTOs were allowed to stand at room temperature for 5 minutes and then annealed in a furnace at 450 °C for 15 minutes. Annealing at 450 °C was done to remove any organic components and to improve the contact between the paste and the dye-sensitizer. The ruthenium complex dye-sensitizer (N719) was added to the cooled TiO_2 coated FTOs and allowed to dry at room temperature as shown in **Fig. 6.1b**.

6.2.3. Preparation of the CNOs based counter electrode

The DSSCs counter electrode was prepared using Pt as reference electrode and CNOs as a carbon based electrode. Firstly, a reference Pt based counter electrode was prepared with a thin layer (~40 nm) sputtered onto the clean FTO as a reference electrode and compared to CNOs counter electrodes (see **Fig. 6.1a**). CNOs were then dispersed in ethanol and ultra-sonicated for 15 minutes. The CNOs solution was drop-casted onto clean FTO glasses while heating the glass at 60 °C until a fairly uniform coated FTO was obtained as shown in **Fig. 6.1c**.

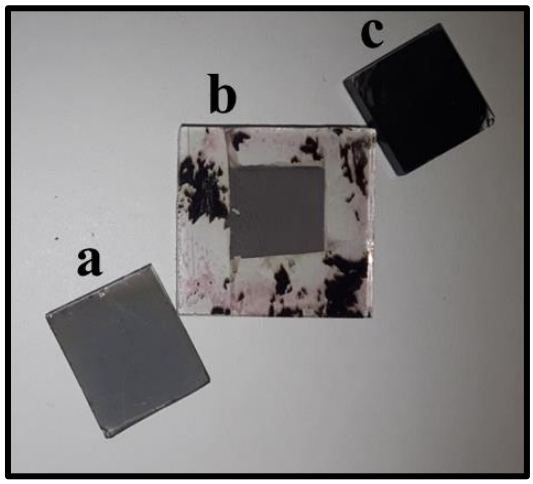

Figure 6.1: Device coated FTOs; (a) normal, used as reference with Pt catalyst counter electrode, (b) normal, used as photoanode with TiO_2 paste and dye-sensitizer stain, (c) CNOs coated FTO used as a counter electrode (cathode).

6.2.4. Device assembly (fabrication)

The photoanode and counter electrodes were combined to complete each cell. Both electrodes were combined using clamps before the electrical conductivity test. The photoanode was placed face up on a flat surface and the CNOs and or Pt counter electrode was placed on top of the photoanode which allowed the non-coated offset position of each electrode. The area of each cell was ~1 cm^2.

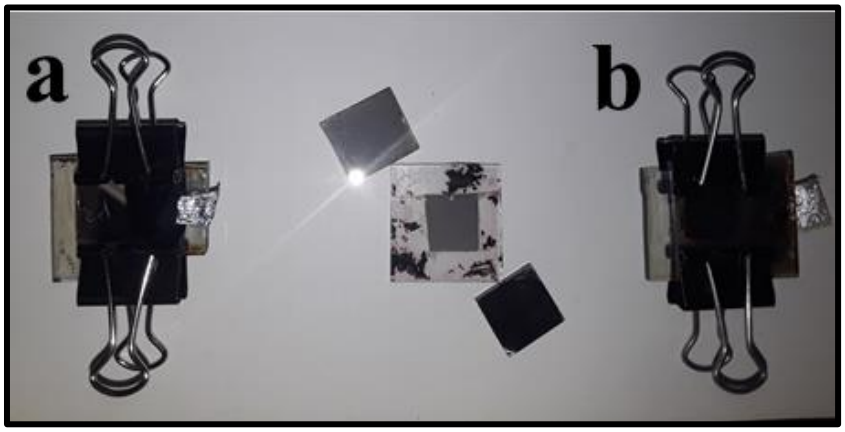

Figure 6.2: Shows fabricated cells using different counter electrodes, i.e.; (a) Pt based and (b) CNOs based counter electrode.

Each electrode was placed offset from the other counter electrode, exposing the non-coated part which allowed both electrode electrical contact and elimination of cell shorting as shown in **Fig, 6.2a and b**. The cell assembly and the device architectures are depicted in the schematic diagrams shown in **Scheme. 6.1 and 6.2**. The **Schemes 6.2a and b** both show the Pt architectures and CNOs based DSSCs respectively. All other components of each cell were similar except for the active catalyst since Pt and CNOs catalysts were tested interchangeably.

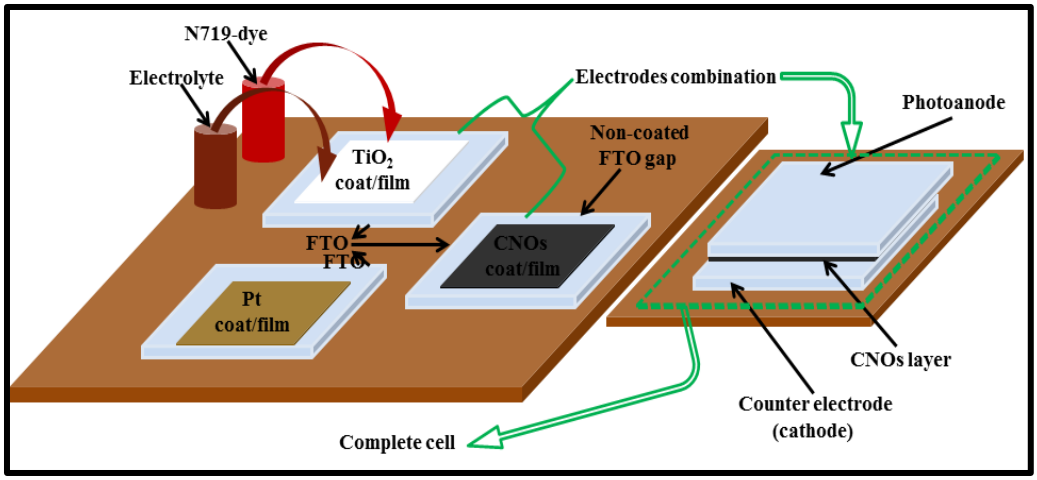

Scheme 6.1: Schematic diagrams of the DSSC assembly using Pt and different CNOs [18].

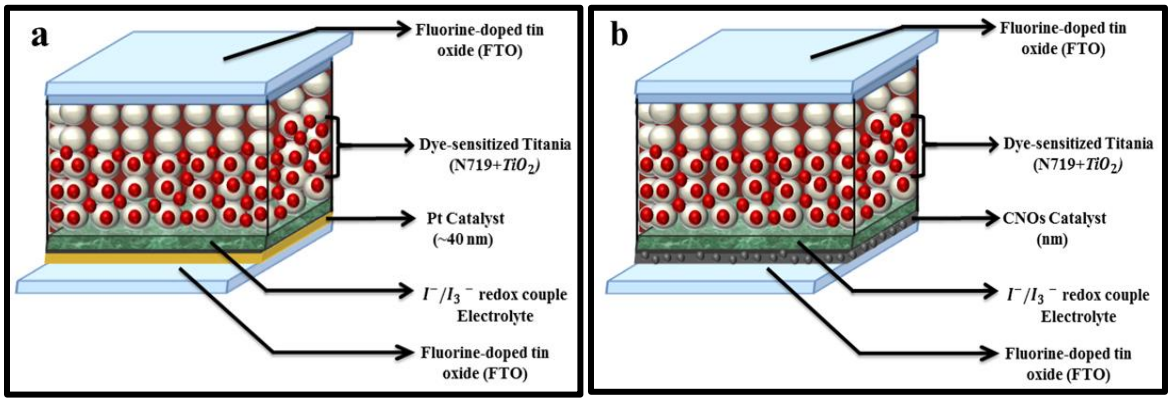

Scheme 6.2: Device architecture: (a) normal, used as reference with Pt catalyst counter electrode, (b) device with CNOs nanoparticles catalyst counter electrode [19-20].

6.2.5. Testing the devices

The fabricated devices were all tested using a liquid electrolyte. The electrolyte solution was prepared using 0.6 M methylhexylimidazolium iodide, 0.1 M iodine, 0.5 M tertbutylpyridine and 0.1 M lithium iodide in 3-methoxypropionitrile. The redox electrolyte solution was then placed at the edges of the offset electrodes. The solution was then drawn into the space between the electrodes through capillary action.

The photocurrent density-voltage (J–V) characteristics of each cell were obtained using the solar simulator (150 W Xe lamp) with 1.5 air mass filters and a source/measure unit (HP 4141B DC)

under 70 $mW.cm^{-2}$ illumination. All tests or measurements were carried out at room temperature under standard conditions.

6.3. Characterization techniques

6.3.1. Structural characterization

The external structural composition, morphology and surface topology of the nanoparticle based counter electrodes (CE) were determined by scanning electron microscopy (SEM) using a FEI Nova 600 instrument at 30 kV. The CNOs based CE samples was analysed by sticking the FTO coated with CNOs layers onto the aluminium stub. The stub was then mounted on the instrument stage, then placed in the chamber and analysed.

6.3.2. Photovoltaic measurements

For all fabricated DSSCs the photovoltaic tests were carried out by measuring the photocurrent and voltage characteristics of each cell. The J-V characteristic determinations were performed using a multi-channel J-V measurement system. Measurements were carried out under ambient atmosphere at room temperature and the incident light intensity was controlled at 70 $mW.cm^{-2}$ (AM 1.5G).

6.4. Results and discussions

6.4.1. Structural morphology

The surface of TiO_2 nanoparticles deposited onto the FTO(s) plays an important role that is related to the performance of each cell [21]. **Fig. 6.3a** shows one of the negative effects based on the TiO_2 surface. Cracking of the TiO_2 as shown by an arrow in **Fig. 6.3a** must be avoided since this can retard the flow of charge through the cell (from the semiconducting TiO_2 to the TCO) [22]. This effect will cause poor cell performance due to the poor active surface of the semiconducting material.

It is useful to have a smooth (no cracks), thin surface with evenly distributed nanocrystalline particles of TiO_2 (anatase) for better electron transfers as shown **in Fig. 6.3b and c**. Moreover, not only the photoanode layer is important but also the counter electrode. The catalytic layer

thickness is important to avoid any form of resistance. However, the use of carbon based materials as active catalyst in the cell brings about drawbacks in terms of the carbon layer thickness which still need considerable improvement. As shown in **Fig. 6.3d and e**, a smooth and thin film of Pt was deposited onto FTO was used as the reference counter electrode.

The prepared CNOs film is shown in **Fig. 6.3d and f**. It is evident from these SEM micrographs that the thickness of the film is larger than that of the Pt film (see arrows in **Fig. 6.3d**). The micrographs also reveal that the CNOs film is not smooth (rough surface) compared to the Pt film (see **Fig. 6.3e and f**). These results also suggest that further optimization of the CNOs layer preparation is needed to make a better preforming cell.

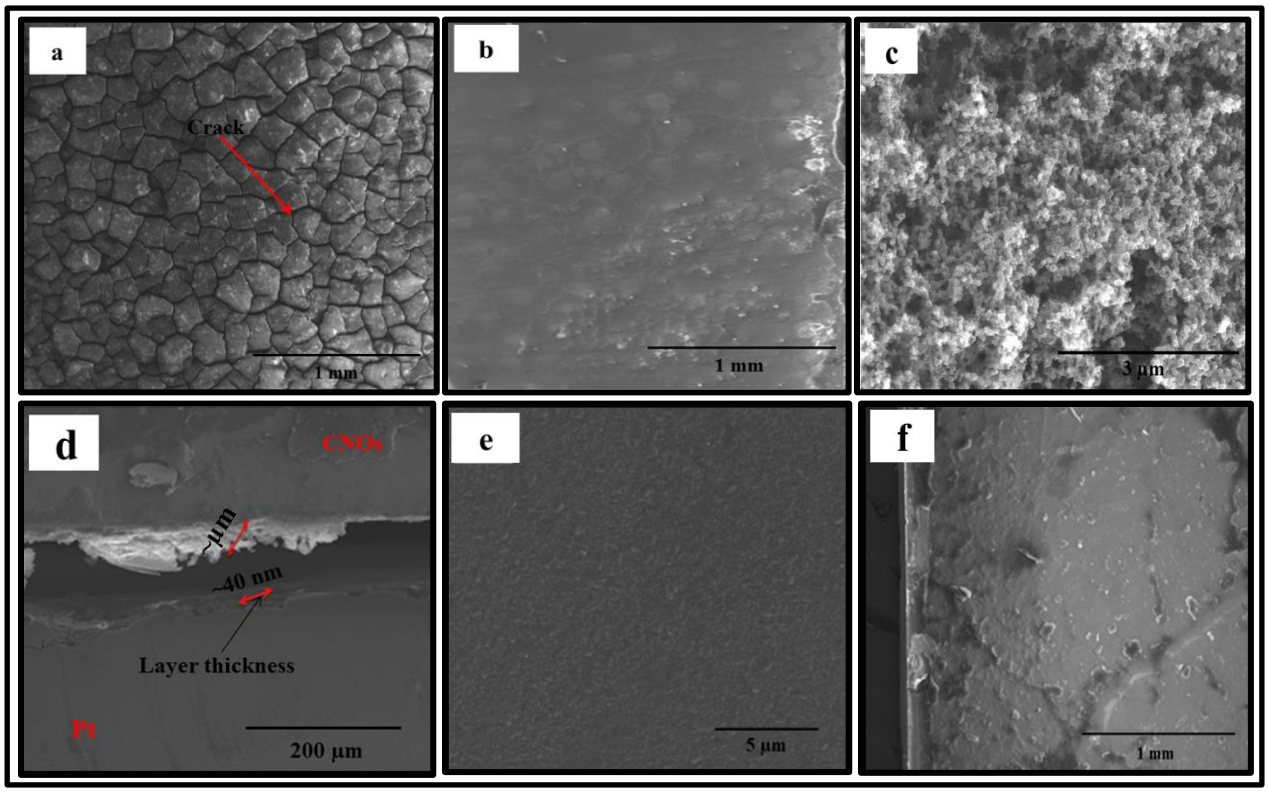

Figure 6.3: SEM micrographs; (a) cracked TiO_2 paste on FTO photoanode, (b) smooth TiO_2 paste on FTO photoanode, (c) nanocrystalline TiO_2 (anatase) film nanoparticles, (d) CNOs and Pt layers on separate FTOs as counter electrodes, (e) smooth Pt layer on FTO, (f) rough CNOs surface layer coated on FTO.

6.4.2. Photocurrent and voltage (J-V) characteristic of the DSSCs

DSSCs behave like a diode with a p-n junction. The DSSCs circuit model has a particular behavior described or represented by the photocurrent density-voltage (J-V) curve shown in **Fig. 6.4**. However, in some cases a J–V curve can present an unexpected knee or S-shape resulting from different operating conditions [23, 24]. The explanation of the physical and chemical phenomena involved in the cell depends on its operation conditions and it can be difficult to explain the phenomenon as it depends on the conditions involved [25]. A single cell consists of a shunted resistance known as the shunt resistance (R_{sh}). The R_{sh} is one of the parasitic parameters which can impinge on the illuminated J-V characteristics and efficiency of a good cell. In the presence of this type of resistance, the leakage current resistance creates a parallel path of high conductivity in the solar photovoltaic panel due to the decrease in the output power and open circuit voltage [26]. The cell can also have a series connection resistance (R_s) which is another parasitic parameter that can affect the cell performance [27].

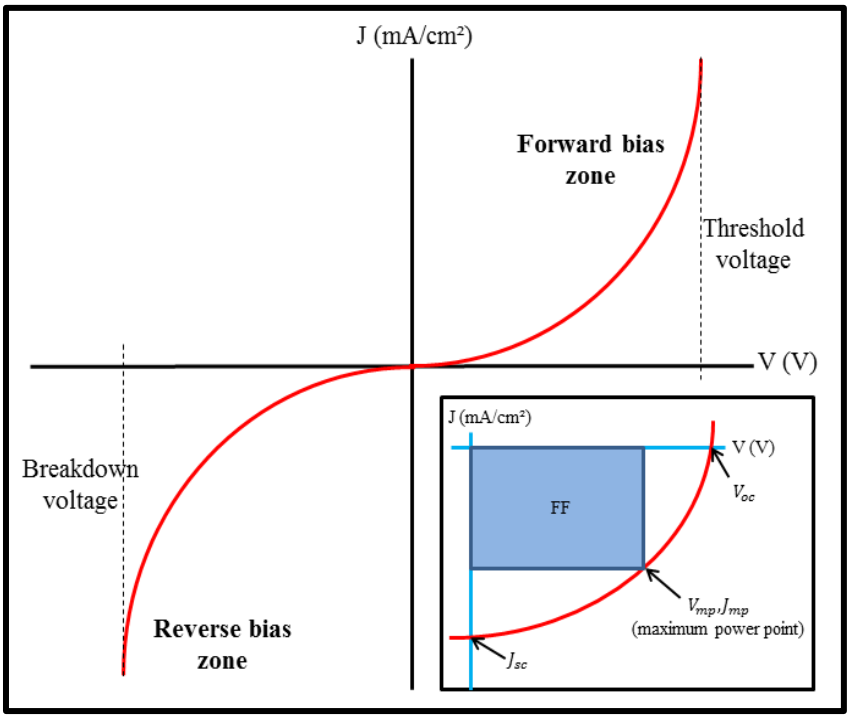

Figure 6.4: The normal J-V characteristic curve of the standard dye-sensitized solar cell [28].

Both the R_s and R_{sh} affect the cell since the short-circuit current density (J_{sc}) depends on both parameters as shown in **Formula 6.1**, where J_{ph} is the light generated current density. Since R_{sh} is a crucial parameter that determines the performance of cell, especially at reduced irradiance levels it becomes a concern when the intensity levels fall. This implies that the irradiance intensity can affect both R_s and R_{sh} [29-31].

$$J_{sc} = J_{ph} - \frac{J_{sc}R_s}{R_{sh}} \quad \text{..... 6.1 [32]}$$

The J-V characteristic curves of different fabricated cells are shown in **Fig. 6.5**. These curves have been obtained using selective CNOs and depend on the structural properties observed and discussed in the previous chapter (i.e. **Chapter 5**). The results show that the DSSCs fabricated show diode-like behavior in which, under dark field conditions, there is no photocurrent generated by the cell. However, a Pt based DSSC was compared to those based on different CNOs. It is evident that the Pt based DSSC has a higher fill factor (FF) when compared to the CNOs (nitrogen doped CNOs) based DSSC.

Unfortunately, the CNOs based cells did not show a good photocurrent response. The cell fabricated using pristine (pCNOs) and the annealed (a_1CNOs) carbon nano-onions showed no fill factor results since there was no observed current and voltage at the maximum power point. This can be due to the parasitic parameters associated with each cell as discussed earlier (i.e. presence of R_s and/ or R_{sh}). Moreover, there are other factors which can contribute to such results. These factors can be the thickness of the catalytic layer, the TiO_2 layer, and the presence of leaking a liquid electrolyte. However, both the open circuit voltage (V_{oc}) and short circuit current (J_{sc}) were observed for all fabricated cells [33]. These observations reveal that CNOs based DSSCs can generated a photocurrent and the size of the current will require optimization for better performance. Negative factors affecting the cells performance can be eliminated by optimizing the conditions in which each cell is fabricated and this includes the use of different redox electrolyte and improved CNOs catalytic layers.

When nitrogen doped CNOs were introduced into a DSSC, the fabricated cell also showed promising results even though the fill factor was lower than that of a Pt based cell as shown in **Table 6.1**. This can be due to the presence of the n-type material in the cell since CNOs doped

with nitrogen can serve as a donor material to improve the catalytic effects of the CNOs in the cell.

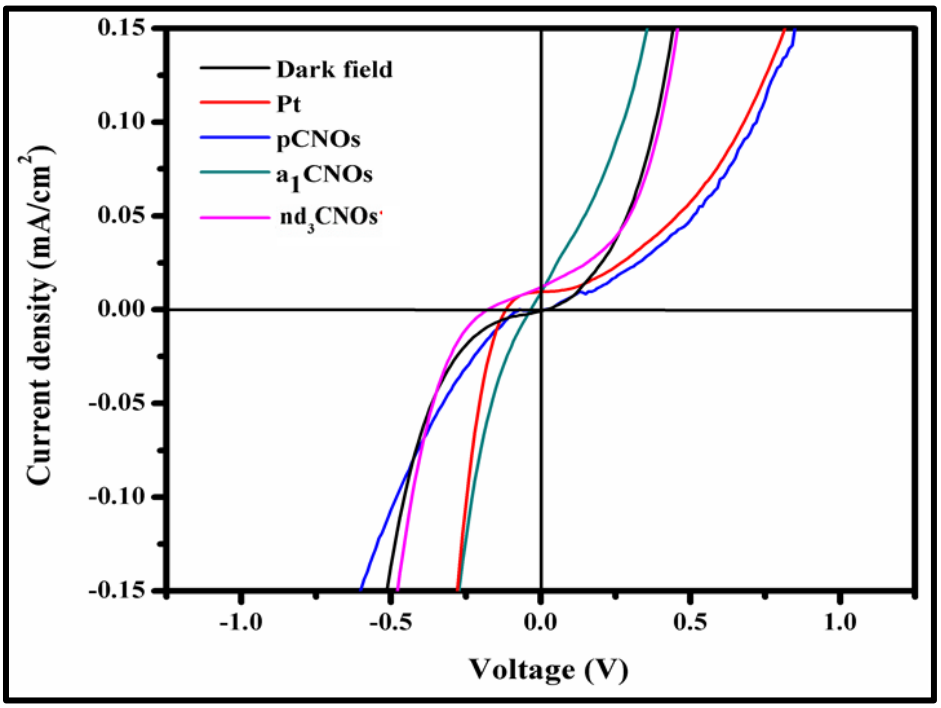

Figure 6.5: The J-V characteristic curves of the fabricated dye-sensitized solar cells. The external parameters of the solar cells are shown in **Table 6.1**.

Table 6.1: The external parameters of the Pt and CNOs based solar cells

Solar cell device (counter electrode)	**J_{sc} (mA/cm^2)**	**V_{oc} (V)**	**J_{mp} (mA/cm^2)**	**V_{mp} (V)**	**FF**
Dark field	0.00	0.00	-	-	-
Pt based	0.18	0.23	0.17	0.20	0.82
Pristine CNOs based (pCNOs)	0.02	0.14	-	-	-
Annealed CNOs based (a_1CNOs)	0.17	0.09	-	-	-
Doped CNOs based (nd_3CNOs)	0.20	0.31	0.16	0.21	0.54

The results show that a Pt based DSSC has a higher fill factor (FF) when compared to the CNOs (nitrogen doped CNOs) based DSSC. This is directly related to J_{mp} and V_{mp} and it corresponds to the photocurrent and voltage values, respectively. The maximum power output is given in the J–V curve [34]. The direct relationship is given by **Formula 6.2**, where J_{sc} and V_{oc} both affect the values FF.

$$FF = \frac{J_{mp}V_{mp}}{J_{sc}V_{oc}} \quad \text{..... 6.2 [35]}$$

The overall performance of the cell can be evaluated in terms of the FF which is a factor that is directly related to the power conversion efficiency ((PCE);ɳ). The PCE is directly proportional to the FF and is hence directly related at a given incident light power (P_{light}) related by **Formula 6.3**. A lower fill factors result in the cell's poor performance for the given incident light power.

$$ɳ(\%) \equiv \frac{J_{mp}V_{mp}}{P_{light}} = \frac{FFJ_{sc}V_{oc}}{P_{light}} x100, \ (\varepsilon\alpha FF) \quad \text{..... 6.3 [36]}$$

6.5. Conclusions

Functionalized CNOs (FCNOs) can be application in DSSCs and would have a promising future for the development of efficient and flexible optoelectronics. Even though FCNOs based DSSCs have lower light to electricity conversion efficiency than the Pt based DSSCs, they can be considerably cheaper to be made and feasible to be printed on a flexible substrate. The FCNOs based DSSCs can exhibit longer lasting properties due to the thermal stability and durability of FCNOs. In addition, since DSSCs can work efficiently in indoor light, because of the dye sensitizer which absorbs diffuse sunlight as well as fluorescent lighting their used can have positive impacts for various communities.

References

1. Qiu X, Burda C. *Chem. Phys*. 339 (2007); p 1
2. Williums R. *The Journal of Chemical Physics Laboratories*. 1 (1959); p 1505
3. Bagher AM. *Engineering Physics*, 1 (2017); p 1
4. Grätzel M, O'Regan B. *Nature*, 353 (1991); p 737
5. Eberhard A. *StanfordPSR*. 1 (2003); p 8
6. Roy-Mayhew JD, Bozym DJ, Punckt C, et al. *ACS Nano.* 4 (2010); p 6209
7. Kyaw AKK, Tantang H, Wu T, et al. *J. Phys. D: Appl. Phys*. 45 (2012); p 1-2
8. Wang H, Hu YH. *Energy Environ. Sci*. 5 (2012); p 8182
9. Zhang DW, Li XD, Li HB, et al. *Carbon.* 49 (2011); p 5382
10. Bagher AM, Vahid MMA, Mohsen M. *American Journal of Optics and Photonics*. 3 (2015); p 99
11. Grätzel M, Dye-sensitized solar cells, *J. Photochem. Photobiol*, C 4 (2003); p 145
12. Wei D, Dye Sensitized Solar Cells. *Int. J. Mol. Sci*. 11 (2010); p 1103
13. Sim K, Sung S, Jo HJ. *Int. J. Electrochem*. *Sci*. 8 (2013); p 8273
14. Murakami TN, Grätzel M. *Inorg. Chem, Acta.* 361 (2008); p 572
15. Qiu X., Burda C. *Chem. Phys*. 339 (2007); p 1
16. Carla T, Cioffi C.T, Palkar A, et al. (2009). *Chem. Eur. J*. 15 (2009); p 4419
17. Gong J, Liang J, Sumathy K. *Renewable and Sustainable Energy Reviews.* 16 (2012); p 5849
18. Chang H, Lo Y. *Solar Energy*. 84 (2010); p 1835
19. Yang X, Yanagida M, Han L. *Energy Environ. Sci*. 6 (2013); p 54
20. Zhang DW, Li XD, Li HB, et al. *Carbon*. 49 (2011); p 5385
21. Singh E, Nalwa HS. *Science of Advanced Materials*. 7 (2015); p 1863–1912
22. Tasi N, Stanojevi ZM, Brankovi Z. *Electrochimica Acta.* 210 (2016); p 608
23. De Castro F, Laudani A, Fulginei FR, et al. *Sol.Energy*. 135 (2016); p 590–597
24. Javier García-Sánchez F, Romero B, Lugo-Mu˜noz DC, et al. *Energet.* 30 (2017); p 327–350
25. Laudania A, Fulgineia FR, Salvini A, et al. *Optik.* 156 (2017); p 312
26. Bisquert J, Cahen D, Hodes G, et al. *The journal of physical chemistry B,* 108 (2004); p 8108
27. Wolf M, Rauschenbach H. *Advanced Energy Conversion*. 3 (1963); p 455
28. Al-Alwani MAM, Abu Bakar Mohamad AB, Ludin NA, et al. *Renewable and Sustainable Energy Reviews.* 65 (2016); p 871

29. D'alessandro V. *Solid-state electronics*, 63 (2011); p 130-136
30. Lal PM, Singh SN. *Solar energy materials & solar cells*. 91 (2007); p 137-142
31. El-Adawi MK, Al-Nuaim IA. *Vacuum*. 64 (2002); p 33
32. Ghani F, Duke M. *Solar energy*. 85 (2011); p 2388
33. Sim K, Sung S, Jo HJ. *Int. J. Electrochem. Sci.*, 8 (2013); p 8273
34. Gong J, Liang J, Sumathy K. *Renewable and Sustainable Energy Reviews*. 16 (2012); p 5850
35. Kontosa AI, Kontosa AG, Tsouklerisa DS, et al. *Journal of materials processing technology*. 196 (2008); p 247
36. Narayan MR. *Renewable and Sustainable Energy Reviews.* 16 (2012); p 212

Chapter 7: General conclusions and recommendations

7.1. Introduction

This last chapter of the dissertation presents general conclusions coupled with recommendations for future work.

7.2. Conclusions

The aim of the study was to synthesize multi-layered CNOs. Multi-layered CNOs were successfully synthesized using two different methods namely; catalytic chemical vapour deposition (CCVD) and Ghee flame pyrolysis (GFP) method. This study successfully produced the required materials with different structural morphologies and the following conclusions were drawn from results obtained in this research project.

7.2.1. Synthesis of CNOs using CCVD and their properties upon annealing

CNOs with multi-layers ranging from 4-25 shells were successfully synthesized using a CCVD method in which an iron catalyst was used to decompose acetylene. TEM micrographs revealed that core-filled CNOs were produced with an average particle size of ~18 ± 3.6 nm. These quasi-spherical nanomaterials have a higher surface area when compared to the carbon spheres.

7.2.2. Synthesis of CNOs using GFP and their properties upon annealing

CNOs with multi-layered shells were successfully synthesized using a GFP method. TEM micrographs revealed that the CNOs produced have particle sizes less than 100 nm (i.e. 55 ± 4.1 nm). These quasi-spherical nanomaterials have a higher surface area when compared to the carbon spheres but lower than that of CNOs produced via CCVD. TGA results revealed that highly pure CNOs were produced following the flame assisted method.

7.2.3. Nitrogen doping of CNOs

With the aim of functionalizing CNOs for application in DSSCs, pure CNOs were doped with a heteroatom (nitrogen) such that the catalytic activity can be improved. It was evident that doping CNOs introduced structural defects that depended on the amount of the nitrogen gas source flow rate. However, it is recommended that further studies be carried out to investigate the amount and type of nitrogen present in the CNOs structural matrix.

7.2.4. CNOs application in DSSCs

In this study, one of the objectives was to introduce different CNOs (i.e. pristine (pCNOs), annealed (aCNOs), and nitrogen doped (ndCNOs) carbon nano-onions into DSSCs and to compare the results with the Pt based DSSC. CNOs were successfully tested as catalytic materials in DSSCs. However, not all CNOs based cells were good cells. It was observed that only the nitrogen doped CNOs showed better and promising results in application with respect to DSSCs. Thus these results suggest further investigations on surface functionalized CNOs.

7.3. Recommendations

With further improvements in electrolytes, catalytic carbon nano-onions, organic dye sensitizers and nanoporous semiconducting electrodes, cheaper but more robust DSSCs can be introduced into the market and compete with traditional thin film solar technologies.

Based on the results obtained, CNOs can act as catalytic carbon based nanomaterial in a DSSC. However, optimization of different layers in DSSCs still needs to be done. Wang and Hu reported that structural defects and functional groups on the surface of graphitic carbon nanomaterials can play an important role in the electrocatalytic sites in DSSC counter electrodes [1]. Therefore, tuning the defects and searching for different effective functional groups for CNOs may be a promising research area to produce good performing CNOs based DSSCs [1].

Another strategy would be to reduce the Pt loading in DSSCs and exploit the Pt/CNOs composite materials as counter electrodes in order to achieve higher power conversion efficiency for CNOs based DSSCs. Furthermore, to achieve a better power conversion efficiency, the thickness of the

carbon film deposited on FTOs during fabrication needs to be improved since the thickness of the film can demonstrate improvements in the J_{sc} and FF as reported by Murakami [2].

This improvement and or optimization of DSSCs is needed to improve the DSSCs devices key performance factors such as the short-circuit current density (J_{sc}), open-circuit voltage (V_{oc}), and fill factor (FF). However, studies of the CNOs surface after deposition onto the FTO needs to be carried out using surface techniques such as atomic force microscopy (AFM), in order to investigate the effect of the surface roughness and properties of the CNOs film.

References

1. Wang H, Hu YH. *Energy Environ. Sci.* 5 (2012); p 8185
2. Murakami TN, Grätzel M. *Inorganica Chimica Acta*. 361 (2008); p 574

Appendix A: Supplementary Information

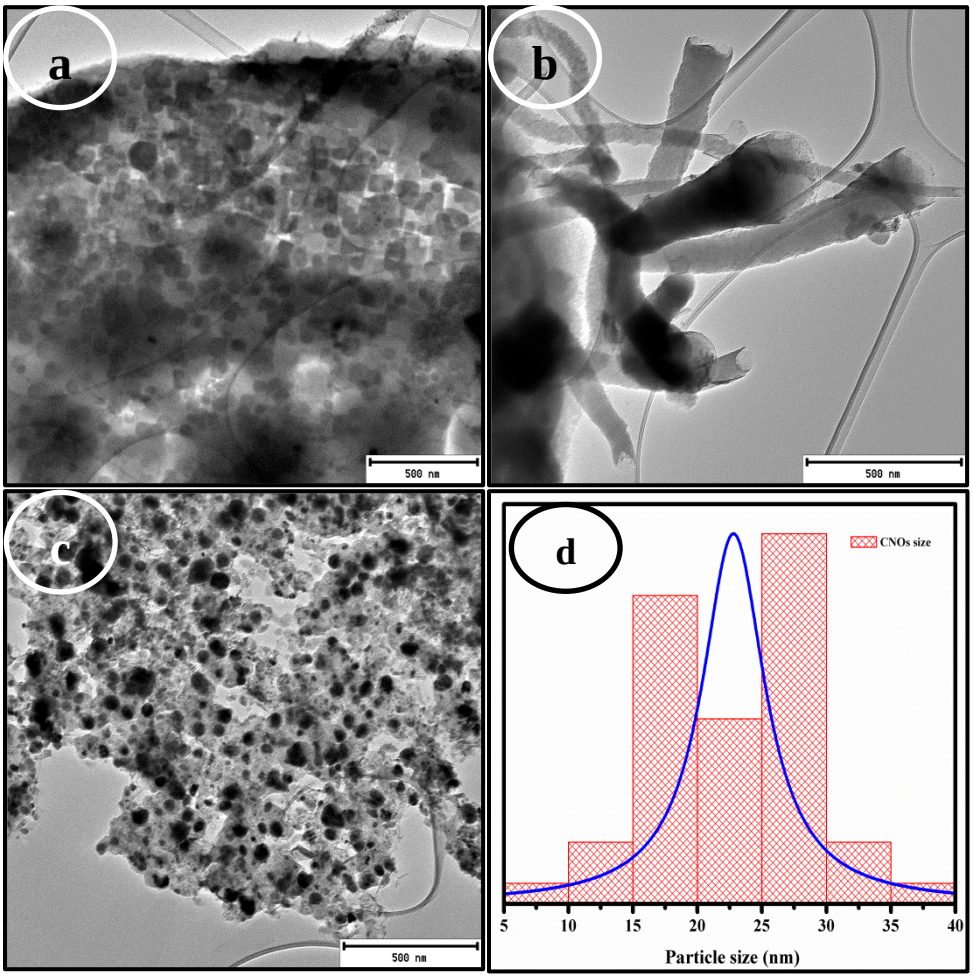

Figure S1: TEM micrographs; (a) Fe nanoparticles, (b) Carbon nano fibers formed at temperatures ~500 °C, (c) CNOs incorporating metal catalyst particles formed at 450 °C, (d) average particle sizes of CNOs.

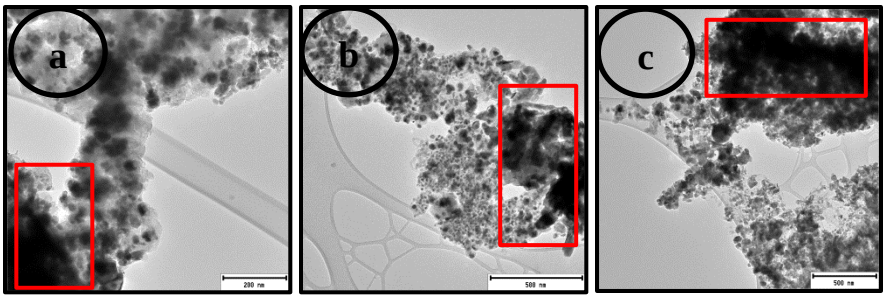

Figure S2: TEM micrographs of agglomerated catalyst particles for different metal to support loadings; (a) 0.6 wt% Fe, (b) 0.9 wt% Fe, (c) 1.2 wt% Fe.

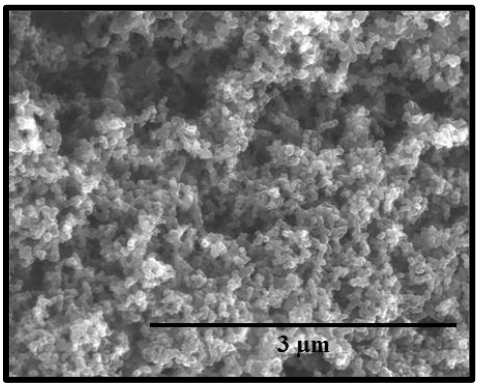

Figure S3: SEM micrograph of CNOs synthesized using brass collecting plate via GFP.